Narrowing the Window for Millicharged Particles by CMB Anisotropy[¶]

S. L. Dubovsky[1], D. S. Gorbunov[1], and G. I. Rubtsov[1, 2]

[1] Institute for Nuclear Research, Russian Academy of Sciences, Moscow, 117312 Russia
[2] Department of Physics, Moscow State University, Moscow, 119899 Russia
e-mail: sergd@ms2.inr.ac.ru, gorby@ms2.inr.ac.ru, grisha@ms2.inr.ac.ru
Received November 17, 2003

We calculate the cosmic microwave background (CMB) anisotropy spectrum in models with millicharged particles of electric charge $q \sim 10^{-6}$–10^{-1} in units of electron charge. We find that a large region of the parameter space for the millicharged particles exists where their effect on the CMB spectrum is similar to the effect of baryons. Using WMAP data on the CMB anisotropy and assuming the Big Bang nucleosynthesis value for the baryon abundance, we find that only a small fraction of cold dark matter, $\Omega_{mcp}h_0^2 < 0.007$ (at 95% CL), may consist of millicharged particles with the parameters (charge and mass) from this region. This bound significantly narrows the allowed range of the parameters of millicharged particles. In models without paraphotons, millicharged particles are now excluded as a dark matter candidate. We also speculate that recent observation of 511-keV γ rays from the Galactic bulge may be an indication that a (small) fraction of cold dark matter is comprised of millicharged particles. © *2004 MAIK "Nauka/Interperiodica"*.

PACS numbers: 14.80.-j; 98.70.Vc; 95.35.+d; 12.90.+b

Search for particles carrying small but nonvanishing electric charge (millicharged particles) has long history. If observed, millicharged particles would either cause serious doubts on the concept of Grand Unification or imply the existence of a new massless gauge boson–paraphoton [1, 2]. Furthermore, the existence of millicharged particles would hint towards processes with apparent electric charge nonconservation, like electron or proton decay to "nothing" [3].

There are various constraints on the parameters (charge and mass) of millicharged particles, coming from accelerator and laboratory experiments and from cosmology and astrophysics (see, e.g., [4–8] for the latest results and [8, 10] for reviews), Fig. 1. Interestingly, reported bounds did not exclude the possibility [11] that a significant part (or even all) of the cold dark matter (CDM) is comprised of millicharged particles.

The constraints on the parameters of millicharged particles are somewhat different in theories with and without paraphotons. Without paraphotons, two domains in the parameter space of millicharged particles are allowed. The first one corresponds to heavy particles with tiny electric charge (left upper corner in Fig. 1) which would never be produced thermally in the early Universe. This region is far beyond the reach of future accelerator and laboratory experiments. In the current letter, we are concerned with another region. This is a narrow window of relatively light particles with masses $M \sim 10^{-3}$–10^2 GeV and charges $q \sim 10^{-6}$–

10^{-1}. Larger charges $q \gtrsim 0.1$ are ruled out by limits on the cosmic ray fluxes of fractionally charged particles [10]. It is worth noting that particles with $q \gtrsim 0.2$ are also excluded by measurements of the width of Z boson (cf. [5]) if one makes use of the latest data [12].

In a model with paraphotons, and for not very small values of the paraphoton coupling constant α', millicharged particles annihilate mainly into pairs of paraphotons. As a result, their annihilation in the early Universe is more efficient and the cosmological bound coming from the relic abundance depends on the value of α' and is generically less restrictive (see Fig. 1) than in the model without paraphotons.

It was noted in [13] that there is a part of the parameter space for the millicharged particles where they do not decouple from the acoustic oscillations of the baryon-photon plasma during recombination, and it was suggested that the effect of these particles on the cosmic microwave background (CMB) anisotropy spectrum may be similar to the effect of baryons. The purpose of this letter is, using the recent precise CMB data from WMAP [14], to set an upper limit on the fraction of millicharged particles in CDM and to narrow the allowed window for millicharged particles. Assuming the standard Big Bang nucleosynthesis (BBN) value for the baryon abundance, $\Omega_b h_0^2 = 0.0214 \pm 0.0020$ [15], we arrive at the following constraint on the millicharged particle abundance,

$$\Omega_{mcp}h_0^2 < 0.007 \text{ (95\% CL)}, \qquad (1)$$

[¶] This article was submitted by the authors in English.
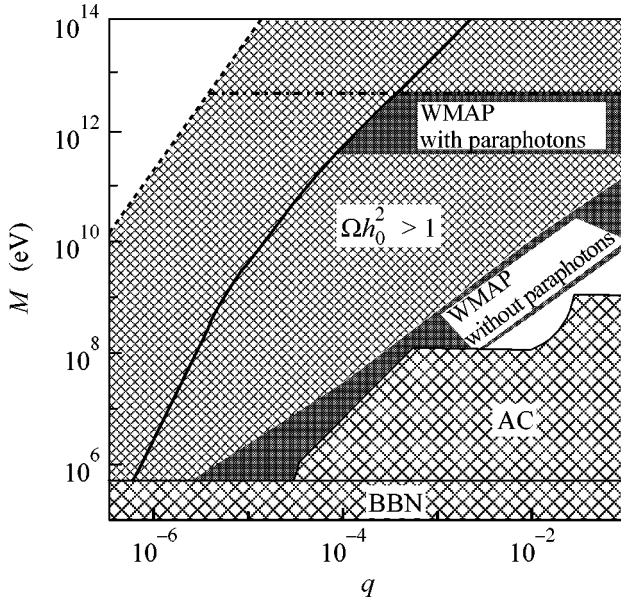
Fig. 1. The exclusion plot in the parameter space for millicharged particles. Light dashed area is excluded by accelerator experiments and BBN. Dashed region is excluded by the relic abundance of millicharged particles in models without paraphotons. Part of this region above the dash–dotted line is excluded by the relic abundance in models with paraphotons (assuming $\alpha' = 0.1$). On the left of the dotted line, millicharged particles cannot be thermally produced in the Early Universe. Dark gray areas are the previously allowed regions which are now excluded by Eq. (1) in models without and with paraphotons. On the right of the dark solid line, millicharged particles are coupled to baryons (see Eq. (8) in the text).

if millicharged particles are coupled to baryons during recombination. The latter condition is satisfied on the right of the dark solid line in Fig. 1. We see that the upper limit (1) applies to the whole allowed window for millicharged particles in models without paraphotons. It is also worth stressing that, in models with paraphotons, the domain of applicability of the upper bound (1) does not depend on the value of α'. Using the Lee–Weinberg formula [16] for the relic abundance, one then translates the upper bound (1) into the lower limit on the annihilation cross section of millicharged particles. As a result, the upper bound (1) excludes most of the allowed window for the millicharged particles in models without paraphotons, leaving a small allowed region with masses in the range $m \sim 10^{-1}$–10 GeV and charges in the range $q \sim 10^{-3}$–10^{-1}. In models with paraphotons, bound (1) translates into meaningful limit on the parameters of millicharged particles, as shown in Fig. 1; the excluded region depends on the value of α'.

Let us proceed to the derivation of the upper bound (1). To calculate the CMB anisotropy spectrum, we adapt the CMBFAST code [17], which numerically solves the set of kinetic equations [18] for the linear perturbations in the primordial plasma. To take into account the presence of millicharged particles, we extend this set by

adding the kinetic equations for the millicharged component, modify the equations for the baryon component to take into account the elastic scattering off millicharged particles, and include the millicharged component contribution to the energy-momentum tensor. The rest of the perturbation equations are the same as in [18]. The Compton scattering off millicharged particles is negligible, since the corresponding cross section is suppressed by the fourth power of the charge q.

We work in synchronous gauge and consider primordial plasma in the expanding Universe with scale factor $a(\tau)$ (where τ is conformal time) normalized to unity at present time. Let T_f, ρ_f, $\mathbf{v}_f$ be the temperature, density and velocity of the fth component of the plasma. In particular, $f = e, b, \gamma, mcp$ for electrons, baryons, photons, and millicharged particles, respectively. In what follows, a bar denotes space averaging. The standard variables describing fluid perturbations are $\delta_f(\mathbf{k}, \tau) = [\rho_f(\mathbf{k}, \tau) - \bar{\rho}_f(\tau)]/\bar{\rho}_f(\tau)$ and $\theta_f(\mathbf{k}, \tau) = ik_j v_f^j(\mathbf{k}, \tau)$, where k_i is conformal momentum.

Before recombination, the interaction between non-relativistic electrons and protons is strong enough to ensure that electron and baryon components have equal velocities, $\theta_e = \theta_b$. This makes it possible to use tight coupling approximation and consider electrons and protons as a single baryon fluid [19]. Then, the set of equations for baryons and millicharged particles reads (cf. [18])

$$\dot{\delta}_b = -\theta_b - \frac{1}{2}\dot{h},$$

$$\dot{\theta}_b = -\frac{\dot{a}}{a}\theta_b + c_s^2 k^2 \delta_b + \frac{4\bar{\rho}_\gamma}{3\bar{\rho}_b}an_e\sigma_T(\theta_\gamma - \theta_b) \qquad (2)$$

$$+ a\Gamma_{mcp}\Omega_{mcp}(\theta_{mcp} - \theta_b),$$

$$\dot{\delta}_{mcp} = -\theta_{mcp} - \frac{1}{2}\dot{h},$$

$$\dot{\theta}_{mcp} = -\frac{\dot{a}}{a}\theta_{mcp} + c_{s,mcp}^2 k^2 \delta_{mcp} \qquad (3)$$

$$+ a\Gamma_{mcp}\Omega_b(\theta_b - \theta_{mcp}),$$

where h is the longitudinal metric perturbation; the dot stands for derivative with respect to the conformal time τ; c_s, $c_{s,mcp}$ are the sound velocities in the baryon and millicharged components; n_e is the number density of electrons; and Γ_{mcp} is the velocity transfer rate for millicharged particles due to scattering off baryons and electrons. The latter is given by

$$\Gamma_{mcp} = \sum_{x=e,p} \frac{n_x}{\Omega_b}\frac{\partial}{\partial v_{M,x}}\left\langle \int \Delta v_M d\sigma_{M,x}\right\rangle\bigg|_{v_{M,x}=0}, \qquad (4)$$

where brackets stand for thermal averaging, $v_{M,e(p)}$ is relative velocity, and Δv_M is velocity transfer in a single

process of scattering; $d\sigma_{M,e}$ ($d\sigma_{M,p}$) is the Rutherford cross section for millicharged particles scattering off electron (proton).

The Rutherford cross section is singular at zero scattering angle, but due to Debye screening, the integral in Eq. (4) is cut at the value of the scattering angle equal to the Debye angle, $\theta_D = \sqrt{2\pi\alpha n_e / T^2 m_e}$. As a result, one arrives at the following expression for the velocity transfer rate in the case of thermal equilibrium:

$$\Gamma_{mcp} = \frac{4\sqrt{2\pi}\alpha^2 q^2 \rho_{crit}}{3 M m_p a^{3/2}(\tau)T_0^{3/2}}|\ln\theta_D|(\sqrt{\mu_{M,e}} + \sqrt{\mu_{M,p}}), \quad (5)$$

where $\mu_{M,e(p)}$ is the reduced mass of a millicharged particle and electron (proton), α is the fine structure constant, and $T_0 \approx 2.726$ K is the present CMB temperature. It is straightforward to generalize Eq. (5) to the non-equilibrium case when electrons, protons, and millicharged particles have different temperatures. In that case, the value of Γ_{mcp} is larger than the one given by Eq. (5), so Eq. (5) may be used as a lower estimate of the interaction rate, which is sufficient for our purposes.

We solve the system of the kinetic equations starting from the early moment of time τ_i and using inflationary initial conditions [18],

$$\delta_{mcp} = \delta_b = \frac{3}{4}\delta_\gamma = -\frac{1}{2}C(k\tau_i)^2,$$

$$\theta_{mcp} = \theta_\gamma = \theta_b = -\frac{1}{18}Ck(k\tau_i)^3,$$

where constant C determines the overall normalization.

The last terms in the right-hand side of Eqs. (2), (3) tend to equalize the velocities of the baryon and millicharged components of the fluid. This results in the kinetic equilibrium, $\theta_{mcp} = \theta_b$, provided Γ_{mcp} is large enough. In this case, the perturbation equations are difficult to solve numerically, because the kinetic relaxation rate for the interaction of millicharged particles and baryons is much larger than the rates of other processes. To deal with this situation, we make use of the zeroth order tight coupling approximation, adopting the method of Peebles and Yu [19]. Namely, we expand Eqs. (2), (3) to the zeroth order in Γ_{mcp}^{-1}, setting $\theta_b = \theta_{mcp} = \theta$. Then, we exclude Γ_{mcp} from Eqs. (2), (3) and arrive at the following equation:

$$\dot{\theta} = -\frac{\dot{a}}{a}\theta + \frac{\Omega_b}{\Omega_b + \Omega_{mcp}}\frac{4\bar{\rho}_\gamma}{3\bar{\rho}_b}an_e\sigma_T(\theta_\gamma - \theta)$$
$$+ \frac{\Omega_b c_s^2 \delta_b + \Omega_{mcp}c_{s,mcp}^2 \delta_{mcp}}{\Omega_b + \Omega_{mcp}}k^2. \quad (6)$$

The ranges of the cosmological parameters used in simulations; we never have a good fit outside the region $n_s \in [0.8, 1.2]$, and for $\Omega_{mcp} > 0.02$

Parameter	Min. value	Max. value	Step	Reference
Ω_{CDM}	0.2	0.4	0.01	PDG [12]
h_0	0.64	0.79	0.01	PDG [12]
n_s	0.8	1.2	0.01	
$\Omega_b h_0^2$	0.0194	0.0234	0.0005	BBN [15]
Ω_{mcp}	0	0.020	0.001	

The CMB spectrum obtained in this approximation agrees with the solution of the original set of equations at the level of one percent, provided that

$$\Gamma_{mcp}(\tau_{rec})(\Omega_b + \Omega_{mcp})H(\tau_{rec})^{-1} \gtrsim 250, \quad (7)$$

where τ_{rec} is conformal time at recombination and $H(\tau_{rec})$ is the Hubble parameter. In what follows, we discuss a region of parameters where tight coupling condition (7) is satisfied (in particular, this region covers the whole allowed window in models without paraphotons) and comment on the rest of the parameter space in due course.

To compare the results of our simulation with the CMB data, we consider the flat ΛCDM model with the number of massless neutrino species $N_\nu = 3$. We perform a scan over the space of the cosmological models by varying parameters from minimal to maximal values as given in the table. All priors are at 95% CL.

We assume the helium fraction at the moment of recombination $Y_{He} = 0.24$. We have checked that reionization effects are irrelevant here, the reason being that reionization affects the spectrum only at the lowest values of the multipole moments.

For each cosmological model, we calculated the likelihood to the WMAP data [14]. As a result, we arrived at the limit given by Eq. (1), which means that no model exists in the considered parameter range with larger values of $\Omega_{mcp}h_0^2$ and likelihood better than 5%.

We also checked that additional CMB data from CBI [20] and ACBAR [21] do not improve the limit (1).

Using the Lee–Weinberg formula we translate the limit given by Eq. (1) into the bound on the parameter space. The corresponding excluded areas are shown in Fig. 1. In models with paraphotons, we extend our analysis to the region where the tight coupling condition (7) is not satisfied. We checked that the upper bound (1) actually applies provided that the following less restrictive condition holds

$$\Gamma_{mcp}(\tau_{rec})(\Omega_b + \Omega_{mcp})H(\tau_{rec})^{-1} \gtrsim 2.5. \quad (8)$$

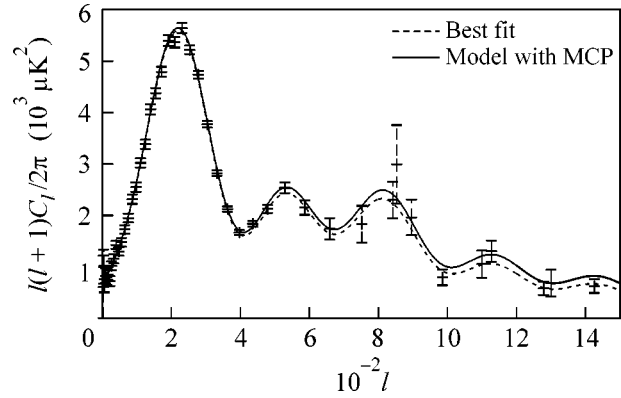This inequality is true on the right of the black solid line in Fig. 1.
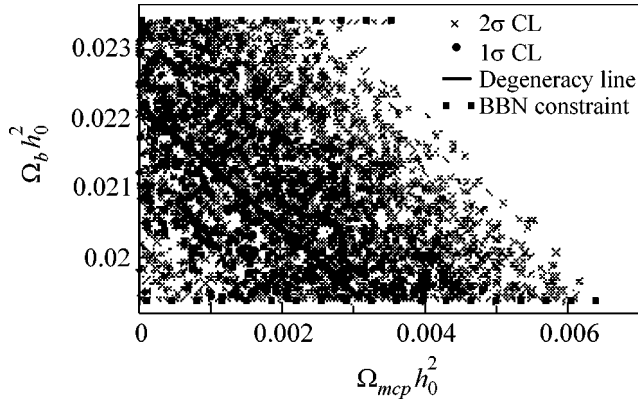
Fig. 2. Distribution of models in the $(\Omega_b h_0^2, \Omega_{mcp} h_0^2)$ plane. Crosses and dots denote models agreeing with data at the 2σ and 1σ CL, respectively. The bold line illustrates the degeneracy of the CMB anisotropy spectrum. Two dotted lines show the range of $\Omega_b h_0^2$ allowed by BBN.

Fig. 3. Two different CMB anisotropy spectra compared with extended WMAP dataset. Solid line represents the best fit model without millicharged particles, $\Omega_b h_0^2 = 0.022$. Dashed line corresponds to model with $\Omega_b h_0^2 = 0.014$, $\Omega_{mcp} h_0^2 = 0.007$.

Coming back to the tight coupling regime, let us illustrate the upper bound (1) pictorially by generating a set of models with random parameters in tight coupling regime, assuming uniform distribution of models in the parameter space within ranges given in the table. For each model, we calculated likelihood to the observed CMB spectrum and plot the resulting distribution of models in the $(\Omega_b h_0^2, \Omega_{mcp} h_0^2)$ plane in Fig. 2. One observes that the CMB spectrum is approximately degenerate along the straight line

$$\Omega_b h_0^2 = 0.022 - 1.1 \Omega_{mcp} h_0^2. \tag{9}$$

This degeneracy is in agreement with the expectation of [13] that the effect of millicharged particles is similar to that of baryons. Thus, in models with millicharged particles, the CMB data [14] determine actually the sum $(\Omega_b + \Omega_{mcp}) h_0^2 = 0.022 \pm 0.001$ (68% CL). Combining this value with the lower limit $\Omega_b h_0^2 > 0.019$ from BBN one arrives at the upper bound very similar to Eq. (1). This serves as a qualitative explanation of our result.

Another illustration of the approximate degeneracy (9) is shown in Fig. 3, where two CMB anisotropy spectra calculated for different models on the degeneracy line are shown. One observes that the two spectra almost coincide in the region of the first and second acoustic peaks. However, the degeneracy is no longer present at higher multipoles. This is due to the fact that the electroneutrality of the plasma implies that the electron number density is proportional to the baryon density. Hence, replacing a certain amount of baryons by millicharged particles results in the enhancement of the Silk damping at small scales. With future precise data for high values of l, one will be able to set a constraint on the value of Ω_{mcp} using the CMB data only, without

reference to BBN results. To check this, we created a simulated dataset, which contains the same values of l as in the WMAP data up to $l = 500$, and then, with the step $\Delta l = 50$ up to $l = 1600$. The CMB anisotropy spectral coefficients C_l's were taken from the best fit [14] to WMAP data. The error bars for these coefficients were assumed to be equal to cosmic variance. Repeating the above procedure for this dataset, we found that an upper limit $\Omega_{mcp} h_0^2 < 0.003$ can be placed. Further improvement of this limit turns out to be impossible due to the new approximate degeneracy,

$$\begin{aligned} \Omega_b h_0^2 &= 0.002 - 0.65 \Omega_{mcp} h_0^2, \\ n_s &= 0.94 + 8.0 \Omega_{mcp}, \end{aligned} \tag{10}$$

arising at smaller values of $\Omega_{mcp} h_0^2$.

To conclude, we note that, when translated into the parameter space, the limit (1) is especially interesting for the models without paraphotons, where it excludes most of the window with not very heavy particles and substantial electric charges. To completely close the window, sensitivity to millicharged particle abundance at the level of $\Omega_{mcp} h_0^2 \sim 3 \times 10^{-4}$ would be required, which cannot be achieved with future CMB experiments due to the degeneracy (10). Determination of the baryon abundance from the BBN is not accurate enough to improve the situation. Hopefully, the rest of the window will be explored by future accelerator and/or laboratory experiments.

Finally, it was recently suggested [22] that the flux of the 511-keV γ rays from the Galactic bulge detected by the INTEGRAL satellite [23] may be explained by the annihilation of the ~1–100 MeV dark matter particles into $e^+ e^-$ pairs, provided their

annihilation cross section $\sigma\beta$ and abundance Ω satisfy $(\sigma\beta/\text{pb})(1\ \text{MeV}/M)^2(\Omega^2/\Omega_{\text{CDM}}^2) \simeq 10^{-(3.5-4.5)}$. Intriguingly, this condition holds in the left corner of the parameter space for millicharged particles without paraphoton allowed by Eq. (1) (say, for $q = 3 \times 10^{-3}$, $M = 100$ MeV). One is tempted to speculate that the observation of the 511 keV line is an indication that a (small) fraction of CDM is comprised of millicharged particles. This possibility will be checked by future CMB data.

REFERENCES

1. L. B. Okun, M. B. Voloshin, and V. I. Zakharov, Phys. Lett. B **138B**, 115 (1984).

2. B. Holdom, Phys. Lett. B **166B**, 196 (1986).

3. A. Y. Ignatev, V. A. Kuzmin, and M. E. Shaposhnikov, Phys. Lett. B **84B**, 315 (1979).

4. M. I. Dobroliubov and A. Y. Ignatev, Phys. Rev. Lett. **65**, 679 (1990).

5. S. Davidson, B. Campbell, and D. C. Bailey, Phys. Rev. D **43**, 2314 (1991).

6. S. Davidson and M. E. Peskin, Phys. Rev. D **49**, 2114 (1994); hep-ph/9310288.

7. A. A. Prinz, R. Baggs, J. Ballam, *et al.*, Phys. Rev. Lett. **81**, 1175 (1998).

8. S. Davidson, S. Hannestad, and G. Raffelt, J. High Energy Phys. **05**, 003 (2000).

9. R. N. Mohapatra and I. Z. Rothstein, Phys. Lett. B **247**, 593 (1990); R. N. Mohapatra and S. Nussinov, Int. J. Mod. Phys. A **7**, 3817 (1992).

10. M. L. Perl, P. C. Kim, V. Halyo, *et al.*, Int. J. Mod. Phys. A **16**, 2137 (2001).

11. H. Goldgberg and L. J. Hall, Phys. Lett. B **174**, 151 (1986).

12. K. Hagiwara, K. Hikasa, K. Nakamura, *et al.* (Particle Data Group), Phys. Rev. D **66**, 010001 (2002).

13. S. L. Dubovsky and D. S. Gorbunov, Phys. Rev. D **64**, 123503 (2001).

14. D. N. Spergel, L. Verde, H. V. Peiris, *et al.*, Astrophys. J., Suppl. Ser. **148**, 175 (2003).

15. D. Kirkman, D. Tytler, N. Suzuki, *et al.*, astro-ph/0302006.

16. B. W. Lee and S. Weinberg, Phys. Rev. Lett. **39**, 165 (1977).

17. U. Seljak and M. Zaldarriaga, Astrophys. J. **469**, 437 (1996); http://www.cmbfast.org/.

18. C.-P. Ma and E. Bertschinger, Astrophys. J. **455**, 7 (1995).

19. P. J. E. Peebles and J. T. Yu, Astrophys. J. **162**, 815 (1970).

20. T. J. Pearson, B. S. Mason, A. C. S. Readhead, *et al.*, Astrophys. J. **591**, 556 (2003).

21. C. L. Kuo, P. A. R. Ade, J. J. Bock, *et al.* (ACBAR Collaboration), astro-ph/0212289.

22. C. Boehm, D. Hooper, J. Silk, and M. Casse, astro-ph/0309686.

23. J. Knodlseder, V. Lonjou, P. Jean, *et al.*, astro-ph/0309442; P. Jean, J. Knoedlseder, V. Lonjou, *et al.*, Astron. Astrophys. **407**, L55 (2003).

Double Beta Decay of ^{150}Nd to the First 0^+ Excited State of ^{150}Sm¶

A. S. Barabash[1, *], F. Hubert[2], Ph. Hubert[2], and V. I. Umatov[1]

[1] *Institute of Theoretical and Experimental Physics, Moscow, 117259 Russia*
[2] *Centre d'Études Nucléaires, IN2P3-CNRS et Université de Bordeaux, F-33170 Gradignan, France*
**e-mail: Alexander.Barabash@itep.ru*

Two neutrino double beta decay of ^{150}Nd to the first 0^+ excited state in ^{150}Sm is investigated with the 400 cm^3 low-background HPGe detector. Data analysis for 11 320.5 h shows the excess of events at 333.9 and 406.5 keV. This makes it possible to estimate the half-life of the investigated process as $[1.4^{+0.4}_{-0.2}(\text{stat}) \pm 0.3(\text{syst})] \times 10^{20}$ yr. © 2004 MAIK "Nauka/Interperiodica".

PACS numbers: 23.40.Hc; 23.40.Bw

The neutrinoless double beta ($0\nu\beta\beta$) decay is allowed if neutrino mixing, involving the electron neutrino ν_e, is present in the weak charged lepton current and the neutrinos with definite mass are Majorana particles (see, e.g., [1]). Strong evidence for neutrino mixing, i.e., for oscillations of solar electron neutrinos ν_e driven by nonzero neutrino masses and neutrino mixing, have been obtained in solar neutrino experiments (see review [2]): Davis *et al.* (Homestake) experiment and in Kamiokande, SAGE, GALLEX/GNO, and Super-Kamiokande. This evidence has been spectacularly reinforced during the last two years by the data from the SNO solar neutrino [3–5] and KamLAND reactor antineutrino [6] experiments. This very exciting result has greatly renewed the interest in $0\nu\beta\beta$ decay. This process is the most sensitive to the possible Majorana nature of massive neutrinos. Their detection will give information on the absolute scale of neutrino masses and their type of hierarchy (normal, inverted, and quasi-generated), and under specific conditions of the CP violation in the lepton sector (see review [2]).

One of the problems in $0\nu\beta\beta$ decay physics is the reliable evaluation of nuclear matrix elements having an accuracy of a factor of two to three up to date. In connection with the $0\nu\beta\beta$ decay, the detection of double beta decay with the emission of two neutrinos ($2\nu\beta\beta$), which is an allowed process of second order in the Standard Model, enables the experimental determination of nuclear matrix elements involved in the double beta decay processes. Accumulation of experimental information for the $2\nu\beta\beta$ processes (transitions to the ground and excited states) promotes a better understanding of the nuclear part of double beta decay and allows one to check theoretical schemes of nuclear matrix element calculations for the two neutrino mode, as well as for the neutrinoless one.

The $\beta\beta$ decay can proceed through transitions to the ground state, as well as to various excited states of the daughter nuclide. Studies of the latter transitions allow one to obtain supplementary information about $\beta\beta$ decay [7]. Because of smaller transition energies, the probabilities for $\beta\beta$-decay transitions to excited states are substantially suppressed in comparison with transitions to the ground state. However, as it was shown [8], by using low-background HPGe detectors, the $2\nu\beta\beta$ decay to the 0^+_1 level in the daughter nucleus may be detected for such nuclei as ^{100}Mo, ^{96}Zr, and ^{150}Nd. In this case, the energies involved in the $\beta\beta$ transitions are large enough (1903, 2202, and 2627 keV, respectively) and the expected half-lives are of the order of 10^{20}–10^{21} yr. The sensitivity required for detection was only reached for ^{100}Mo, and the transition was detected in the three experiments [9–11] with the half-life lying within (6–9) $\times 10^{20}$ yr (the average value is $(6.8 \pm 1.2) \times 10^{20}$ yr) [12]. Recently, additional isotopes, ^{82}Se, ^{130}Te, ^{116}Cd, and ^{76}Ge, have become of interest in studies of the $2\nu\beta\beta$ decay to the 0^+_1 level too (see review [13]).

Theoretical estimates of the $2\nu\beta\beta$ decay to a 2^+ excited state have shown that, for a few nuclei (^{82}Se, ^{96}Zr, ^{100}Mo, and ^{130}Te), the half-lives can be ~10^{22}–10^{23} yr [7]. This would mean that the detection of such decays becomes possible using present and new installations in the near future.

It is very important to note that, in the framework of QRPA models, the behavior of nuclear matrix elements with parameter g_{pp} is completely different for transitions to the ground and excited (2^+ and 0^+) states [7, 14]. This is why the decay to excited states may probe different aspects of the calculational method than the decay to the ground states. So, the search for $\beta\beta$ transitions to the excited states has its own special interest.

¶ This article was submitted by the authors in English.

In this article, results of an experimental investigation of the ββ decay of ^{150}Nd to the first 0⁺ excited state in ^{150}Sm are presented. The decay scheme is shown in Fig. 1. A search for ββ transitions of ^{150}Nd to the first 0⁺ excited state in ^{150}Sm has been carried out using a germanium detector to look for γ-ray lines corresponding to the decay scheme.

The experimental work was performed in the Modane Underground Laboratory (depth of 4800 m w.e.). A 400 cm³ low-background HPGe detector was used for investigation of 3046 g Nd$_2$O$_3$ powder placed in a special Marinelli delrin box which was put on the detector endcap. Taking into account the natural abundance (5.64%), 153 g of ^{150}Nd was exposed. The data collected for 11 320.5 h were used for analysis.

The HPGe detector was surrounded by a passive shield consisting of 2 cm of archeological lead, 10 cm of OFHC copper, and 15 cm of ordinary lead. To reduce the ^{222}Rn gas, which is one of the main sources of the background, special efforts were made to minimize the free space near the detector. In addition, the passive shield was enclosed in an aluminum box flushed with high-purity nitrogen. The cryostat, the endcap, and the critical mechanical components of the HPGe detector were made of very pure Al–Si alloy. Finally, the cryostat had a J-type geometry to shield the crystal from possible radioactive impurities in the dewar.

The electronics consisted of currently available spectrometric amplifiers and an 8192 channel ADC. The energy calibration was adjusted to cover the energy range from 50 keV to 3.5 MeV. The energy resolution was 1.9 keV for the 1332 keV line of ^{60}Co. The electronics were stable during the experiment due to the constant conditions in the laboratory (temperature of 23°C, hygrometric degree of 50%). A daily check on the apparatus functioning was made.

The detection photopeak efficiencies were equal to 2.33% at 333.9 keV and 2.33% at 406.5 keV. The efficiencies were computed with the CERN Monte Carlo code GEANT3.21. Special calibration measurements with radioactive sources and powders containing well-known ^{226}Ra activities confirmed that the accuracy of these efficiencies is about 10%.

The dominate detector backgrounds come from natural ^{40}K, radioactive chains of ^{232}Th and ^{235,238}U, man-made and/or cosmogenic activities of ^{137}Cs and ^{60}Co. The sample was found to have considerable activity of ^{40}K (46.3 mBq/kg). Additionally, long-lived radioactive impurities were observed in the sample but with much weaker activities. In our case, the most important isotopes contributing to energy ranges of the investigated transition are ^{214}Bi (1.15 mBq/kg), ^{228}Ac (0.93 mBq/kg), ^{227}Ac (0.62 mBq/kg), and their daughters.

Figures 2 and 3 show the energy spectrum in the ranges of interest. As one can see, there is an excess of events above continuous background at the investigated
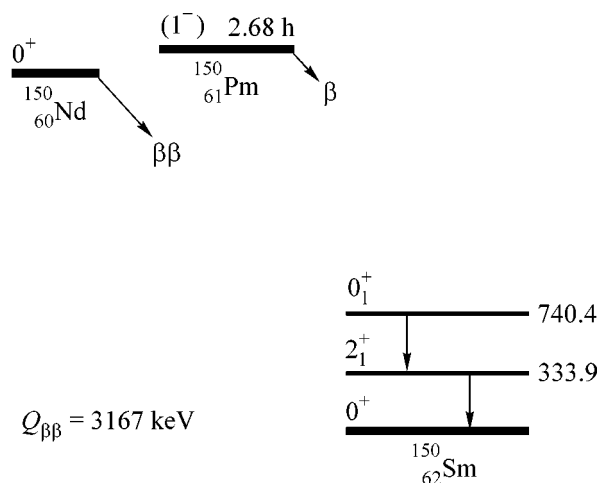

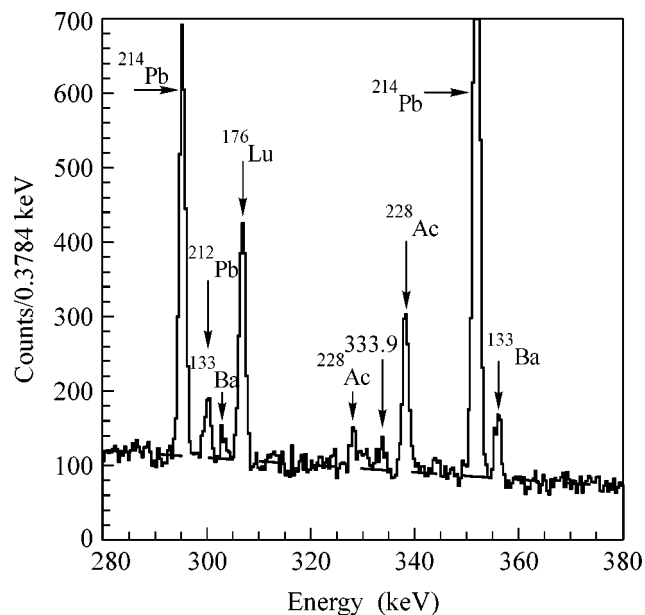**Fig. 1.** Decay scheme of ^{150}Nd. Energies of levels are in keV.

Fig. 2. Energy spectrum in the range of 333.9 keV. Dashed line is continuous background used in the analysis.

energies. Isotopes of natural radioactivity (^{211}Pb, ^{214}Bi, ^{227}Th, and ^{228}Ac), found in the spectrum, have γ lines near these energies. ^{214}Bi contributes to both investigated ranges through γ rays with energies of 333.31 (0.080%) and 334.78 keV (0.034%) for the 333.9 keV peak and 405.74 keV (0.17%) for the 406.5 keV peak. ^{228}Ac touches the 333.9 keV peak range with its γ (332.37 keV, 0.40%). ^{227}Ac exhibits through its daughters, ^{227}Th (334.37 keV, 1.14%) and ^{211}Pb (404.853 keV, 3.78%). There is also the artificial isotope, ^{150}Eu ($T_{1/2} = 36.9$ yr), decaying to the same daughter, ^{150}Sm, with γ rays of 333.9 (96%), 406.5 (0.14%), 439.4 (80%), and 584.3 keV (52.6%). However, its possible exhibition at
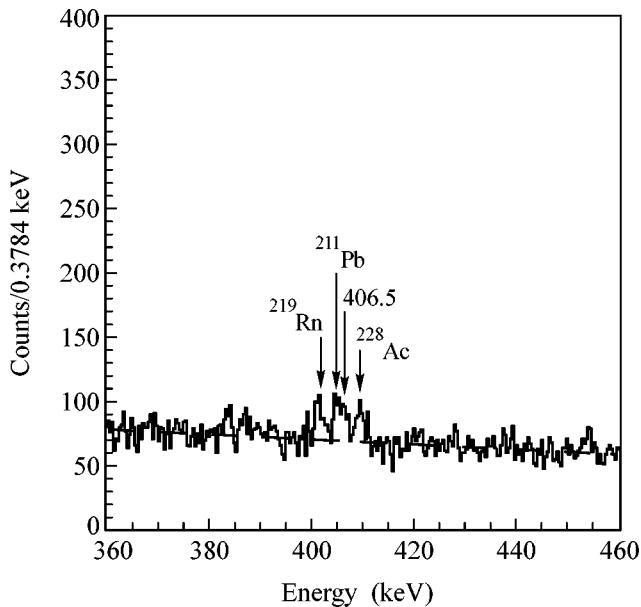
Analysis of events in the range of peaks under study

Peak	333.9 ± 1.12			406.5 ± 1.12	
Number of events	779			603	
Continuous background	656.6			484.5	
Isotopes	^{214}Bi	^{227}Th	^{228}Ac	^{214}Bi	^{211}Pb
E_γ, keV	333.1; 334.78	334.37	332.37	405.74	404.853
Contributions from isotopes	8.8	22.6	5.4	9.7	8.7
Excess of events	86 ± 28			100 ± 25	

439.4 keV is within standard deviation of continuous background; therefore, it can be taken into account as a systematic error.

The table presents the results of the analysis for the two peak energy ranges under study. A peak shape is described as a Gaussian with a standard deviation of ~0.56 keV at the energies investigated. For the analysis, a peak range is taken within four standard deviations ($E \pm 2\sigma$), i.e., 0.9545 of a peak area. As one can see, there is an excess of events for each peak under study. Summing the two peaks gives (186 ± 38) events, which corresponds to about the 5σ positive effect. Finally, we can estimated the half-life of the 2νββ decay of ^{150}Nd to the first 0^+ excited state of ^{150}Sm as $T_{1/2} = [1.4^{+0.4}_{-0.2}(\text{stat}) \pm 0.3(\text{syst})] \times 10^{20}$ yr.

Previous experiments gave only limits on this transition, $>1 \times 10^{20}$ yr [15] and $>1.5 \times 10^{20}$ yr [16]. Taking into account all errors, our result is not in contradiction with the previous limits.

If one compares our result with the average experimental value of the half-life for the 2νββ transition of ^{150}Nd to the ground state, $T_{1/2} = (7.0 \pm 1.7) \times 10^{18}$ yr [12], and take into account phase space factors [7], then one can obtain for nuclear matrix elements the following ratio, $M^{2\nu}_{\text{g.s.}} \approx 1.4 M^{2\nu}_{0^+_1}$. So, the nuclear matrix element for the transition to the first 0^+ excited level is a little less than one for the transition for the ground state.

REFERENCES

1. S. M. Bilenky and S. T. Petcov, Rev. Mod. Phys. **59**, 671 (1987).
2. S. M. Bilenky, C. Guinti, J. A. Grifols, and E. Masso, Phys. Rep. **379**, 69 (2003).
3. Q. R. Ahmad, R. C. Allen, T. C. Andersen, *et al.*, Phys. Rev. Lett. **87**, 071301 (2001).
4. Q. R. Ahmad, R. C. Allen, T. C. Andersen, *et al.*, Phys. Rev. Lett. **89**, 011301 (2002); Q. R. Ahmad, R. C. Allen, T. C. Andersen, *et al.*, Phys. Rev. Lett. **89**, 011302 (2002).
5. SNO Collaboration, nucl-ex/0309004.
6. K. Eguchi, S. Enomoto, K. Furuno, *et al.*, Phys. Rev. Lett. **90**, 021802 (2003).
7. J. Suhonen and O. Civitarese, Phys. Rep. **300**, 123 (1998).
8. A. S. Barabash, JETP Lett. **51**, 207 (1990).
9. A. S. Barabash, F. T. Avignone III, J. I. Collar, *et al.*, Phys. Lett. B **345**, 408 (1995).
10. A. S. Barabash, R. Gurriaran, F. Hubert, *et al.*, Phys. At. Nucl. **62**, 2039 (1999).
11. L. De Braeckeleer, M. Hornish, A. S. Barabash, and V. I. Umatov, Phys. At. Nucl. **63**, 1214 (2000).
12. A. S. Barabash, Czech. J. Phys. **52**, 567 (2002).
13. A. S. Barabash, Czech. J. Phys. **50**, 447 (2000).
14. M. Aunola and J. Suhonen, Nucl. Phys. A **602**, 133 (1996).
15. C. Arpesella, L. Zanotti, E. Bellotti, and N. Ferrari, Nucl. Phys. B (Proc. Suppl.) **70**, 249 (1999).
16. A. A. Klimenko, S. B. Osetrov, A. A. Smolnikov, and S. I. Vasiliev, Czech. J. Phys. **52**, 589 (2002).

Fig. 3. Energy spectrum in the range of 406.5 keV. Dashed line is continuous background used in the analysis.

The Evaluation of the Branching Ratios of the Decays
φ(1020) ⟶ 2π⁺2π⁻π⁰, π⁺π⁻3π⁰[¶]

N. N. Achasov and A. A. Kozhevnikov

Laboratory of Theoretical Physics, Sobolev Institute for Mathematics, Novosibirsk, 630090 Russia
e-mail: achasov@math.nsc.ru, kozhev@math.nsc.ru
Received November 20, 2003

Combining the Okubo–Zweig–Iizuka rule in the decay $\phi \longrightarrow \rho\pi \longrightarrow \pi^+\pi^-\pi^0$ with the $\rho \longrightarrow 4\pi$ decay amplitudes, we calculate the $\phi \longrightarrow 2\pi^+2\pi^-\pi^0$ and $\phi \longrightarrow \pi^+\pi^-3\pi^0$ ones. The partial widths of the above ϕ decays are evaluated, and the excitation curves in e^+e^- annihilation are obtained, assuming reasonable particular relations among the parameters characterizing the anomalous terms of the HLS Lagrangian. The evaluated branching ratios $B_{\phi \to \pi^+\pi^-3\pi^0} \approx 2 \times 10^{-7}$ and $B_{\phi \to 2\pi^+2\pi^-\pi^0} \approx 7 \times 10^{-7}$ are such that, with the luminosity $L = 500$ pb^{-1} attained at DAΦNE φ factory, one may already possess about 1685 events of the decays $\phi \longrightarrow 5\pi$. © *2004 MAIK "Nauka/Interperiodica".*

PACS numbers: 13.25.Jx

The decay of the φ(1020) meson to the state 3π occurs due to the violation of the Okubo–Zweig–Iizuka rule (OZI). The decay $\phi \longrightarrow 5\pi$, expected to proceed due to the violation of this rule, should be dominated by the process $\phi \longrightarrow \rho\pi$ followed by the decay $\rho \longrightarrow 4\pi$, whose amplitudes and decay width were calculated in, e.g., [1]. See the diagram in Fig. 1a. The ρ meson in these diagrams is resonant. Indeed, choosing the averaged pion energy from the condition of "equilibrium" as $\langle E_\pi \rangle = m_\phi/5$, one finds that the invariant mass of four pions emitted in the transition $\rho \longrightarrow 4\pi$ is $m_{4\pi} \simeq m_\rho$. The seemingly resonant diagrams Fig. 1b and 1d do not, in fact, possess this property, because three pions produced either from the transition $\pi \longrightarrow \pi\pi\pi$ or directly from the $\phi \longrightarrow \rho\pi\pi\pi$ transition push ρ meson away from the resonance. Indeed, the invariant mass of the pion pair in the transition $\rho \longrightarrow 2\pi$ evaluated assuming the same average pion energy as above falls into the interval $2m_\pi \leq m_{2\pi} \leq 0.41$ GeV, which is far from the resonance value. The contribution of the diagram in Fig. 1e containing the OZI-suppressed vertex $\phi\rho\rho\pi$ is, at the φ mass, deeply under the threshold of the production of two ρ mesons and because of this is also suppressed. The two diagrams in Fig. 1c, containing OZI-suppressed pointlike vertices $\phi \longrightarrow 5\pi$ and $\phi \longrightarrow 3\pi$, do not contain the intermediate ρ-meson at all and, hence, can be neglected in the approximation of the resonant ρ meson. The effect of relaxing these approximations is considered below.

There are two feasible models of the OZI-suppressed $\phi \longrightarrow \rho\pi$ decay amplitude. The first one is the φω mixing model [2], where the above decay proceeds due to the small admixture of nonstrange quarks in the flavor wave function of φ meson composed mostly of a pair of strange quarks. In the second model, φ goes to ρπ directly, see [3]. Irrespective of these models, the effective $\phi \longrightarrow \rho\pi$ coupling $g_{\phi\rho\pi}^{\text{eff}}$ in the diagram (Fig. 1a) is determined by the branching ratio of the well-studied process $\phi \longrightarrow \rho\pi \longrightarrow \pi^+\pi^-\pi^0$. Then, the contribution to the decay amplitude of the dominant diagram (Fig. 1a) for each isotopic mode, $2\pi^+2\pi^-\pi^0$ and $\pi^+\pi^-3\pi^0$, can be represented as
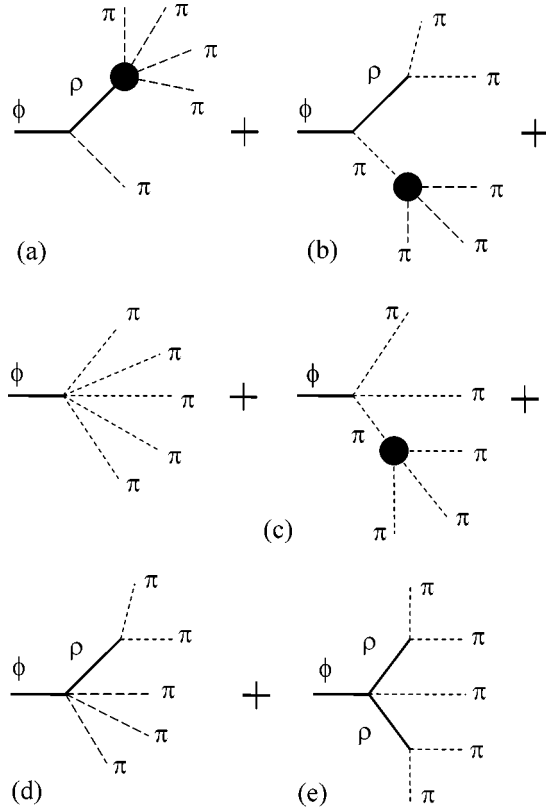
$$M = -\frac{g_{\phi\rho\pi}^{\text{eff}}g_{\rho\pi\pi}}{f_\pi^2}\varepsilon_{\mu\nu\lambda\sigma}\sum \frac{q_\mu\epsilon_\nu q_\lambda^\pi J_\sigma(\rho \longrightarrow 4\pi)}{D_\rho(q - q^\pi)}, \quad (1)$$

where the sum is over all possible permutations of the final pion momenta, q and ϵ are the four-momentum and polarization vector of the φ meson, and q^π is the four-momentum of the final pion in the decay $\phi \longrightarrow \rho\pi$. The coupling constant $g_{\rho\pi\pi}$ is calculated from the $\rho \longrightarrow \pi^+\pi^-$ decay width, and $f_\pi = 92.4$ MeV is the pion decay constant. The inverse propagator of the ρ meson is

$$D_\rho(q) = m_\rho^2 - q^2 - i\frac{g_{\rho\pi\pi}^2}{6\pi\sqrt{q^2}}\left(\frac{q^2}{4} - m_\pi^2\right)^{3/2}. \quad (2)$$

The expressions for the $\rho \longrightarrow 4\pi$ decay currents $J_\sigma(\rho \longrightarrow 4\pi)$ are given in [1]. The partial width of the decay $\phi \longrightarrow 5\pi$ is

$$\Gamma_{\phi \to 5\pi}(s) = \frac{1}{2\sqrt{s}(2\pi)^{11}N_{\text{sym}}}\int|M|^2 d\mathcal{D}_5, \quad (3)$$

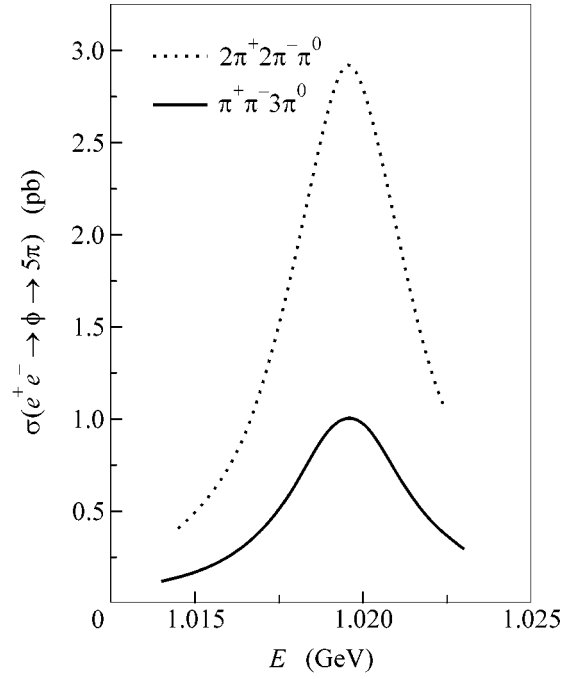[¶] This article was submitted by the authors in English.

Fig. 1. Diagrams describing the amplitudes of the decay $\phi(1020) \longrightarrow 5\pi$. The total set of diagrams for each isotopic final state $2\pi^+2\pi^-\pi^0$ and $\pi^+\pi^-3\pi^0$ should include all possible permutations of the final pion momenta. The shaded circle in (b), (c) [(a)] refers to the $\pi \longrightarrow 3\pi$ ($\rho \longrightarrow 4\pi$) vertex, which includes the ρ exchange. See [1].

Fig. 2. The excitation curve of the decays $\phi \longrightarrow 5\pi$ in e^+e^- annihilation.

where s is the total energy squared in the rest frame system of the decaying ϕ meson; the Bose symmetry factor $N_{\text{sym}} = 6, 4$ for the decay $\phi \longrightarrow \pi^+\pi^-3\pi^0$ and $\phi \longrightarrow 2\pi^+2\pi^-\pi^0$, respectively; and $d\mathcal{D}_5$ given in [4] is the differential element of the phase space volume of the five pion final state. Note that we take into account the mass difference of the charged and neutral pions both in amplitude and in the phase space volume.

The evaluation of the branching ratios with the resonant diagram (Fig. 1a) gives $B^{\text{resonant}}_{\phi \to \pi^+\pi^-3\pi^0} = 2.1 \times 10^{-7}$ and $B^{\text{resonant}}_{\phi \to 2\pi^+2\pi^-\pi^0} = 6.2 \times 10^{-7}$, where $B_{\phi \to 5\pi} \equiv \Gamma_{\phi \to 5\pi}(m_\phi^2)/\Gamma_\phi(m_\phi^2)$. The excitation curves for the $\phi \longrightarrow 5\pi$ decays in e^+e^- annihilation,

$$\sigma_{\phi \to 5\pi}(s)$$
$$= 12\pi\left(\frac{m_\phi}{\sqrt{s}}\right)^3 \Gamma_{\phi \to e^+e^-}(m_\phi^2)\frac{s\Gamma_{\phi \to 5\pi}(s)}{\left(s - m_\phi^2\right)^2 + m_\phi^2\Gamma_\phi^2} \qquad (4)$$

are plotted in Fig. 2. We take the fixed width approximation for the ϕ meson propagator, because this meson is narrow.

Let us discuss the role of the remaining diagrams in Fig. 1. To this end, one should write the effective Lagrangian for the decays $\phi \longrightarrow 3\pi$ and $\phi \longrightarrow 5\pi$ as

$$\mathcal{L}^{\text{an}}_{\phi,\rho,\pi} = \frac{1}{2f_\pi^3}(\beta_1 - \beta_2 - \beta_3)$$

$$\times \varepsilon_{\mu\nu\lambda\sigma}\phi_\mu(\partial_\nu\boldsymbol{\pi} \cdot [\partial_\lambda\boldsymbol{\pi} \times \partial_\sigma\boldsymbol{\pi}])$$

$$+ \frac{1}{8f_\pi^5}\left[-\beta_1 + \frac{5}{3}(\beta_2 + \beta_3)\right]$$

$$\times \varepsilon_{\mu\nu\lambda\sigma}\phi_\mu(\partial_\nu\boldsymbol{\pi} \cdot [\partial_\lambda\boldsymbol{\pi} \times \partial_\sigma\boldsymbol{\pi}])\boldsymbol{\pi}^2$$

$$- \frac{2\beta_3 g}{f_\pi}\varepsilon_{\mu\nu\lambda\sigma}\partial_\mu\phi_\nu\bigg\{(\boldsymbol{\rho}_\lambda \cdot \partial_\sigma\boldsymbol{\pi}) \qquad (5)$$

$$+ \frac{1}{6f_\pi^2}[(\boldsymbol{\rho}_\lambda \cdot \boldsymbol{\pi})(\boldsymbol{\pi} \cdot \partial_\sigma\boldsymbol{\pi}) - \boldsymbol{\pi}^2(\boldsymbol{\rho}_\lambda \cdot \partial_\sigma\boldsymbol{\pi})]\bigg\}$$

$$- \frac{2g}{f_\pi}(\beta_1 + \beta_2 - \beta_3)\varepsilon_{\mu\nu\lambda\sigma}\phi_\mu\bigg\{\frac{1}{4f_\pi^2}(\partial_\nu\boldsymbol{\pi} \cdot \boldsymbol{\rho}_\lambda)$$

$$\times (\boldsymbol{\pi} \cdot \partial_\sigma\boldsymbol{\pi}) - \frac{g}{4}([\boldsymbol{\rho}_\nu \times \boldsymbol{\rho}_\lambda] \cdot \partial_\sigma\boldsymbol{\pi})\bigg\},$$

where $\beta_{1,2,3}$ are arbitrary parameters responsible for the violation of the OZI rule in the $\phi \longrightarrow 5\pi$ decays, $g = g_{\rho\pi\pi}$. Expression (5) is written guided by the form of the anomalous contributions in the hidden local sym-

metry approach [5, 6]. As is evident from Eq. (5), the coupling constant of direct $\phi \longrightarrow \rho\pi$ transition is

$$g_{\phi\rho\pi} = -\frac{2\beta_3 g}{f_\pi} = 0.8 \text{ GeV}^{-1}. \qquad (6)$$

Since there is no sizeable pointlike $\phi \longrightarrow \pi^+\pi^-\pi^0$ contribution, see [7, 8], one can set

$$\beta_1 - \beta_2 - \beta_3 = 0. \qquad (7)$$

The results of relaxing this conditions are discussed at the end of the paper. After all, the ratio β_1/β_3 remains arbitrary. We set

$$\beta_1 + \beta_2 - \beta_3 = 0, \qquad (8)$$

hence, $\beta_1 = \beta_3$, $\beta_2 = 0$, so that the $\phi \longrightarrow 5\pi$ decay amplitudes are determined by only parameter β_3. The amplitudes in this case are very lengthy and given elsewhere [9]. The results of the evaluation are

$$\begin{aligned} B_{\phi \to \pi^+\pi^-3\pi^0}(m_\phi^2) &= 2.4 \times 10^{-7}, \\ B_{\phi \to 2\pi^+2\pi^-\pi^0}(m_\phi^2) &= 6.9 \times 10^{-7}. \end{aligned} \qquad (9)$$

The evaluation of the nonresonant contribution in Figs. 1b–1e gives $B_{\phi \to \pi^+\pi^-3\pi^0}^{\text{nonresonant}} = 0.34 \times 10^{-7}$, which constitutes 16% of the resonant contribution, and $B_{\phi \to 2\pi^+2\pi^-\pi^0}^{\text{nonresonant}} = 0.70 \times 10^{-7}$, which constitutes about 11% of the resonant one. The above estimates clearly illustrate the dominance of the diagrams with the resonant ρ meson in the intermediate state in the decay $\phi \longrightarrow 5\pi$, because the resonant and the smaller nonresonant contributions add incoherently in the case of the $\phi \longrightarrow 5\pi$ decay. Indeed, the phase space averaged relative phase between the resonant and nonresonant contributions calculated with the help of the given branching ratios is about $\delta = 91°$ in the decay $\phi \longrightarrow \pi^+\pi^-3\pi^0$ and $\delta = 89°$ in the $\phi \longrightarrow 2\pi^+2\pi^-\pi^0$. For comparison, the opposite situation takes place in the case of the $\omega \longrightarrow 5\pi$ decay amplitudes, where the smaller nonresonant contribution to the decay amplitude adds almost in phase with the resonant one and because of this is essential [9].

Relaxing constraint Eq. (8) to $-1 \le (\beta_1 + \beta_2 - \beta_3)/4\beta_3 \le 1$ implies the deviations of $B_{\phi \to 5\pi}$ by less than 1%. Relaxing the constraint of the absence of the pointlike $\phi \longrightarrow \pi^+\pi^-\pi^0$ amplitude, Eq. (7), gives the following. Using the KLOE data [8], one can estimate the combination characterizing the pointlike $\phi \longrightarrow \pi^+\pi^-\pi^0$ vertex as $|3(\beta_1 - \beta_2 - \beta_3)/2\beta_3 m_\rho^2| \simeq 1$. Then, the evaluation of $B_{\phi \to 5\pi}$ gives results deviating by $\pm 8\%$ (depending on the sign of the above combination) from those obtained under Eq. (7). All the above discussion shows that the branching ratios of the decays $\phi \longrightarrow \pi^+\pi^-3\pi^0$ and $\phi \longrightarrow 2\pi^+2\pi^-\pi^0$ are determined within the conservatively estimated accuracy 20% by the well-studied

OZI rule violating transition of ϕ meson to the $\rho\pi$ state followed by the transition $\rho \longrightarrow 4\pi$ in the model independent way.

The excitation curves of the decay $\phi \longrightarrow 5\pi$ in e^+e^- annihilation can be used to evaluate the expected number of these decays at the ϕ peak. With the luminosity $L = 10^{32}$ cm^{-2} s^{-1}, the observation of, respectively, 750 (250) $\phi \longrightarrow 2\pi^+2\pi^-\pi^0$ ($\phi \longrightarrow \pi^+\pi^-3\pi^0$) decays per month is feasible. Note that the existing upper limit is $B_{\phi \to 2\pi^+2\pi^-\pi^0} < 4.6 \times 10^{-6}$ (90% CL) [10]. With the luminosity $L = 500$ pb^{-1} already attained at ϕ factory DAΦNE [11], one could gain about 1685 events of the decay $\phi \longrightarrow 5\pi$ proceeding via chiral mechanisms considered in the present paper. The possible nonchiral-model background from the dominant decay $\phi \longrightarrow K_L K_S$, $K_L \longrightarrow 3\pi$, $K_S \longrightarrow 2\pi$ is well cut from the considered chiral mechanism by macroscopic distances kaons fly away. Rare decay $\phi \longrightarrow \eta\pi^+\pi^-$, whose branching ratio was estimated [12, 13] at the $B_{\phi \to \eta\pi^+\pi^-} \sim 3 \times 10^{-7}$, is cut by removing events in the vicinity of the η peak in the three pion distribution observed in the five pion events [10].

REFERENCES

1. N. N. Achasov and A. A. Kozhevnikov, Phys. Rev. D **62**, 056011 (2000); JETP **91**, 433 (2000).

2. S. Okubo, Phys. Lett. **5**, 165 (1963).

3. N. N. Achasov and A. A. Kozhevnikov, Phys. Rev. D **52**, 3119 (1995); Yad. Fiz. **59**, 153 (1996) [Phys. At. Nucl. **59**, 144 (1996)].

4. R. Kumar, Phys. Rev. **185**, 1865 (1969).

5. M. Bando, T. Kugo, S. Uehara, *et al.*, Phys. Rev. Lett. **54**, 1215 (1985); M. Bando, T. Kugo, and K. Yamawaki, Nucl. Phys. B **259**, 493 (1985); Prog. Theor. Phys. **73**, 1541 (1985); Phys. Rep. **164**, 217 (1988).

6. M. Harada and K. Yamawaki, Phys. Rep. **381**, 1 (2003); hep-ph/0302103.

7. M. N. Achasov, V. M. Aulchenko, K. I. Beloborodov, *et al.*, Phys. Rev. D **65**, 032002 (2002).

8. A. Aloisio *et al.* (KLOE Collaboration), Phys. Lett. B **561**, 55 (2003).

9. N. N. Achasov and A. A. Kozhevnikov, Phys. Rev. D **68**, 074009 (2003).

10. R. R. Akhmetshin *et al.*, Phys. Lett. B **491**, 81 (2000).

11. KLOE Collaboration, hep-ex/0305108.

12. N. N. Achasov and V. A. Karnakov, Pis'ma Zh. Éksp. Teor. Fiz. **39**, 285 (1984) [JETP Lett. **39**, 342 (1984)].

13. N. N. Achasov and A. A. Kozhevnikov, Int. J. Mod. Phys. A **7**, 4825 (1992); Yad. Fiz. **55**, 809 (1992) [Sov. J. Nucl. Phys. **55**, 449 (1992)].

Quasilinear Theory for the Nonlinear Schrödinger Equation with Periodic Coefficients

S. B. Medvedev and M. P. Fedoruk*

Institute of Computational Technologies, Siberian Division, Russian Academy of Sciences,
pr. Akademika Lavrent'eva 6, Novosibirsk, 630090 Russia
* e-mail: mife@ict.nsc.ru

The nonlinear Schrödinger equation with periodic coefficients is analyzed under the condition of large variation in the local dispersion. The solution after n periods is represented as the sum of the solution to the linear part of the nonlinear Schrödinger equation and the nonlinear first-period correction multiplied by the number of periods n. An algorithm for calculating the quasilinear solution with arbitrary initial conditions is proposed. The nonlinear correction to the solution for a sequence of Gaussian pulses is obtained in the explicit form. © 2004 MAIK "Nauka/Interperiodica".

PACS numbers: 42.65.Tg; 42.81.Dp

1. INTRODUCTION

Interest in the study of optical solitons in the framework of the nonlinear Schrödinger equation with periodic coefficients has grown considerably in the last decade in connection with practical advances in using solitons in current fiber-optic communication lines. So-called dispersion-managed solitons are used as information carriers in communication systems (see, e.g., [1]). We note that such a soliton is a stable localized solution rather than a traditional (fundamental) soliton in the theory of completely integrable systems [2]. Periodic variation in the system dispersion makes it possible to increase the soliton amplitude compared to a similar pulse in constant-dispersion systems and, therefore, to increase the signal-to-noise ratio.

Spurious field perturbations, which arise at initially empty places in a sequence of optical pulses as a result of nonlinear four-wave interaction, are among the main causes restricting data transmission over long distances with low error ratios in lines with a rate of 40 Gbit/s and above [3]. There have been several recent attempts to develop a simplified quasilinear theory of this phenomenon [4–8]. To calculate suprious field perturbations and energy in a "test" bit, Ablowitz and Hirooka [5] considered its interaction with nearest neighbors. In [6, 8], the mean amplitude jitter for a random bit sequence was obtained by summing all possible combinations with allowance for the resonance condition. A similar approach was used in [7] to calculate the mean timing jitter due to cross-phase modulation. In that work, the pair interaction of a test pulse with each pulse of the sequence was considered and, then, summation over all possible bit combinations was carried out.

In this work, we obtain a quasilinear equation for calculating the nonlinear correction to an arbitrary initial distribution of the optical field at any point of time interval t rather than at particular points of the test bits, as was done in [4–8]. We propose an effective numerical algorithm for calculating spurious perturbations of the field using the fast Fourier transform. This algorithm provides a considerable time gain, as compared to the direct algorithms of sum calculations considered in [7, 8].

In addition, estimates of the minimum number of neighboring pulses that affect the solution at a given point of the test bit are obtained for a wide range of the fiber-optic line parameters.

In this work, we consider periodic lines with relatively large variation of local dispersion compared to the average dispersion over a period. The case of small variation of local dispersion was considered in [9].

2. QUASILINEAR SOLUTION

The propagation of optical pulses in optical fibers is described by the generalized nonlinear Schrödinger equation

$$i\frac{\partial B}{\partial z} + d(z)\frac{\partial^2 B}{\partial t^2} + \sigma(z)|B|^2 B = iG(z)B, \qquad (1)$$

where B is the complex envelope of the electromagnetic field and the periodic coefficients $d(z)$, $\sigma(z)$, and $G(z)$ describe dispersion, nonlinearity, and gain (loss), respectively. Let the initial conditions for this equation have the form $B(t, 0) = B_0(t)$. Without loss of generality, we assume that all coefficients in Eq. (1) vary with the unit period and $\langle G \rangle = \int_0^1 G(z)dz = 0$. The latter condi-

tion means that the loss and gain are mutually compensated at the period.

To exclude the linear part of the equation, we make the following transformation:

$$B(z, t) = e^{g(z) + i(R(z) + \langle d \rangle z)\Delta} X(z, t), \quad (2)$$

where $g(z) = \int_0^z G(s)ds$ and $R(z) = \int_0^z (d(s) - \langle d \rangle)ds$. The equation for X takes the form

$$X_z = ic(z)e^{-i\rho(z)\Delta}[|e^{i\rho(z)\Delta}X|^2 e^{i\rho(z)\Delta}X], \quad (3)$$

where

$$c(z) = \sigma(z)e^{2g(z)}, \quad \rho(z) = R(z) + \langle d \rangle z,$$

$$\Delta = \frac{\partial^2}{\partial t^2}. \quad (4)$$

We assume that the nonlinearity coefficient is small; i.e., $c(z) \sim \varepsilon \ll 1$. In this case, initial Eq. (1) is quasilinear. The initial conditions for Eq. (3) have the form $X(t, 0) = B_0(t)$. To solve this equation at distances comparable with ε^{-1}, we apply the iteration procedure. The first iteration gives the solution in the form

$$X(t, z) = X^{(1)}(t, z) = B_0(t)$$

$$+ i\int_0^z c(s)e^{-i\rho(s)\Delta}[|e^{i\rho(s)\Delta}B_0(s)|^2 e^{i\rho(s)\Delta}B_0(s)]ds, \quad (5)$$

$$X^{(0)} = B_0(t).$$

For practical applications, it is of interest to find the solution at the points $z_n = n$ after n periods. Unfortunately, the integrand in Eq. (5) is not a periodic function of s, except the case $\langle d \rangle = 0$, and, to find the solution after n periods, it is necessary to integrate from 0 to n. However, we consider the case where the periodic term $R(z)$ of the function $\rho(z)$ is much larger than the linear term $\langle d \rangle z$. In this case, Eq. (5) reduces to the equation

$$X(t, z) = B_0(t)$$

$$+ i\int_0^z c(s)e^{-iR(s)\Delta}[|e^{iR(s)\Delta}B_0(s)|^2 e^{iR(s)\Delta}B_0(s)]ds \quad (6)$$

$$+ O(\langle d \rangle z).$$

Then, the solution after n periods can easily be found in the form

$$X(t, n) = B_0(t) + n\Delta X(t), \quad (7)$$

where the correction to the initial solution at one period is given by the expression

$$\Delta X(t)$$

$$= i\int_0^1 c(s)e^{-iR(s)\Delta}[|e^{iR(s)\Delta}B_0(s)|^2 e^{iR(s)\Delta}B_0(s)]ds. \quad (8)$$

To obtain the solution in the initial variables, it is necessary to make the transformation inverse to transformation (2). It is easy to show that the solution $B(t, n)$ has the form

$$B(t, n) = e^{i\langle d \rangle n\Delta}(B_0(t) + n\Delta X(t)), \quad (9)$$

where the first term represents the linear evolution of the initial solution and the second term is the nonlinear correction to the solution. We emphasize that the function $\Delta X(t)$ describes nonlinear effects. The correction $\Delta X(t)$ can be found numerically for an arbitrary function $B_0(t)$ or analytically for the particular initial conditions $B_0(t)$.

3. ANALYTIC SOLUTION FOR GAUSSIAN PULSES

We take the initial conditions in the form of an infinite sequence of Gaussian pulses

$$B_0(t) = \sum_k e^{-p_k t^2 - q_k t - r_k}, \quad (10)$$

where all coefficients are complex and $\mathrm{Re}\, p_k > 0$. In this case,

$$\Delta X(t) = i\int_0^1 c(s) \sum_{l, m, n} \frac{1}{\sqrt{1 - 4ip_l^* R(s)}} \frac{1}{\sqrt{1 + 4ip_m R(s)}}$$

$$\times \frac{1}{\sqrt{1 + 4ip_n R(s)}} \frac{1}{\sqrt{1 - 4ip_{lmn} R(s)}} \quad (11)$$

$$\times \exp\left\{-\frac{p_{lmn}t^2 + q_{lmn}t + iq_{lmn}^2 R(s)}{1 - 4ip_{lmn}R(s)} - r_{lmn}\right\}ds,$$

where * means complex conjugation and

$$p_{lmn} = \frac{p_l^*}{1 - 4ip_l^* R} + \frac{p_m}{1 + 4ip_m R} + \frac{p_n}{1 + 4ip_n R}, \quad (12)$$

$$q_{lmn} = \frac{q_l^*}{1 - 4ip_l^* R} + \frac{q_m}{1 + 4ip_m R} + \frac{q_n}{1 + 4ip_n R}, \quad (13)$$

$$r_{lmn} = \frac{iq_l^{*2}R}{1 - 4ip_l^* R} - r_l^* - \frac{iq_m^2 R}{1 + 4ip_m R}$$

$$- r_m - \frac{iq_n^2 R}{1 + 4ip_n R} - r_n. \quad (14)$$

The first and second terms in Eq. (9) have the from

$$e^{i\langle d \rangle n\Delta}B_0(t) = e^{i\langle d \rangle n\Delta}\sum_k e^{-p_k t^2 - q_k t - r_k}$$

$$= \sum_k \frac{1}{\sqrt{1 + 4ip_k \langle d \rangle n}} \quad (15)$$

$$\times \exp\left\{-\frac{p_k t^2 + q_k t - i q_k^2 \langle d \rangle n}{1 + 4 i p_k \langle d \rangle n} - r_k\right\},$$

$$ne^{i\langle d\rangle n\Delta}\Delta X(t) = in\int_0^1 c(s) \sum_{l,m,n} \frac{1}{\sqrt{1 - 4ip_l^* R(s)}}$$

$$\times \frac{1}{\sqrt{1 + 4ip_m R(s)}} \frac{1}{\sqrt{1 + 4ip_n R(s)}}$$

$$\times \frac{1}{\sqrt{1 - 4ip_{lmn}R(s)}} \frac{1}{\sqrt{1 + 4i\hat{p}_{lmn}\langle d\rangle n}} \tag{16}$$

$$\times \exp\left\{-\frac{\hat{p}_{lmn}t^2 + \hat{q}_{lmn}t - i\hat{q}_{lmn}^2\langle d\rangle n}{1 + 4i\hat{p}_{lmn}\langle d\rangle n} - \hat{r}_{lmn}\right\}ds,$$

respectively, where

$$\hat{p}_{lmn} = \frac{p_{lmn}}{1 - 4ip_{lmn}R(s)},$$

$$\hat{q}_{lmn} = \frac{q_{lmn}}{1 - 4ip_{lmn}R(s)}, \tag{17}$$

$$\hat{r}_{lmn} = \frac{iq_{lmn}^2 R(s)}{1 - 4ip_{lmn}R(s)} - r_{lmn}.$$

$$c_{lmn} = \frac{p_0 X^2(l^2 + m^2 + n^2 - 8ip_0 R(s)(m^2 + n^2 - mn - ml - nl) + 16p_0^2 R^2(s)(l - m - n)^2)}{(1 + 4ip_0 R(s))(1 - 12ip_0 R(s))}. \tag{21}$$

Not all terms of the triple sum in Eq. (19) are important for calculating the integral. Let us consider the function

$$F_{lmn}(t, s) = \exp\{-a_{lmn}t^2 - b_{lmn}t - c_{lmn}\}.$$

For simplicity, let all amplitudes N_m be identical. To calculate the width of F_{lmn} as a function of the parameter t, it is sufficient to consider $|F_{lmn}|$, which is determined by the real parts of the parameters a_{lmn}, b_{lmn}, and c_{lmn}. We represent $|F_{lmn}|$ in the form

$$|F_{lmn}| = \exp(-S)\exp(-P(t - Q)^2),$$

where

$$P = \frac{3 + 48(p_0 R(s))^2}{1 + (12p_0 R(s))^2}p_0$$

characterizes the width of the function,

$$Q = -(l - m - n)X + \frac{(4l - 2m - 2n)X}{3(1 + 48(p_0 R(s))^2)}$$

gives the position of the maximum, and

The resulting expressions are too complicated for analysis and we will consider a simpler case below.

We assume that all pulses have the same width and they are spaced at the same distance X:

$$B_0(t) = \sum_k N_k e^{-p_0(t - Xk)^2}, \tag{18}$$

where N_k is the complex amplitude. General formula (11) gives

$$\Delta X(t) = i\int_0^1 c(s)$$

$$\times \sum_{l,m,n} \frac{N_l^* N_m N_n}{\sqrt{1 + 4ip_0 R(s)}\sqrt{1 - 12ip_0 R(s)}} \tag{19}$$

$$\times \exp\{-a_{lmn}t^2 - b_{lmn}t - c_{lmn}\}ds,$$

where

$$a_{lmn} = \frac{3 - 4ip_0 R(s)}{1 - 12ip_0 R(s)}p_0,$$

$$b_{lmn} = -\frac{2p_0 X(l + m + n + 4ip_0 R(s)(l - m - n))}{1 - 12ip_0 R(s)}, \tag{20}$$

$$S = \frac{2p_0(l^2 + m^2 + n^2 - lm - ln - mn)X^2}{3(1 + 48(p_0 R(s))^2)}$$

is the amplitude.

To estimate the interaction between pulses, we consider the sum near $t = 0$. In this case, the expression

$$\sum_{l,m,n} |F_{lmn}(0, s)| \tag{22}$$

estimates the nonlinear correction to the solution for a pulse localized at zero.

For two limiting cases $(p_0 R)^2 \longrightarrow 0$ and $(p_0 R)^2 \longrightarrow \infty$, the exponent $PQ^2 + S$ for the function $|F_{lmn}(0, s)|$ has the form

$$PQ^2 + S = p_0 X^2\left(\frac{1}{3}r_1^2 + \frac{1}{2}r_2^2 + \frac{1}{6}r_3^2\right) + O((p_0 R)^2), \tag{23}$$

$$PQ^2 + S = p_0 X^2\left(\left(\frac{1}{3} + \frac{1}{81(p_0 R)^2}\right)r_1^2 \right.$$
$$\left. + \frac{1}{96(p_0 R)^2}r_2^2 + \frac{1}{2592(p_0 R)^2}r_3^2\right) + O((p_0 R)^{-4}), \tag{24}$$

respectively, where $r_1 = l - m - n$, $r_2 = m - n$, and $r_3 = 2l + m + n$.

Two types of initial conditions are possible for each of these limiting cases. If the pulse width is much smaller than the distance between pulses, then $p_0 X^2 \gg 1$, otherwise $p_0 X^2 \ll 1$. We calculate estimates for four possible combinations of the parameter $p_0 R$ and initial conditions.

First, $(p_0 R)^2 \longrightarrow 0$ and $p_0 X^2 \gg 1$. As is seen from Eq. (23), the exponent is zero for $k = l = m = 0$ and much larger than unity for any other combination of l, n, and m. This means that the terms in sum (22) decrease exponentially with an increase in the distance from zero, and, to approximate the sum, it is sufficient to take the term corresponding to the point $(0, 0, 0)$ and several terms with close numbers. In other words, it is sufficient to include several nearest neighbors of the zeroth pulse.

Second, $(p_0 R)^2 \longrightarrow 0$ and $p_0 X^2 \ll 1$. As is seen from Eq. (23), the exponent is zero for $k = l = m = 0$ and increases slowly with moving away from this point, because $p_0 X^2 \ll 1$. In this case, sum (22) can be approximated by the integral

$$\int_{-\infty}^{+\infty} e^{-PQ^2 - S} \, dl \, dm \, dn. \tag{25}$$

Obviously, the width of the integrand is equal to $1/\sqrt{p_0 X^2} \gg 1$. The number of points for the satisfactory finite-difference approximation of integral (25) is proportional to the width. Thus, to calculate the initial sum, it is necessary to take into account pulses with numbers up to $1/\sqrt{p_0 X^2}$.

Third, $(p_0 R)^2 \longrightarrow \infty$ and $p_0 X^2 \ll 1$. In this case, coefficients of r_1, r_2, and r_3 are sufficiently small. Therefore, similar to the preceding case, integral (25) can be considered as an approximation to the corresponding sum given by Eq. (22). To satisfactorily approximate integral (25), it is necessary to take certain numbers of discrete points in the r_1, r_2, and r_3 directions. These numbers are on the order of $1/\sqrt{p_0 X^2}$, $\sqrt{96} p_0 R/\sqrt{p_0 X^2}$, and $\sqrt{2592} p_0 R/\sqrt{p_0 X^2}$ for the r_1, r_2, and r_3 direction, respectively. This means that pulses with numbers no smaller than $1/\sqrt{p_0 X^2}$ must be involved in summation.

Finally, let us consider the fourth variant $(p_0 R)^2 \longrightarrow \infty$ and $p_0 X^2 \gg 1$. It is seen from Eq. (6) that, in contrast to the preceding cases, the coefficients of coordinates r_2 and r_3 depend on the quantity $p_0 X^2 (p_0 R)^{-2}$ and the coefficient of r_1 depends only on $p_0 X^2$. Therefore, to approximate the exponent in sum (22) in the r_1 direction, it is sufficient to include terms for which the coordinate r_1 is close to zero. For the approximation of the exponent in Eq. (22) in the r_2 and r_3 directions, two variants are possible. To satisfactorily approximate sum (22) in the case of $p_0 X^2 (p_0 R)^{-2} \gg 1$, it is sufficient to take into account pulses near the zeroth pulses in the r_2 and r_3 coordinates. Otherwise, it is necessary to include $\sqrt{96} p_0 R/\sqrt{p_0 X^2}$ and $\sqrt{2592} p_0 R/\sqrt{p_0 X^2}$ points for the r_2 and r_3 coordinates, respectively.

The above results were confirmed by the direct calculations of various sums.

In closing this section, we note that the estimates were obtained for equal amplitudes of the initial pulses. The case of different amplitudes is more complex. However, the above estimates give an indication of the minimum number of neighboring pulses that can affect the solution at zero.

4. RESULTS OF NUMERICAL INTEGRATION

First, let us discuss algorithms for the numerical integration of Eqs. (1) and (6).

Nonlinear Schrödinger equation (1) was numerically solved by the symmetric method of splitting into physical processes [1]:

$$B(z + \Delta z, t)$$
$$= \exp\left(\frac{\Delta z}{2} \tilde{N}\right) \exp(\Delta z \hat{D}) \exp\left(\frac{\Delta z}{2} \hat{N}\right) B(z, t). \tag{26}$$

Here, $\hat{D}$ is the operator allowing for the dispersion and loss in a linear medium and $\hat{N}$ is the nonlinear operator allowing for the nonlinearity effect on pulse propagation. The exponential operator $\exp(\Delta z \hat{D})$ can be estimated in the spectral region by the formula

$$\exp(\Delta z \hat{D}) B(z, t) = F_T^{-1} \exp(\Delta z \hat{D}(i\omega)) F_T B(z, t),$$

where F_T is the Fourier transform operator.

The function

$$Y(t, s) = e^{-iR(s)\Delta} \left[\left| e^{iR(s)\Delta} B_0(s) \right|^2 e^{iR(s)\Delta} B_0(s) \right]$$

entering Eq. (6) is calculated by using the fast Fourier transform. In particular,

$$e^{iR(s)\Delta} B_0(s) = F_T^{-1} (e^{-iR(s)\omega^2} F_T B_0(s)).$$

After calculation of $Y(t, s)$, $X(t, z)$ is obtained by single integration with respect to z in Eq. (6).

As an example, we consider the symmetric dispersion map TF + CF + TF with a general loss of 20 dB. For complete compensation of loss in this line, the inverse Raman pumping was used. The transmission fiber (TF) had a dispersion of 20 ps/nm/km at 1550 nm; effective area $A_{\text{eff}} = 106$ μm^2; losses of 0.188 and 0.234 dB/km at 1550 and 1450 nm, respectively; and

Fig. 1.
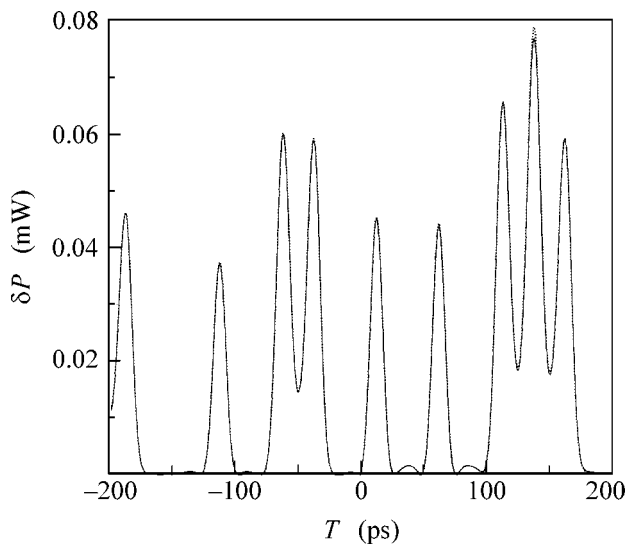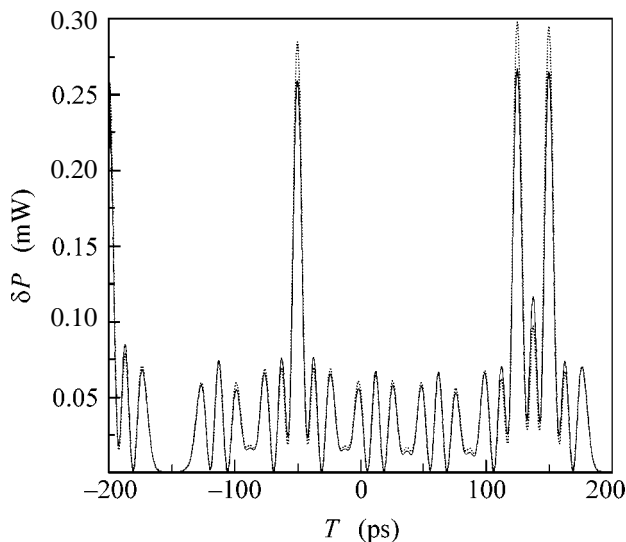

Fig. 2.

the nonlinear index of refraction $n_2 = 2.7 \times 10^{-20}$ V^{-1}/m^2. The compensating fiber (CF) had a dispersion of -42.3 ps/nm/km at 1550 nm; effective area $A_{\text{eff}} = 30$ μm^2; losses of 0.233 and 0.304 dB/km at 1550 and 1450 nm, respectively; and the nonlinear index of refraction $n_2 = 2.7 \times 10^{-20}$ V^{-1}/m^2.

Figures 1 and 2 show the correction δP to the initial signal power as a function of time after ten periodic sections of the communication line for the average dispersions $\langle D \rangle = 0$ and 0.05 ps/nm/km, respectively. In the calculations, a pseudorandom sequence consisting of 128 bits with a general duration of 3200 ps (data transmission rate 40 Gbit/s) was simulated. A single Gaussian pulse in the sequence had a width of 12.5 ps and a

peak power of 1 mW. As is seen in these figures, the quasilinear approximation adequately reproduces signal evolution and can be used to numerically simulate periodic fiber-optic transmission lines.

5. CONCLUSIONS

The solution to Eq. (1) has been represented as an explicit function of the initial data. The equation corresponding to this transformation has the form

$$X_z = ic(z)e^{-iR(z)\Delta}[|e^{iR(z)\Delta}X|^2 e^{iR(z)\Delta}X]. \qquad (27)$$

This equation differs from the equation obtained by averaging in [10, 11]. Equation (27) and transformation (7) are valid if $R(z) \gg \langle d \rangle z$. The advantage of this transformation is that nonlinear effects per period are described by a single function $\Delta X(t)$. A numerical algorithm based on this simple transformation has been proposed and realized. This algorithm can also be used to find periodic solutions to the averaged equation [12].

An analytic solution for an infinite sequence of Gaussian pulses has been obtained in this approximation. Analytic estimates show that the inclusion of only nearest neighbors in calculation of the nonlinear interaction of a test pulse with other pulses of the bit sequence is insufficient if the local dispersion varies strongly.

REFERENCES

1. G. P. Agrawal, *Nonlinear Fiber Optics*, 3rd ed. (Academic, Boston, 2001; Mir, Moscow, 1996).
2. V. E. Zakharov, S. V. Manakov, S. P. Novikov, and L. P. Pitaevskiĭ, *The Theory of Solitons. The Inverse Scattering Method* (Nauka, Moscow, 1980; Consultants Bureau, New York, 1984).
3. P. V. Mamyshev and N. A. Mamysheva, Opt. Lett. **24**, 1454 (1999).
4. F. Merlaud and S. K. Turitsyn, in *Proceedings of ECOC2000* (Munchen, Germany, 2000), Vol. 3, p. 35.
5. M. J. Ablowitz and T. Hirooka, Opt. Lett. **25**, 1750 (2000).
6. M. J. Ablowitz and T. Hirooka, Opt. Lett. **26**, 1846 (2001).
7. M. J. Ablowitz and T. Hirooka, Opt. Lett. **27**, 203 (2002).
8. S. Kumar, J. C. Mauro, S. Raghavan, and D. Q. Chowdhury, IEEE J. Sel. Top. Quantum Electron. **8**, 3 (2002).
9. S. B. Medvedev and S. K. Turitsyn, JETP Lett. **69**, 499 (1999).
10. I. Gabitov and S. K. Turitsyn, Opt. Lett. **21**, 327 (1996).
11. S. K. Turitsyn, V. K. Mezentsev, and E. G. Turitsyna, in *Technical Digest of Quantum Electronics and Photonics Conference* (Inst. of Physics, Manchester, 1999), p. 217.
12. S. B. Medvedev, O. V. Shtyrina, S. L. Musher, and M. P. Fedoruk, Phys. Rev. E **66**, 066607 (2002).

Translated by R. Tyapaev

Ionization Mechanisms of Aluminum Acceptor Impurity in Silicon

T. N. Mamedov[1],*, D. G. Andrianov[2], D. Herlach[3], V. N. Gorelkin[4], A. V. Stoikov[1], and U. Zimmermann[3]

[1] *Joint Institute for Nuclear Research, Dubna, Moscow region, 141980 Russia*
*e-mail: tmamedov@nu.jinr.ru
[2] *State Research and Project Institute of Rare-Metal Industry "Giredmet," Moscow, 109017 Russia*
[3] *Paul Scherrer Institut, CH-5232 Villigen PSI, Switzerland*
[4] *Moscow Institute of Physics and Technology, Institutskiǐ per. 9, Dolgoprudnyǐ, Moscow region, 141700 Russia*
Received November 12, 2003

Processes of ionization of shallow acceptor centers (ACs) in silicon are studied. In crystalline silicon samples with phosphorus (1.6×10^{13}, 2.7×10^{13}, and 2.3×10^{15} cm^{-3}) and boron (1.3×10^{15} cm^{-3}) impurities, $_\mu$Al impurity atoms were produced by implantation of negative muons. It is found that thermal ionization is the main mechanism for ionizing the Al acceptor impurity in both *p*-type and *n*-type silicon with an impurity concentration of $\lesssim 10^{15}$ cm^{-3} at $T > 45$ K. The thermal ionization rate of Al ACs in Si varies from $\sim 10^5$ to $\sim 10^6$ s^{-1} in the temperature range 45–55 K. © *2004 MAIK "Nauka/Interperiodica"*.

PACS numbers: 71.55.Cn; 61.72.Tt; 76.75.+i; 36.10.Dr

It was shown in our previous publications [1, 2] that the use of polarized negative muons provides rich information on the interaction of acceptor centers (ACs) in silicon. The implantation of μ^- into Si leads to the formation of a muonic atom $_\mu$Al which models an acceptor impurity of aluminum. Information on the charge state of the electronic shell in the given muonic atom (AC) and on its interaction with the medium is contained in the polarization function $P(t)$ of the muon located at the $1s$ level of the $_\mu$Al atom.

In a magnetic field transverse to the muon spin, the behavior of the muon polarization is described by the system of differential equations [3]

$$\frac{d}{dt}P_p = (i\omega_p - \lambda_p - \nu_i)P_p + \nu_c P_d,$$
$$\frac{d}{dt}P_d = \nu_i P_p + (i\omega_d - \nu_c)P_d, \quad (1)$$

where subscripts p and d denote the paramagnetic (neutral) and diamagnetic (ionized) states of the AC, respectively ($_\mu$Al^0 and $_\mu$Al$^-$); P_p and P_d are complex quantities (the experimentally observable quantity is $P = \mathrm{Re}(P_p + P_d)$; ν_i is the AC ionization rate; ν_c is the rate of hole capture by $_\mu$Al$^-$; ω_p and ω_d are the muon spin precession frequencies; and λ_p is the muon spin relaxation rate in the paramagnetic state. In the approximation of isotropic hyperfine interaction between the magnetic moments of the muon and AC electronic shell, the para-

magnetic shift of precession frequency and the muon spin relaxation rate are [4],

$$\frac{\omega_p - \omega_d}{\omega_d} = -\frac{g\mu_B}{2\mu_B^\mu}\frac{J(J+1)A}{3k_B T}, \quad (2)$$

$$\lambda_p = \frac{J(J+1)}{3}\left(\frac{(A/\hbar)^2}{\nu} + \frac{(A/\hbar)^2\nu}{\nu^2 + \omega_e^2}\right), \quad (3)$$

where A is the hyperfine interaction constant, ν is the relaxation rate of AC magnetic moment; $\hbar = h/2\pi$; h is the Planck's constant; k_B is the Boltzmann constant; μ_B and μ_B^μ are the electron and muon Bohr magneton, respectively; g is the AC g factor; $\omega_e = g\mu_B B/\hbar$ is the angular precession frequency of the magnetic moment of AC electronic shell in magnetic field B; and T is temperature. For a shallow AC in silicon, we have $J = 3/2$ [5] and $g = -1.07$ [6].

Under the conditions that only one of the AC charge states is populated at the initial instant and there are no transitions between states ($\nu_i = \nu_c = 0$), the solution to system (1) has the form

$$P(t) = P_0 e^{-\lambda t}\cos(\omega t + \phi), \quad (4)$$

where P_0 is the muon polarization at the $1s$ level at $t = 0$, $\lambda = \lambda_p(0)$, $\omega = \omega_p(\omega_d)$ in the AC paramagnetic (diamagnetic) state, and ϕ is the initial phase of the muon spin precession.
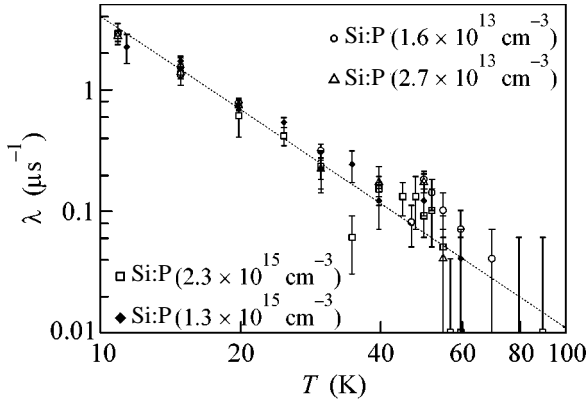
Fig. 1. Temperature dependences of the muon spin relaxation rate. The dotted line is drawn for better visualization.
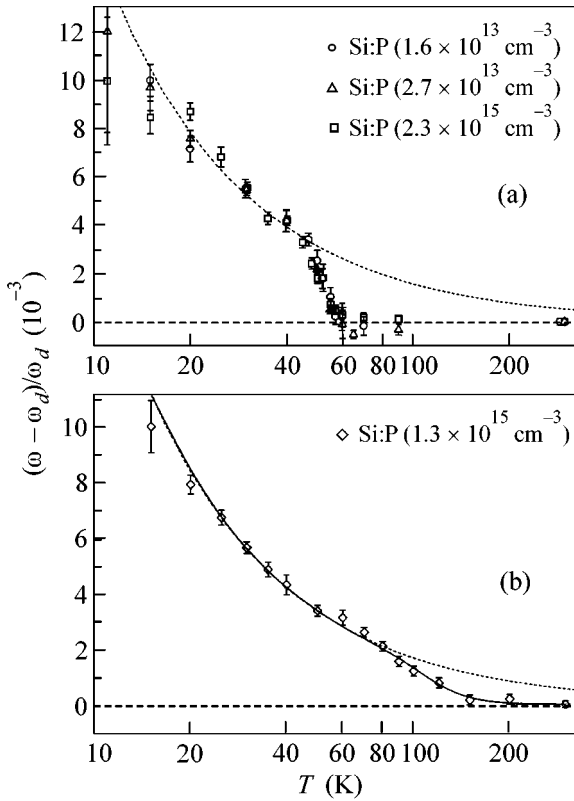
Fig. 2. Temperature dependences of the frequency shift in the muon spin precession for silicon samples with (a) phosphorus and (b) boron impurity. Dotted curves correspond to dependence (2) with $A/h = 23.6$ (a) and 25.3 MHz (b). The solid curve in Fig. 2b is the result of approximation of the experimental data by dependence (7) with $A/h = 25.3$ MHz and $E_i = 66.0$ meV.

Our earlier studies [1, 2] show that the function of type (4) describes experimental data for the samples of nondegenerate *n*- and *p*-type silicon at $T \lesssim 50$ K. The occurrence of muon spin relaxation and the form of the

temperature dependence of ω indicate that an AC is initially formed in the paramagnetic state and its ionization probability in time $\sim \tau_\mu$ ($\tau_\mu = 760$ ns is the lifetime of μ^- at the $_\mu$Al $1s$ level [7]) is negligibly small.

However, analysis of a silicon sample containing a phosphorus impurity with a concentration of 1.6×10^{13} cm^{-3} [8] revealed that the $\Delta\omega/\omega_d = f(T)$ dependence ($\Delta\omega = \omega - \omega_d$, where ω is the precession frequency at temperature T) is described by $1/T$ from (2) only at $T \lesssim 50$ K, while the muon spin precession frequency corresponds to the diamagnetic state of an AC even at $T > 52$ K. It was concluded that the AC ionization probability in this sample becomes significant at $T > 50$ K in a time period on the order of τ_μ. However, the available data on the rate of processes such as electron capture from the conduction band by an AC and acceptor thermal ionization are not sufficient for determining the AC ionization mechanism. The scatter in the experimental data on the coefficient of electron capture by a neutral AC in silicon reaches five orders of magnitude [9]. The thermal ionization rate of a boron impurity in silicon was determined, for example, in [10] and amounts to $\approx 2 \times 10^4$ s^{-1} at $T = 21$ K. However, the temperature dependence of the ionization rate (in the temperature range 11–21 K) corresponded to a boron ionization energy of 8.3 meV, which is considerably lower than the calculated value of this quantity (45 meV [11]). Note that the knowledge of the ionization rate for shallow impurity centers is highly important for estimating the response speed of semiconducting devices operating at low temperatures [10, 12].

This study aims at determining the ionization mechanism for a $_\mu$Al AC in Si and determining the ionization rate of this center. For this purpose, we analyzed the behavior of the polarization of negative muons in silicon samples with phosphorus (1.6×10^{13}, 2.7×10^{13}, and 2.3×10^{15} cm^{-3}) and boron (1.3×10^{15} cm^{-3}) impurities in the temperature range 10–300 K.

Measurements were made on the GPD spectrometer [13] mounted in the muon channel μE1 of the proton accelerator at the Paul Scherrer Institute (PSI, Switzerland). The samples were cut from silicon single crystals, had the shape of disks (with a diameter of ~30 mm and a height of ~12 mm), and were mounted so that the disk axis coincided with the axis of the muon beam. A magnetic field was produced by Helmholtz coils. The field magnitude was 2.5 kG with a long-term stability no worse than 10^{-4}. The temperature of the samples was maintained to within 0.1 K.

The muon polarization was measured by detecting decay electrons from the reaction $\mu^- \longrightarrow e^- + \bar{\nu}_e + \nu_\mu$. The time dependence of the number of detected electrons has the shape of an exponential modulated by function $P(t)$. The measurement technique and the procedure for reconstructing the parameters of the muon spin polarization from the recorded μ^-SR spectra are described in detail in [1, 3].

Figures 1 and 2 show the temperature dependences of the relaxation rate λ and frequency shift $\Delta\omega/\omega_d$ of muon spin precession (for ω_d, we took the room-temperature precession frequency equal to 212.22 ± 0.05 rad/μs), which were obtained by the approximation of experimental data using polarization function (4).

It can be seen from Fig. 1 that the muon spin relaxation rate for all samples increases with decreasing temperature approximately in proportion to T^{-q} ($q \sim 3$). Such a behavior of λ agrees with our earlier results obtained for nondegenerate samples and is associated with the spin–lattice relaxation of the AC magnetic moment (see [1, 2]).

The behavior of the muon spin precession frequency shift in the n-type silicon with a phosphorus impurity (Fig. 2a) at $T \lesssim 45$ K is described by $1/T$ dependence (2) with the hyperfine interaction constant $A/h = 23.6 \pm 0.4$ MHz. At $T > 45$ K, $\Delta\omega/\omega_d$ deviates from dependence (2); for $T > 55$ K, we have $\omega \approx \omega_d$. Thus, the predominant population of the AC paramagnetic (nonionized) state gives way to the predominant population of the diamagnetic (ionized) state in the temperature range 45–55 K. Evidently, this transition is associated with an increase in the AC ionization rate ν_i with increasing temperature. The rate ν_c of the reverse process (hole capture by $_\mu$Al$^-$) in n-type silicon is negligibly small. Indeed, from the detailed balancing principle, we have $\nu_c/\nu_i = W_0/W_-$, where W_0 ($W_- = 1 - W_0$) is the probability of finding a $_\mu$Al AC in the neutral (ionized) state ($W_0 = 0$ in n-type silicon; see [8]). The solution to Eq. (1) for $\nu_i \neq 0$, $\nu_c = 0$, and $\lambda \ll \delta = \omega_p - \omega_d$ ($\lambda \lesssim 10^5$ s^{-1} and $\delta \approx 3 \times 10^{-3}\omega_d \approx 6 \times 10^5$ s^{-1} for $45 \leq T \leq 55$ K; see Figs. 1 and 2a) is the polarization function [3]

$$P(t) = P_0 \left[\frac{\delta}{\sqrt{\delta^2 + \nu_i^2}} e^{-\nu_i t} \cos((\omega_d + \delta)t + \phi - \pi/2) \right.$$

$$\left. + \frac{\nu_i}{\sqrt{\delta^2 + \nu_i^2}} \cos(\omega_d t + \phi) \right]. \tag{5}$$

Function (5) was used for fitting the experimental data for n-type silicon at temperatures 45–55 K. At each temperature from this range, the value of δ was calculated using formula (2) (for $A/h = 23.6$ MHz and $\omega_d = 212.22$ rad/μs). Subsequently, in processing the experimental data, the values of parameters ω_d and δ were fixed.

The values of the AC ionization rate obtained by the approximation of the experimental data are shown in Fig. 3. It can be seen that the ionization rate at $T = 55$ K is approximately the same for all three samples and amounts to $\approx 10^6$ s^{-1}. It is worth noting that the electron concentration in the conduction band of silicon at $T = 55$ K increases by more than an order of magnitude upon a change in the phosphorus concentration from
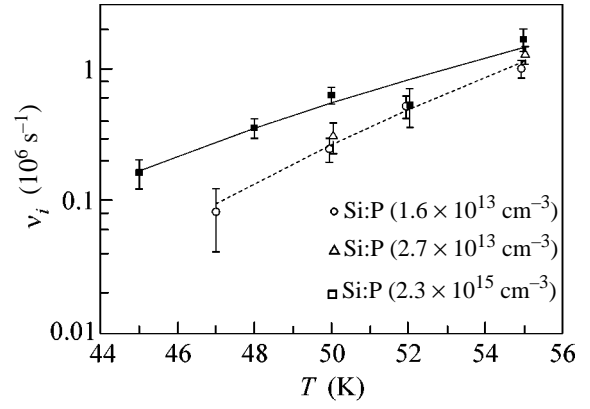
Fig. 3. Temperature dependences of the ionization rate for a $_\mu$Al AC in Si, obtained as a result of processing experimental data for Si samples with P impurity by using polarization function (5). The solid and dotted curves describe dependences of the form $\nu_i \sim T^{-1}\exp(-E_i/k_B T)$ for $E_i = 50$ and 74 meV, respectively.

1.6×10^{13} cm^{-3} to 2.3×10^{15} cm^{-3} (see [8]). This means that the AC ionization at this temperature is determined by the electron capture not from the conduction band but from the valence band. In other words, the $_\mu$Al$^-$-bound h^+ hole undergoes transition to the valence band; the energy necessary for this transition is acquired due to the interaction with phonons.

The rate of hole thermal emission from neutral acceptors is defined by the well-known expression [9]

$$\nu_i = N_v \sigma_p^- v_{th} \exp(-E_i/k_B T), \tag{6}$$

where $N_v = 2(m^* k_B T/2\pi\hbar^2)^{3/2}$ is the effective density of states in the valence band; m^* and $v_{th} = \sqrt{3k_B T/m^*}$ are the effective mass and thermal velocity of holes; σ_p^- is the cross section for hole capture by a negatively charged AC; and E_i is the AC ionization energy.

Using relation (6), we can estimate the thermal ionization rate of the Al acceptor impurity in Si. Using the calculated values [14] for the capture cross section, σ_p^- [cm^2] $\approx 3.8 \times 10^{-8}T^{-3}$ for $2.8 \leq T < 100$ K, for E_i (Al) $= 68$ meV [11], we obtain ν_i(Al) $\sim 10^6$ s^{-1} at $T = 55$ K. Thus, the ionization rate for $_\mu$Al AC determined here is on the same order of magnitude as the theoretical estimate of the thermal ionization rate for an Al acceptor center in Si.

The value of ionization energy E_i of a $_\mu$Al acceptor obtained by fitting the function $\nu_i \sim T^{-1}\exp(-E_i/k_B T)$ to the data represented in Fig. 3, amounted to 74 ± 8 meV and 50 ± 7 meV for samples with phosphorus concentrations of $\sim 10^{13}$ cm^{-3} and 2.3×10^{15} cm^{-3}, respectively. The slightly smaller slope of the $\nu_i(T)$ dependence for the sample with a higher phosphorus impurity concentration (see Fig. 3) is probably due to an additional con-

tribution to the acceptor ionization rate due to the electron capture from the conduction band. Note that the values obtained for ν_i and E_i may contain a systematic error (~30 and ~5% in determining ν_i and E_i, respectively) due to the fact that parameters ω_d and δ were fixed in data processing.

In silicon with a boron atom impurity of 1.3×10^{15} cm^{-3} (see Fig. 2b), the deviation of the frequency shift in the muon spin precession from the Curie law is observed at a higher temperature ($T > 80$ K) than in samples with a phosphorus impurity. In contrast to the *n*-type silicon, the probability of the reverse process (hole capture from the valence band by $_\mu$Al$^-$) in *p*-type silicon is as high as the probability of acceptor thermal ionization (the rate of this process for nondegenerate silicon samples is independent of the impurity type). For the given boron concentration in the sample, the capture rate $\nu_c = \nu_i W_0/(1 - W_0)$ is considerably higher than the ionization rate ν_i at $T \lesssim 80$ K ($W_0 \approx 1$ [8]). At $T > 45$ K, when the ionization probability of $_\mu$Al^0 in a time period on the order of τ_μ becomes significant, the condition $\lambda, \delta \ll (\nu_i + \nu_c)$ also holds. The solution to the system of differential equations (1) in this case leads to a polarization function of the form (4) with $\lambda = W_0\lambda_p$ and $\omega = W_0\omega_p + W_-\omega_d$. Accordingly, for the frequency shift in the muon spin precession, we obtain

$$\frac{\Delta\omega}{\omega_d} = \frac{\omega_p - \omega_d}{\omega_d}W_0. \tag{7}$$

The population W_0 of state $_\mu$Al^0 was calculated as in [15], to give

$$W_0 = \left[1 + \beta^{-1}\exp\left(\frac{F - E_i}{k_\mathrm{B}T}\right)\right]^{-1}, \tag{8}$$

where E_i is the ionization energy of a $_\mu$Al acceptor center, β is the degeneracy factor ($\beta = 4$), and F is the Fermi energy (analytic expressions for determining the position of the Fermi level are given, for example, in [15]).

Function (7) was used for approximating the experimental data represented in Fig. 2b. The values of the hyperfine interaction constant and the AC ionization energy obtained as a result of this approximation were 25.3 ± 0.4 MHz and 66.0 ± 3.4 meV, respectively.

Thus, the results obtained in this study demonstrate that thermal ionization is the main ionization mechanism for an Al acceptor impurity in both *p*-type and *n*-type silicon with a donor impurity concentration of $\lesssim 10^{15}$ cm^{-3} at $T > 45$ K. The thermal ionization rate for an Al AC in Si in the temperature range 45–55 K varies from ~10^5 to ~10^6 s^{-1}.

REFERENCES

1. T. N. Mamedov, A. V. Stoĭkov, and V. N. Gorelkin, Fiz. Élem. Chastits At. Yadra **33**, 1005 (2002) [Phys. Part. Nucl. **33**, 519 (2002)].

2. T. N. Mamedov, D. Herlach, V. N. Gorelkin, *et al.*, Physica B (Amsterdam) **326**, 97 (2003).

3. T. N. Mamedov, I. L. Chaplygin, V. N. Duginov, *et al.*, J. Phys.: Condens. Matter **11**, 2849 (1999).

4. V. N. Gorelkin, T. N. Mamedov, and A. S. Baturin, Physica B (Amsterdam) **289–290**, 585 (2000).

5. G. L. Bir and G. E. Pikus, *Symmetry and Strain-Induced Effects in Semiconductors* (Nauka, Moscow, 1972; Wiley, New York, 1975).

6. H. Neubrand, Phys. Status Solidi B **86**, 269 (1978).

7. T. Susuki, D. F. Measday, and J. P. Roalsvig, Phys. Rev. C **35**, 2212 (1987).

8. T. N. Mamedov, D. G. Andrianov, D. Herlach, *et al.*, Pis'ma Zh. Éksp. Teor. Fiz. **76**, 515 (2002) [JETP Lett. **76**, 440 (2002)].

9. A. G. Milnes, *Deep Impurities in Semiconductors* (Wiley, New York, 1973; Mir, Moscow, 1977).

10. S. K. Tewksbury, J. Appl. Phys. **53**, 3865 (1982).

11. *Physical Quantities. Handbook*, Ed. by I. S. Grigor'ev and E. Z. Meĭlikhov (Énergoatomizdat, Moscow, 1991).

12. E. Rosencher, V. Mosser, and G. Vincent, Phys. Rev. B **29**, 1135 (1984).

13. R. Abela, C. Baines, X. Donath, *et al.*, Hyperfine Interact. **87**, 1105 (1994).

14. V. N. Abakumov, V. I. Perel', and I. N. Yassievich, Fiz. Tekh. Poluprovodn. (Leningrad) **12**, 3 (1978) [Sov. Phys. Semicond. **12**, 1 (1978)].

15. K. V. Shalimova, *Physics of Semiconductors* (Énergiya, Moscow, 1971).

Translated by N. Wadhwa

JETP Letters, Vol. 79, No. 1, 2004, pp. 25–27. Translated from Pis'ma v Zhurnal Éksperimental'noĭ i Teoreticheskoĭ Fiziki, Vol. 79, No. 1, 2004, pp. 30–33.
Original Russian Text Copyright © 2004 by Karlykhanov, Lykov, Timakova, Chizhkov.

1D-Simulation Results of Indirect-Driven Target Optimization for Ignition at Iskra-6 Facility

N. G. Karlykhanov, V. A. Lykov, M. S. Timakova, and M. N. Chizhkov*

Zababakhin All-Russia Research Institute of Technical Physics, Snezhinsk, Chelyabinsk region, 456770 Russia

*e-mail: m.n.chizhkov@vniitf.ru

Received November 17, 2003

A design of an indirect-drive ignition target for the Iskra-6 laser facility is proposed. One-dimensional simulations show that the 1.7-MJ fusion yield can be achieved at an energy absorbed by the target of about 30 kJ. © 2004 MAIK "Nauka/Interperiodica".

PACS numbers: 52.57.Bc

At present, the NIF and LMJ high-power laser facilities with the pulse energy as high as 2 MJ [1, 2] are being created in the USA and France. In [1–3], it was shown that the ignition of cryogenic thermonuclear targets can be achieved in these facilities. The implosion of spherical indirect-drive targets will be provided by blackbody X radiation with a temperature of up to 350 eV, which is generated when the laser radiation is focused into a cylindrical gold cavity. In Russia, the Iskra-6 laser facility on the basis of a solid-state laser with a pulse energy of up to 300 kJ and a nanosecond pulse duration is planned to be created at the Russian Federal Nuclear Center All-Russia Research Institute of Experimental Physics (RFNC VNIIEF) [4].

The Hohlraum-type pellet proposed at the RFNC VNIITF consists of a spherical gold shell with eight holes through which laser radiation is introduced, eight screens, and a multilayer spherical target at the center [5]. Three-dimensional calculations of the radiation propagation inside the Hohlraum, as well as 1D simulations of the implosion and burning of the multilayer spherical target, were performed. These calculations and estimates indicate that the conditions necessary for a thermonuclear burst with a neutron yield of 10^{16} per pulse at a laser energy lower than 1 MJ [5] can be achieved with this target.

The present study continues the investigations on inertial confinement fusion (ICF) carried out at the RFNC VNIITF. The aim of this work is to study the possibility of igniting a thermonuclear target with a beryllium ablator (which is similar to the NIF target [6]) in the Iskra-6 facility. The NIF target, which was proposed at the Los Alamos National Laboratory (LANL), consists of a copper-doped (with a Cu atomic fraction of 0.9%) beryllium ablator in the shape of a 0.155-mm-thick spherical shell, whose inner surface is covered with a 0.08-mm-thick DT-ice layer with an inner radius of 0.87 mm. The central region of the target is filled with a DT gas with an equilibrium density of 0.3 mg/cm³. In [7], the time dependence of the blackbody radiation temperature required for ignition is presented; the peak value of the radiation temperature is 330 eV. In 1D simulations of the LANL target by the LASNEX code, the fusion energy yield was 18.1 MJ at a thermal radiation energy absorbed by the target of 214 kJ [7].

The target parameters were chosen using the ERA 1D code [8, 9], which was developed for simulating physical processes occurring in ICF targets. The energy and momentum transport by nonequilibrium radiation was taken into account in the multigroup diffusion approximation. In simulations, we used the tabulated spectral absorption coefficient calculated by the mean atom model [10].

As a starting point for the target optimization, we used the LANL target, which was decreased twofold. The time dependence of the blackbody radiation temperature on the target surface was scaled by reducing the time scale by half.

The energy absorbed by the target is described by the following approximate relationship:

$$E_{abs} = \sigma T^4 \times 4\pi R^2 \Delta t,$$

where T is the peak radiation temperature, R is the outer radius of the target, and Δt is the temperature rise time. The twofold decrease in the radius R and time Δt should lead to a decrease in the absorbed energy by a factor of 8: from 214 kJ for the LANL target to 25–30 kJ for the scaled target.

The LANL target scaling does not provide exact self-similarity. It was shown in [3] that the NIF target starts to be ignited from a hot central spot with the temperature $T_i \sim 10$ keV and $\rho R \sim 0.3$ g/cm². In the scaled
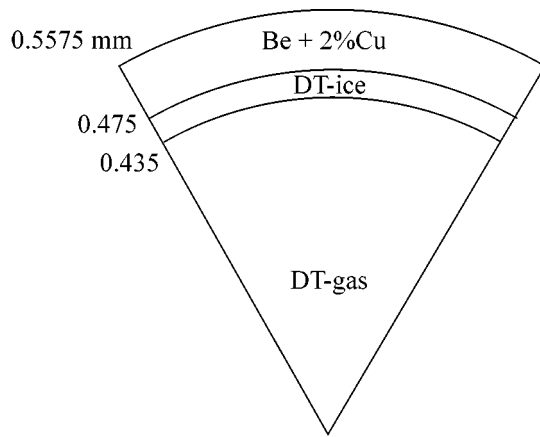
Fig. 1. Schematic of a thermonuclear target for the Iskra-6 facility.
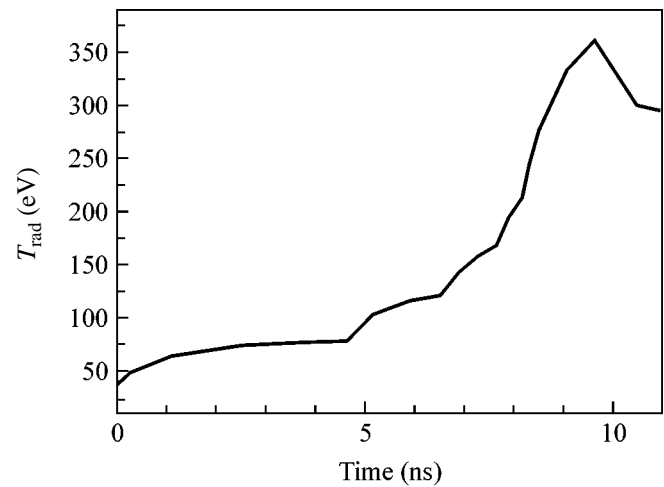
Fig. 2. Time dependence of the blackbody radiation temperature on the target surface.

target, the required value of ρR in the hot spot is not reached and the target is not ignited.

According to [3], the driver energy required for ignition is inversely proportional to a certain power of the implosion velocity: $E_{las} \sim 1/V_{imp}^{\alpha}$, $\alpha = 5\text{--}10$. Conse-

Table

	NIF	Iskra-6
Target parameters		
Outer shell radius, mm	1.105	0.5575
Beryllium shell thickness, μm	155	82.5
DT-ice thickness, μm	80	40
Cu atomic fraction in the ablator, %	0.9	2
Hohlraum temperature		
Maximum radiation temperature, eV	330	360
Temperature rise time, ns	20	10
Calculation of the target implosion		
Energy absorbed by the target, kJ	200	31
Velocity of the imploding shell, km/s	330	400
Mass fraction of the evaporated material, %	84	90
Calculation of the target burning		
Maximum ion temperature, keV	100	40
Maximum fuel density, g/cm^3	490	700
Tritium burning-out, %	34	19
Fusion energy yield, MJ	24	1.7
Neutron yield, 10^{17}	90	6
Required laser parameters		
Energy, MJ	1.4	0.3

quently, the velocity of the imploding shell should be increased as the laser energy decreases. The implosion velocity is nearly proportional to the radiation temperature on the target surface: $V_{imp} \sim T^{0.9}$ [3]. Hence, for the decreased target to be ignited, the temperature should be increased.

The self-similarity in terms of the radiation mean-free-path lengths is also absent. In the scaled target, the mean-free-path lengths should be shorter, which may be achieved by increasing the copper content in beryllium.

The target optimization by the ERA code allowed us to self-consistently determine the target parameters (Fig. 1), the radiation temperature (Fig. 2), and the optimum Cu fraction in the ablator. The thickness of the beryllium shell was increased by 6% with respect to the halved LANL target. The peak radiation temperature on the target surface was 360 eV. When using an ablator consisting of 98% beryllium atoms and 2% copper atoms, the calculated energy yield was about 1.7 MJ.
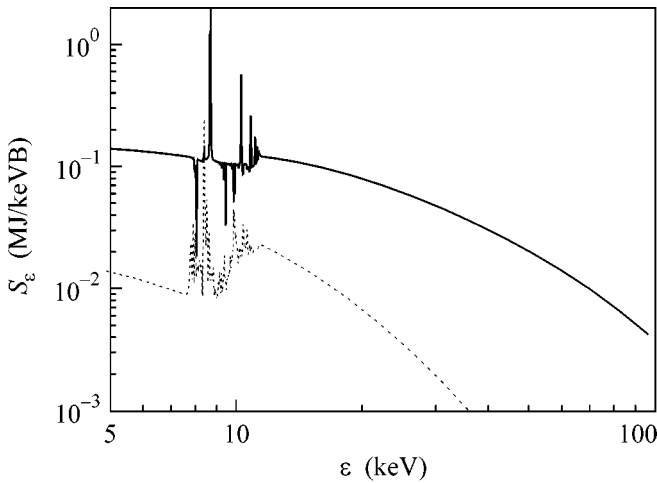
The table presents the parameters of the implosion and burning of thermonuclear targets calculated for the NIF and Iskra-6 facilities by the ERA code. The fusion energy yield calculated for the LANL target by the ERA code coincides with that calculated by the LASNEX code accurate to 30%. This confirms the reliability of the methods used at the RFNC VNIITF and LANL to calculate thermonuclear targets.

The energy absorbed by the scaled target was 31 kJ. For a Hohlraum of the NIF type [3] (with a laser–target energy conversion efficiency of $\eta = E_{abs}/E_{las} = 0.12\text{--}0.15$), the ignition can be achieved at a laser energy of 200–300 kJ, which is on the order of the laser pulse energy in the Iskra-6 facility.

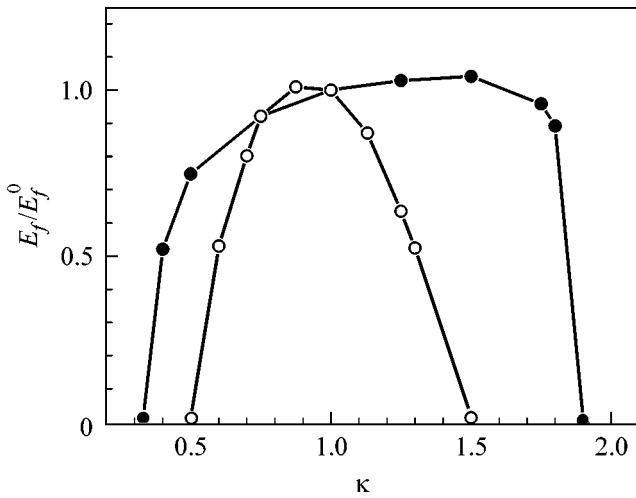The maximum fuel density achieved in the course of implosion of the optimized target is 1.4 times higher

Fig. 3. Spectrum of radiation with a photon energy higher than 5 keV for the NIF (solid curve) and Iskra-6 (dashed curve) targets.

Fig. 4. The calculated fusion energy yield as a function of the radiation absorption coefficient (normalized to the fusion energy yield at a rated absorption coefficient) for the NIF (closed circles) and Iskra-6 (open circles) targets. The spectral absorption coefficient was varied by multiplying by a constant factor.

than that achieved in the course of implosion of the LANL target.

Figure 3 shows the spectra of X radiation emitted from the LANL target and the scaled target. The X-ray

energy yield was about 3 MJ for the NIF target and 150 kJ for the target proposed for the Iskra-6 facility.

Figure 4 shows the dependence of the fusion energy yield on the spectral absorption coefficient, which was varied by multiplying by a constant factor. The LANL target admits 60% variations in the absorption coefficient. The target for the Iskra-6 facility is more sensitive to the radiation mean-free-path length and admits 30% variations in the absorption coefficient.

Besides the calculations of the spectra, we performed three-temperature calculations for the NIF and Iskra-6 targets by the ERA code. The results obtained are in good agreement.

In this paper, we did not consider such important issues as the influence of mixing, the asymmetry of radiation on the target surface, and the roughness of the shell surface. These problems will be the subject of our further investigations.

REFERENCES

1. E. M. Campbell and J. W. Hogan, in *Inertial Fusion Sciences and Application-99*, Ed. by Christian Labaune, William J. Hogan, and Kazuo A. Tanaka (Elsevier, 2000), p. 9.
2. M. L. Andre, in *Inertial Fusion Sciences and Application-99*, Ed. by Christian Labaune, William J. Hogan, and Kazuo A. Tanaka (Elsevier, 2000), p. 32.
3. J. Lindl, Phys. Plasmas **2**, 3933 (1995).
4. G. A. Kirillov, G. G. Kochemasov, A. V. Bessarab, *et al.*, Laser Part. Beams **18**, 219 (2000).
5. E. N. Avrorin, V. A. Lykov, V. E. Chernyakov, *et al.*, Laser Part. Beams **15**, 145 (1997).
6. D. C. Wilson and W. J. Krauser, in *Laser Interaction with Matter: Proceedings of 23rd European Conference* (IOP, Bristol and Philadelphia, 1995), IOP Conference Series, No. 140, p. 459.
7. P. A. Bradley and D. C. Wilson, Phys. Plasmas **6**, 4293 (1999).
8. N. A. Barysheva, A. I. Zuev, N. G. Karlykhanov, *et al.*, Zh. Vychisl. Mat. Mat. Fiz. **22**, 401 (1982).
9. A. I. Zuev, Zh. Vychisl. Mat. Mat. Fiz. **32**, 82 (1992).
10. A. F. Nikiforov, V. G. Novikov, and V. B. Uvarov, *Quantum–Statistic Models of High-Temperature Plasma* (Fizmatlit, Moscow, 2000).

Translated by E. Satunina

Influence of Fermi-System Chirality on the Temperature Dependence of the Aharonov–Bohm Effect

A. A. Bykov[1, *], D. V. Nomokonov[1], A. K. Bakarov[1], A. V. Goran[1], O. Estibals[2], and J. C. Portal[2]

[1] *Institute of Semiconductor Physics, Siberian Division, Russian Academy of Sciences, pr. Akademika Lavrent'eva 13, Novosibirsk, 630090 Russia*
e-mail: bykov@thermo.isp.nsc.ru

[2] *Grenoble High Magnetic Fields Laboratory, MPI-FKF and CNRS B.P.166, F-38042 Grenoble, France*

Received November 13, 2003

The Aharonov–Bohm effect in submicron rings with narrow electron channels was studied in the range of magnetic fields from 0 to 15 T and temperatures from 0.1 to 10 K. It is found that the temperature dependences of the h/e-oscillation amplitude at low magnetic fields and in the situation of tunnel-coupled edge current states are different. The obtained experimental data are explained by the influence of Fermi-system chirality on the coherent transport in a ring interferometer. © 2004 MAIK "Nauka/Interperiodica".

PACS numbers: 73.23.-b; 73.40.Gk

It is known that the coherent processes occurring in a ring interferometer placed in a uniform external magnetic field B are governed not only by the flux through the ring inner area but also by the flux through the electron channels of the interferometer. As a result, the magnetoconductance of metallic rings operating in the diffusion charge-carrier transport regime exhibits, apart from Aharonov–Bohm oscillations, universal conductance fluctuations [1, 2]. The flux through the electron channels in semiconductor ballistic interferometers fabricated on the basis of a high-mobility two-dimensional electron gas (2DEG) modifies the ring energy spectrum and induces Aharonov–Bohm oscillation beats [3, 4]. In a high magnetic field, the flux through the channels of a ballistic ring gives rise to edge current states, in which electrons can move only in one direction. In these conditions, the symmetry of charge-carrier transport breaks and the Fermi system becomes chiral.

According to [5, 6], the influence of chirality on the coherent processes in the interferometer is as follows. The magnetic flux through the ring in a nonchiral system (Fig. 1a) gives rise to both constructive and destructive interference of electron waves, whereas the chiral system allows only constructive interference (Fig. 1b). This distinction in the transport through the ring should primarily manifest itself in the temperature dependence of the Aharonov–Bohm effect. This follows from the fact that h/e oscillations in the nonchiral system are suppressed when the temperature length L_T becomes shorter than the circle half-length $L/2$, whereas, in the chiral system, this occurs when L_T is shorter than L, where $L_T = \hbar v/k_B T$ and v is the Fermi velocity. The interval of magnetic fields where the Aha-ronov–Bohm oscillations appear in the ballistic rings is determined by the width of electron channels; the narrower the channels, the broader this interval [7, 8].
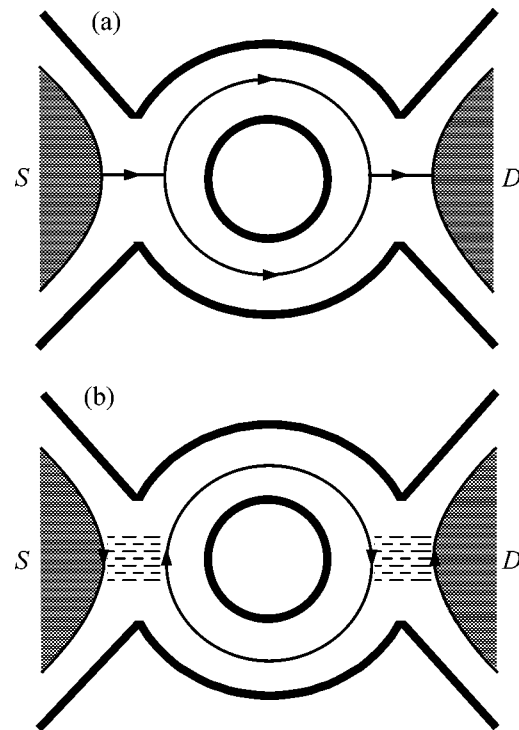
Fig. 1. (a) Scheme of charge-carrier motion in the ring in a low magnetic field. (b) Scheme of charge-carrier transfer in the ring in the presence of tunnel-coupled edge current states. Dashes set off the regions of tunneling between edge states. The 2DEG regions are shaded grey.

Because of this, ballistic rings with narrow electron channels allow the transition from the nonchiral to chiral system to be followed from its onset to its completion upon increasing B. The purpose of this work is to study the temperature dependence of the Aharonov–Bohm effect in such rings and to reveal experimentally the role of chirality in the suppression of the h/e-oscillation amplitude with increasing temperature.

Interferometers for study were fabricated on the basis of 2DEG in single GaAs quantum wells with AlAs/GaAs superlattice barriers [9]. Contrary to the gas in a GaAs/AlGaAs heterojunction, two-dimensional electron gas in our structures can simultaneously be highly mobile and have high concentration, allowing the fabrication, on its basis, of ballistic rings of submicron sizes [10]. The 2DEG concentration and mobility in the starting structure grown from molecular beam epitaxy were, respectively, $n_s = 1.8 \times 10^{12}$ cm^{-2} and $\mu = 4 \times 10^5$ cm^2/(V s) at $T = 4.2$ K. The schematic view of the interferometer is shown in Fig. 2a. Double bridges with a width of 50 µm and a separation between the potentiometric terminals of 100 µm were fabricated using optical lithography and liquid etching. The ring was placed between two pairs of potentiometric terminals and fabricated using electron beam lithography and dry etching. The ring effective radius determined from the period of h/e oscillations was $r_{eff} = 0.13$–0.15 µm and coincided, within this accuracy, with the mean radius given by electron beam lithography. Experiments were carried out in the range of magnetic fields from 0 to 15 T and temperatures from 0.1 to 10 K.

In Fig. 2b, the magnetic-field dependences of the interferometer longitudinal (R_{23}) and transverse (R_{37}) resistances are presented for $T = 1.4$ K and B values ranging from 0 to 15 T. It is seen from this figure that the 2DEG transverse resistance (R_{37}) in magnetic fields above 5 T assumes quantized values. However, the quantization is not seen in the four-terminal ring resistance (R_{23}) up to 15 T. This implies that, in a high magnetic field, the situation of tunnel-coupled edge current states appears in the narrowest ring input/output regions of the interferometer and in the conducting channel waists [10–12]. A distinguishing feature of the Aharonov– Bohm effect in the interferometers studied is that the h/e oscillations (ΔR_{23}) are most pronounced in the situation where the Fermi level in the two-dimensional source (S) and drain (D) regions coincides with the energy of the latter with the half-filled Landau level. This is clearly seen in Fig. 3a, where it is shown that the amplitude of Aharonov–Bohm oscillations correlates with the Shubnikov–de Haas oscillations. The results of fast Fourier transform in different intervals of magnetic field are presented in Fig. 3b. It follows from the curves that both the peak amplitude and its low-frequency shift increase with an increase in the magnetic field.

The $\Delta G(B)$ dependence of the periodic component of ring conductance is shown in Fig. 4a for two different temperatures. One can see that the h/e-oscillation
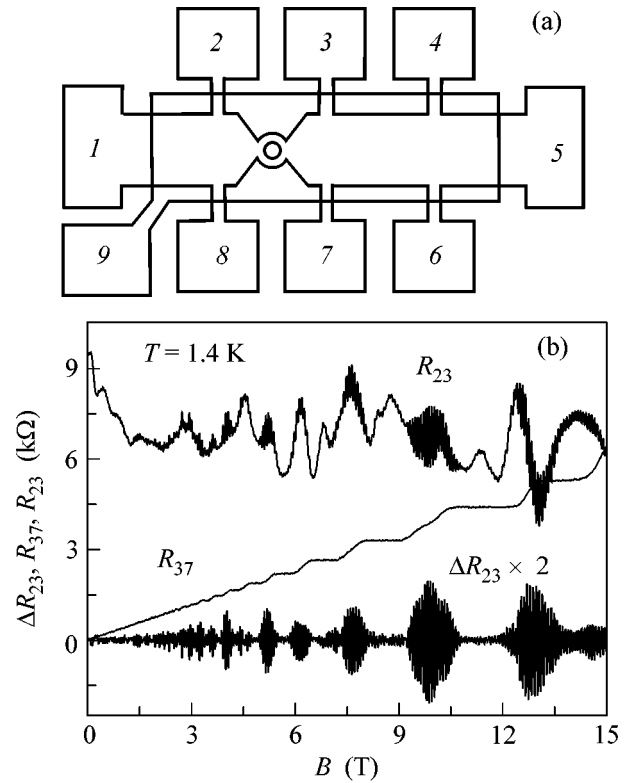

Fig. 2. (a) Schematic of the ring interferometer. (*1, 5*) Current terminals; (*2, 3, 4, 6, 7, 8*) potentiometric terminals; and (*9*) thin-film metallic gate. (b) Experimental $R_{23}(B)$ and $R_{37}(B)$ curves and the differences $\Delta R_{23}(B)$ between the experimental and smoothed curves at $T = 1.4$ K.

amplitude decreases with increasing temperature faster at high magnetic fields than at lower fields. Moreover, the Aharonov–Bohm oscillations undergo a "shift" upon changing temperature at high B values, whereas it is absent in low magnetic fields. Figure 4b shows that the temperature dependences of the relative amplitude G_{AB}/G_{AB0} of Aharonov–Bohm oscillations, where G_{AB0} is the h/e-oscillation amplitude at $T = 0.1$ K, become steeper as the magnetic field increases.

It is pointed out above that one of the distinctive features of the interferometers of interest is that the h/e-oscillation amplitude correlates with the Shubnikov–de Haas oscillations in the 2DEG regions adjacent to the ring. The increase in the resistance R_{23} in the B intervals where the Aharonov–Bohm oscillations are suppressed (Fig. 3a), while the resistance R_{34} becomes zero, allows the assumption to be drawn that this correlation is caused by strengthening of the backscatter under the conditions where the quantum Hall effect occurs in the source and drain regions. An unambiguous interpretation of the experimentally observed correlation requires the development of a model for this phenomenon, although this is beyond the scope of this work.
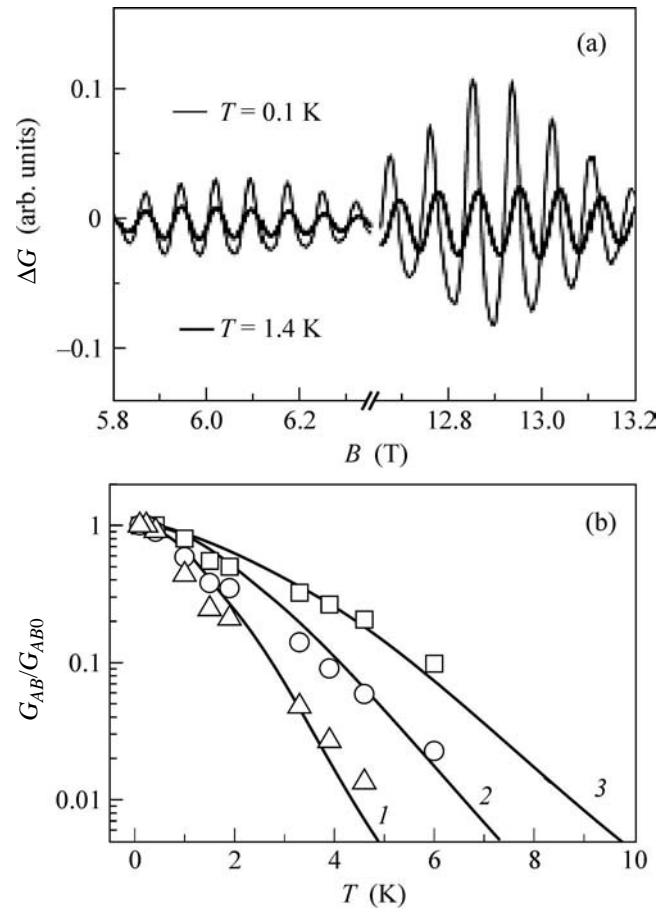
As in [7, 8], the fact that the period of h/e oscillations increases with B (Fig. 3b) is related in this work
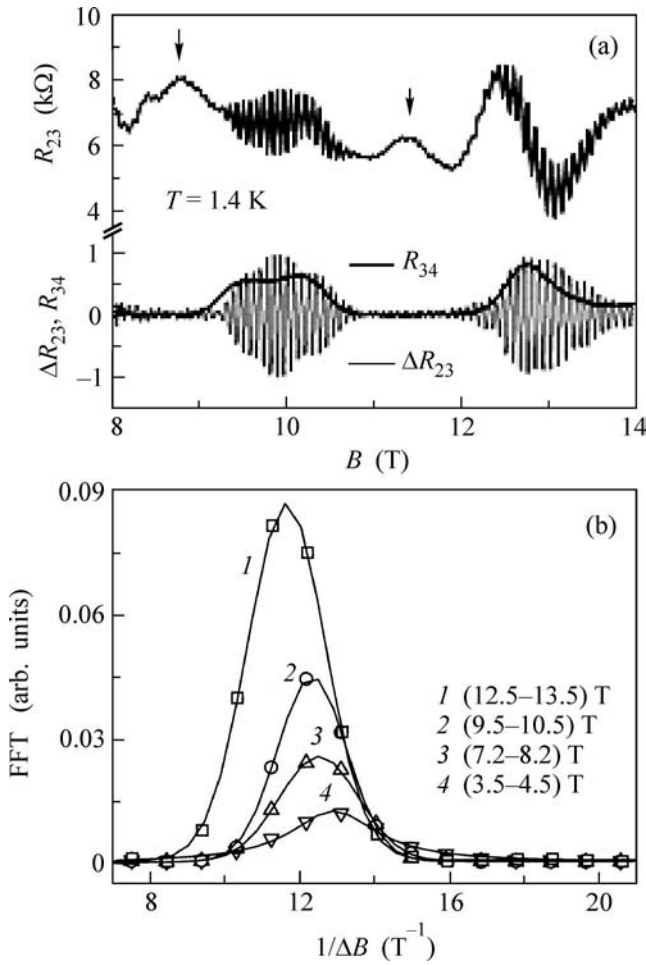
Fig. 3. (a) The $R_{23}(B)$, $R_{34}(B)$, and $\Delta R_{23}(B)$ dependences at $T = 1.4$ K. Arrows indicate maxima on the $R_{23}(B)$ curve in the interval of fields where $R_{34}(B) = 0$. (b) Lorentz-approximated results of the fast Fourier transform of the $\Delta R_{23}(B)$ functions in different intervals of magnetic field: (*1*) 12.5–13.5, (*2*) 9.5–10.5, (*3*) 7.2–8.2, and (*4*) 3.5–4.5 T.

Fig. 4. (a) The $\Delta G(B)$ dependences in two different intervals of B at $T = 0.1$ and 1.4 K. (b) Temperature dependences of the relative amplitude G_{AB}/G_{AB0} ($G_{AB0} = G_{AB}(0.1$ K)) of Aharonov–Bohm oscillations in different intervals of B: (squares) 2.8–3.3, (circles) 7.2–7.7, and (triangles) 12.7–13.2 T. Calculations by formula $G_{AB}/G_{AB0} = (T/T_0)/\sinh(T/T_0)$ from [6]. $T_0 = $ (*1*) 0.6, (*2*) 0.9, and (*3*) 1.2 K.

to the decrease in the effective radius of the closed ring edge state through which electrons are tunneling. Such a behavior is evidence for the formation of the edge states and is indicative of a change in the chirality of Fermi system with an increase in magnetic field. The fact that the temperature dependences of the Aharonov–Bohm effect are different in a low magnetic field and under conditions of the tunnel-coupled edge current states (Fig. 4b) is also related to the change in chirality.

The temperature dependence of the Aharonov–Bohm effect in a chiral Fermi system was theoretically analyzed in [5, 6]. The h/e-oscillation amplitude in such a system is determined by the lengths L and L_T. In our case, $L = 2\pi r_{\text{eff}}$. If $L_T \gg L$, the h/e-oscillation amplitude is maximal and independent of T. In the opposite case, $L_T \ll L$, the coherent processes are fully suppressed and the Aharonov–Bohm effect does not occur. The characteristic temperature separating these limiting cases is

given by the expression [6] $T_0 = \hbar v/\pi k_B L$. The shorter L, the higher the characteristic temperature, all things being the same. It is pointed out above that, in contrast to the situation with tunnel-coupled edge states, the Fermi system is nonchiral in a low magnetic field, and the value of T_0 in this case will be determined not by the full length L but by its half. This signifies that T_0 should change twofold upon the transition from low to high fields. In [6], it was shown that the Aharonov–Bohm oscillation amplitude normalized to its zero-temperature value is given by the relation $G_{AB}/G_{AB0} = (T/T_0)/\sinh(T/T_0)$. Curves *1*, *2*, and *3* in Fig. 4b are calculated by this formula for different T_0 values. One can see that the experimental temperature dependences are consistent with the theoretical curves. As the magnetic field increases, the fitting parameter T_0 decreases from 1.2 to 0.6 K; i.e., in the ring interferometers studied, T_0 in a low magnetic field differs approximately twofold

from its value in the regime of tunnel-coupled edge current states, in compliance with the change in chirality of the Fermi system.

Thus, the temperature dependences of the Aharonov–Bohm effect in submicron rings with narrow conducting channels have been studied experimentally in the range of magnetic fields from 0 to 15 T. In the interferometers studied, not only the suppression of the Aharonov–Bohm oscillations but also their shift have been observed upon increasing temperature in a high magnetic field. It has been found that the slope of the temperature curve for the h/e-oscillation amplitude in a low magnetic field differs from that in the situation with the tunnel-coupled edge current states. The obtained experimental data are explained by the fact that the chirality of the Fermi system changes with increasing magnetic field. This is consistent with the theoretical results obtained in [6].

REFERENCES

1. A. D. Stone, Phys. Rev. Lett. **54**, 2692 (1985).

2. R. A. Webb, S. Washburn, C. P. Umbach, and R. B. Laibowitz, Phys. Rev. Lett. **54**, 2696 (1985).

3. W.-C. Tan and J. C. Inkson, Phys. Rev. B **53**, 6947 (1996).

4. A. A. Bykov, Z. D. Kvon, and E. B. Olshanetskii, Inst. Phys. Conf. Ser. **145**, 909 (1996).

5. M. R. Geller, D. Loss, and G. Kirczenow, Phys. Rev. Lett. **77**, 5110 (1996).

6. M. R. Geller and D. Loss, Phys. Rev. B **56**, 9692 (1997).

7. G. Timp, P. M. Mankiewich, P. de Vegvar, *et al.*, Phys. Rev. B **39**, 6227 (1989).

8. O. Estibals, A. A. Bykov, A. K. Bakarov, *et al.*, Inst. Phys. Conf. Ser. **171**, B1 (2003).

9. A. A. Bykov, A. K. Bakarov, L. V. Litvin, and A. I. Toropov, Pis'ma Zh. Éksp. Teor. Fiz. **72**, 300 (2000) [JETP Lett. **72**, 209 (2000)].

10. A. A. Bykov, D. V. Nomokonov, A. K. Bakarov, *et al.*, Pis'ma Zh. Éksp. Teor. Fiz. **78**, 36 (2003) [JETP Lett. **78**, 30 (2003)].

11. A. A. Bykov, D. G. Baksheev, L. V. Litvin, *et al.*, Pis'ma Zh. Éksp. Teor. Fiz. **71**, 631 (2000) [JETP Lett. **71**, 434 (2000)].

12. A. A. Bykov, Z. D. Kvon, E. B. Ol'shanetskiǐ, *et al.*, Pis'ma Zh. Éksp. Teor. Fiz. **58**, 897 (1993) [JETP Lett. **58**, 839 (1993)].

Translated by V. Sakun

Influence of Impurities on the Metallization of Inert Gases at High Pressures

Yu. B. Kudasov* and A. S. Korshunov

Russian Federal Nuclear Center, Institute of Experimental Physics,
Arzamas-16, Nizhni Novgorod region, 607188 Russia
*e-mail: kudasov@ntc.vniief.ru
Received November 14, 2003

It is shown that the introduction of heavy inert gas impurities into the condensed phase of a lighter inert gas can significantly change the kinetic properties of the latter at high pressures. The electronic structure of the ordered $Ar_{15}Xe$ solid solution is calculated. Doping of the condensed phase of a light inert gas with atoms of a heavier inert gas may become a new convenient tool in high-pressure experiments. © *2004 MAIK "Nauka/Interperiodica".*

PACS numbers: 71.30.+h; 71.55.-i; 62.50.+p

Metallization of condensed inert gases at high pressures has attracted considerable attention for a long time [1–11]. This is primarily due to the fact that inert gas atoms have completely filled and spherically symmetric outer electronic shells. For this reason, the analysis of the electronic structure and the interpretation of experimental results for these objects are considerably simplified. Pressures in the megabar range required for studying metallization can be created using several experimental techniques: static (in diamond cells [1–3]) and dynamic (isentropic [4] and quasi-isentropic [5] compression). The transition to the metal phase at low temperatures was studied in detail only for xenon. It was proved that xenon exhibits a structural transition from the face-centered cubic (fcc) to the hexagonal closely packed (hcp) lattice at a pressure of 0.7–0.9 Mbar; a transition to the metal phase occurs at 1.37 Mbar [1, 2]. The metallization pressure increases with decreasing atomic number; for this reason, experimental studies of krypton and argon are much more complicated [4–6]. The comprehensive theoretical analysis of the electronic structure of inert gases [7–11] has proved, among other things, that the pressures corresponding to metallization of neon and helium noticeably exceed modern experimental potentialities [10, 11].

Under low pressures, the Fermi level in Ne, Ar, Kr, and Xe crystals lies in the energy gap between the valence p band and the conduction s band. With increasing pressure, the gap becomes narrower, and an insulator becomes an intrinsic semiconductor and then a metal (when the conduction band overlaps with the valence band). It is well known that the introduction of donor or acceptor impurities in an intrinsic superconductor can radically change its kinetic properties. Thus, it would be interesting to analyze the effect of impurities on the properties of condensed inert gases at high pressures.

Doping impurities for elementary semiconductors are usually elements of the neighboring groups in the periodic table. For inert gases, Group I and II metals could be donor impurities, while Group VI and VII elements could serve as acceptor impurities. However, inert gases under normal pressure crystallize at cryogenic temperatures, and it is hardly possible to introduce metallic impurities in atomic form into these gases. It is also difficult to introduce Group VI and VII elements in atomic form into such a crystal, since such impurities in the liquid or solid phase of a inert gas will be, in all probability, in molecular form with the filled molecular shell (e.g., F_2, Cl_2, or O_2).

At the same time, atoms of a different inert gas can easily be introduced as an impurity into a condensed inert gas. Let us consider a crystal formed by atoms of a light inert gas with an impurity of atoms of a heavier inert gas (e.g., an Ar crystal with a Xe impurity). With increasing atomic number, the binding energy of outer electrons with the ion core becomes lower; i.e., the first ionization potential decreases. It is mainly for this reason that the energy gap for light inert gases in the solid phase is larger and the metallization pressure is higher. Thus, at low pressures, the impurity states of heavy inert gases must lie in the energy gap and have the form of very deep donor levels (see Fig. 1a). Since $E_d \approx E_g$, the impurity level practically does not affect the electrical conductivity. As the pressure increases and the gap becomes narrower, this level approaches the conduction band bottom and the intrinsic semiconductor becomes an *n*-type semiconductor when the energy gap width becomes quite small (see Fig. 1b). From the standpoint of physics, this situation means that an increase in temperature first leads to thermal ionization
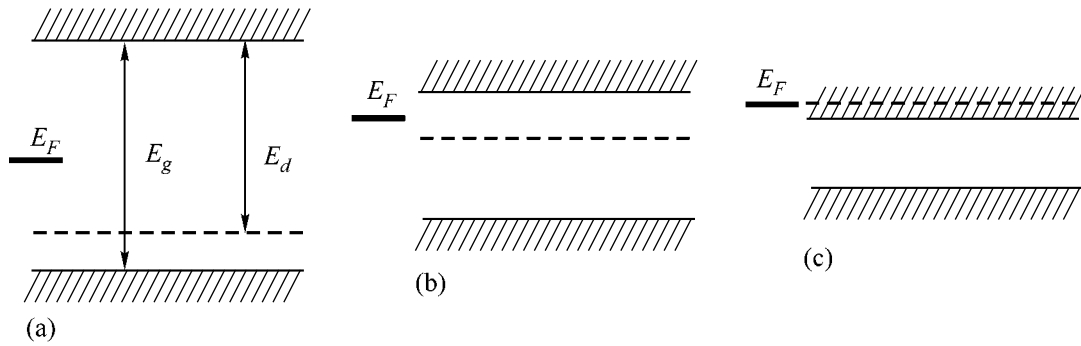
Fig. 1. Variation of the position of the impurity level upon an increase in pressure from (a) to (c).

of impurity atoms due to a comparatively weak coupling of their outer electrons with the ion core. Finally, a situation may arise where the impurity level enters the conduction band. This means that the semiconductor becomes degenerate; i.e., metallization of semiconductor takes place (Fig. 1c).

In order to verify the hypothesis described above, we calculated the electronic structure of the solid inert gases using the full-potential linearized augmented plane wave (FPLAPW) method with software packages Wien2k (version 02) [12] and XCrysDen (version 0.6.0) [13, 14]. We carried out precision calculations (5000 points in the Brillouin zone) of the total crystal energy E, the electronic structure, and the optical spectra for pure inert gases at high pressures in the fcc and hcp phases at $T = 0$ K. Calculations were made for various sizes of the unit cell, i.e., for fixed values of volume V. To construct the equation of state, we calculated the total energy $E(V)$ of the crystal as a function of its volume. Then, we approximated the energy by a smooth function of the form [5]

$$E = 3V_0 \sum_{i=1}^{4} \frac{a_i}{i} \left[\left(\frac{V_0}{V} \right)^{i/3} - 1 \right],$$

where V_0 is the volume at normal pressure. Coefficients a_i were determined by the least square method. The pressure was calculated as $P = -\partial E/\partial V$. Good agreement between the calculated and experimental results was achieved (the results will be described in greater detail in a separate publication).

We also studied the effect of Xe impurities on the electronic structure of an Ar crystal in the hcp phase. For this purpose, we took for a unit cell a supercell consisting of eight $(2 \times 2 \times 2)$ primitive hcp cells, which, in turn, contained two Ar atoms each. One of the Ar atoms in this supercell was replaced by an impurity (xenon) atom. Thus, we actually studied an ordered solid substitutional $Ar_{15}Xe$ solution. It should be borne in mind in the calculations that a superlattice contains eight nonequivalent positions of Ar atom. Calculations were made on a mesh with 500 points in the Brillouin zone. For the exchange correlation potential, we used the

potential of the generalized gradient approximation (PBE GGA) [15]. Since the compressibility of xenon is smaller than that of argon, the pressure curve (in the $P–V$ plane) for $Ar_{15}Xe$ is slightly higher than for pure Ar with the same cell volume.

Figure 2 shows the densities of states for pure Ar in the hcp phase and for the ordered $Ar_{15}Xe$ solution at various pressures. It can be clearly seen that, under low pressure, an impurity state of Xe appears in the energy gap of $Ar_{15}Xe$. This state is concentrated almost completely at the Xe atom (dashed curve). The difference between the total density of states and the density of states at xenon corresponds to the density of states at 15Ar atoms. It should be noted that the smearing of the impurity level into an impurity band is observed due to the high concentration of impurity in our calculations. As the pressure increases, the donor impurity band approaches the conduction band and becomes broader due to stronger overlap of atomic orbitals. At a pressure of 4.4 Mbar, the gap in the density of states of the ordered $Ar_{15}Xe$ solution is not observed, in contrast to the situation with pure Ar.

The case of doping the condensed phase of heavy inert gas with atoms of a lighter inert gas is less interesting, since the impurity level lies deeply in the valence band and does not noticeably affect the electrical conductivity.

The results described above lead to the following two conclusions, which are important for applications. First, in the analysis of the conductivity of condensed inert gases, it is necessary to make allowance for the fact that even minor impurities of heavier inert gases can noticeably change the electrical conductivity in the semiconducting phase and introduce an error in the measured value of the metallization pressure. Second, the controllable introduction of impurities of heavy inert gases into lighter inert gases may become a new tool in their investigation under high pressures. For example, the argon metallization pressure lies in the range of 5–6 Mbar [7], which exceeds the values attainable with static methods of producing ultrahigh pressures. It was noted above that the metallization pressure for neon and, the more so, for helium can hardly be
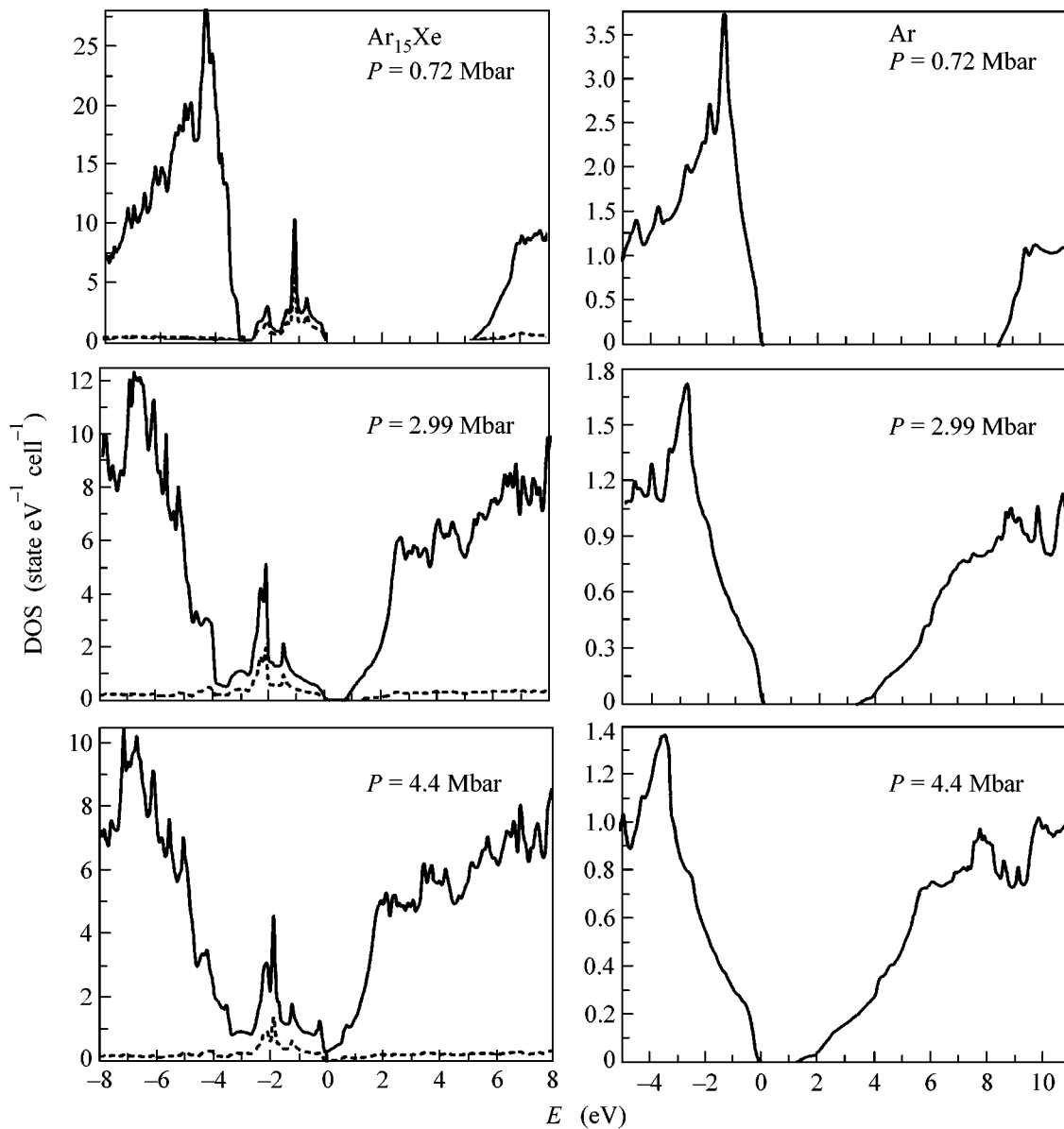
Fig. 2. Density of states (DOS) of (left) $Ar_{15}Xe$ and (right) Ar in the hcp phase at various pressures. The solid curve corresponds to the total DOS, and the dashed curve describes the partial DOS at the Xe atom.

reached even using dynamic methods. However, when an impurity is introduced, the transition to the state of a degenerate semiconductor is mainly determined by the electron binding energy with an impurity atom; consequently, the introduction, for example, of a xenon impurity into neon will probably reduce the metallization pressure radically.

It was noted above that the broadening of the impurity level is associated with a high concentration of impurity in our calculations. Lowering of the impurity concentration can reduce this effect. For instance, the size of a superlattice could be increased up to 54 atoms ($3 \times 3 \times 3$ of primitive cells). Such a problem is quite solvable but requires a considerable increase in com-

puter power. In our computations, we disregarded the distortions of the crystal lattice in the vicinity of an impurity atom, which takes place due to the difference in the atomic radii. This effect may lead to a certain displacement and narrowing of the impurity band but does not qualitatively affect the results described above,

REFERENCES

1. A. P. Jepcoat, H. K. Mao, L. W. Finger, *et al.*, Phys. Rev. Lett. **59**, 2670 (1987).
2. R. Reichlin, K. E. Brister, A. K. McMahan, *et al.*, Phys. Rev. Lett. **62**, 669 (1989).

3. K. A. Gottel, J. H. Eggert, I. F. Silvera, and W. C. Moss, Phys. Rev. Lett. **62**, 665 (1989).

4. L. R. Veeser, C. A. Ekdahl, H. Oona, *et al.*, in *Digest of Technical Papers of 11th IEEE International Pulsed Power Conference*, Ed. by G. Cooperstein and I. Vitkovitski (Baltimore, USA, 1997), Vol. 1, p. 384.

5. I. A. Adamskaya, F. V. Grigor'ev, O. L. Mikhaĭlova, *et al.*, Zh. Éksp. Teor. Fiz. **93**, 647 (1987) [Sov. Phys. JETP **66**, 366 (1987)].

6. M. Ross, H. K. Mao, P. M. Bell, and J. A. Xu, J. Chem. Phys. **85**, 1028 (1986).

7. I. Kwon, L. A. Collins, J. D. Kress, and N. Troullier, Phys. Rev. B **52**, 15165 (1995).

8. M. Ross and A. K. McMahan, Phys. Rev. B **21**, 1658 (1980).

9. A. K. McMahan, Phys. Rev. B **33**, 5344 (1986).

10. J. C. Borttger, Phys. Rev. B **33**, 6788 (1986).

11. J. Hama, Phys. Lett. A **105A**, 303 (1984).

12. P. Blaha, K. Schwarz, P. Sorantin, and S. B. Trickey, Comput. Phys. Commun. **59**, 339 (1990).

13. T. Kokalj, J. Mol. Graph. Model. **17**, 176 (1999).

14. T. Kokalj and M. Causa, in *Proceedings of High Performance Graphics Systems and Applications European Workshop* (Bologna, 2000), p. 51.

15. J. P. Perdew, K. Burke, and M. Ernzerhof, Phys. Rev. Lett. **77**, 3865 (1996).

Translated by N. Wadhwa

Conductance of a Multiterminal Ballistic Wire

Z. D. Kvon[1], V. A. Tkachenko[1, *], A. E. Plotnikov[1], V. A. Sablikov[2], V. Renard[3], and J. C. Portal[3]

[1] *Institute of Semiconductor Physics, Siberian Division, Russian Academy of Sciences, Novosibirsk, 630090 Russia*
*e-mail: vtkach@isp.nsc.ru
[2] *Institute of Radio Engineering and Electronics, Russian Academy of Sciences, Fryazino, Moscow region, 141190 Russia*
[3] *Grenoble High Magnetic Fields Laboratory, MPI-FKF and CNRS, F-38042 Grenoble, France*
Received November 20, 2003

An experimental study of the two-, three-, and four-terminal resistance of a ballistic wire is carried out. The wire is fabricated on the basis of high-mobility 2D electron gas in an AlGaAs/GaAs heterojunction. Different behavior of mesoscopic fluctuations of multiterminal resistances is observed depending on the gate voltage and magnetic field. At $B = 0.45$ T, the four-terminal resistance drops almost to zero and features resembling a ballistic conductance quantization are observed. © *2004 MAIK "Nauka/Interperiodica".*

PACS numbers: 73.23.Ad

Over a period of more than ten years after the discovery of conductance quantization in a ballistic wire, no experimental data on the distribution of voltage along the wire was available. In measuring this distribution by potentiometric probes, two problems arise. The first problem consists in that the terminals connecting the probes and the wire should not affect the properties of the latter [1]. The second problem is related to the fact that, generally speaking, the potential measured by a probe is not equal to the local potential of the wire [2, 3]. The existing theories of ballistic transport give no universal relationship between these quantities [3, 4].

Recently, three- and four-terminal resistances of a long (~6 μm) ballistic wire were measured under the conditions when the transparency of potentiometric probes was much smaller than the transparency of the wire itself [5]. The wire was fabricated by an unconventional method on a cleaved surface of an AlGaAs/GaAs heterostructure. The analysis of measurements suggested the conclusion [5] that the voltage applied to the wire equally drops in the near-terminal regions while the voltage drop between the probes is equal to zero. However, it is necessary to note that zero voltage between the probes cannot be considered as proof of quasi-neutrality (zero drop of potential) inside the ballistic wire [3]. In addition, in the structure studied in the cited experiment, a nonadiabatic (nonplanar) connection of the wire with the terminals was used. Therefore, the quantization steps of the two-terminal conductance of a short part of the wire had a noticeably smaller height than the quantum $2e^2/h$ (the two-terminal conductance of the whole multiterminal wire was not measured). The width of the contact of each probe with the wire was close to the length of the free part of the wire, so that the measured potential was averaged over a relatively large length. Nevertheless, the results of this experiment fit well the single-particle model of ballistic

wires [1–4], and they caused a number of questions concerning electron interactions. Calculations [6, 7] showed that the interaction of electrons with the self-consistent field of the charge arising in such a wire leads to the situation when the major part of voltage applied to the wire drops near the reservoirs while the rest of the wire remains almost equipotential.

In this paper, we present the results of studying the problem described above by using a ballistic wire that was fabricated in a standard way on the basis of an AlGaAs/GaAs heterojunction with 2D electron gas and with probe terminals that were much narrower than in [5]. The mobility of 2D electron gas in the initial structures was equal to $\mu = 10^6$ cm²/(V s), the electron concentration was $N_s = 4 \times 10^{11}$ cm⁻², and the corresponding mean free path was $l = 10$ μm. The fabrication procedure was as follows. First, electron lithography and plasma chemical etching were used to fabricate the wires with a lithographic length of $L = 1.2$–1.4 μm and width of $WL = 0.4$–0.5 μm and with two potentiometric probes of width $Wp = 0.3$–0.4 μm. The presence of the probes made it possible to measure two-, three-, and four-terminal resistances of the wire with the transparency of the probes being much lower than the transparency of the wire. The last stage of the fabrication procedure was the deposition of a TiAu metal gate on top of the structure. The topology and dimensions of the wires are shown in Fig. 1.

To determine the effective width and length of the wire and the terminals, as well as the number of modes transmitted through them, we performed a numerical simulation of the electrostatic potential and energy spectrum of the wire with allowance for the real technological parameters (the structure of the initial heterojunction, the etch depth, the presence of the upper metal layer, etc.). Methods and examples of such a simulation

were described in [8, 9] in application to other semiconductor devices. Figure 1 shows one of the results of simulation for the wire under study. One can see that, already at zero gate voltage, electrons are present in the wire (calculations show that, at $V_g = 0$, the transmission through the wire is open for two modes, while the potentiometric terminals represent an impenetrable barrier). Only when the third mode becomes open in the wire, the barrier in the terminal region is lowered so as to allow one mode to penetrate to the potentiometric terminal. This property of the structure under study means that the potentiometric terminals become suitable for multiterminal resistance measurements when three or more modes are transmitted through the wire.

Measurements of two- (R_{1212}), three- (R_{1213} and R_{1242}), and four-terminal (R_{1234}) resistances were carried out in a temperature range of 0.2–1.5 K, in a linear regime, at gate voltages corresponding to the transmission of several (three to six) modes through the wire. The resistances are expressed in terms of the terminal potentials and the current I_{12} through the wire: $R_{1212} = V_{12}/I_{12}$, $R_{1213} = V_{13}/I_{12}$, $R_{1242} = V_{42}/I_{12}$, and $R_{1234} = V_{34}/I_{12}$. Figure 2a shows the dependence of the two-terminal resistance R_{1212} on the gate voltage V_g at a temperature of 0.2 K in the interval of V_g from –60 to 150 mV. The dependence exhibits weak features corresponding to the quantization of the first two modes and no such features for higher-order modes. The features are most pronounced in the derivative $R' = -dR_{1212}/dV_g$. For comparison, Fig. 2b shows the dependences of the two-terminal resistances of the probes: $R_{1313}(V_g)$ and $R_{4242}(V_g)$. From the position of the first step, one can see that the probes are slightly different and that they become open at $V_g \approx 60$ mV, i.e., when three modes have already been transmitted through the wire. The height of the step noticeably exceeds the resistance quantum $h/2e^2 = 12.9$ kΩ, because the measured values of R_{1313} and R_{4242} contain the contribution of the series resistances of the probe leads, whose values exceed 10 kΩ. When $V_g < 40$ mV, the resistance of the probes becomes too large to allow a correct measurement of potential difference and, hence, three- and four-terminal resistances of the wire.

Figure 3 presents the dependences of two-, three-, and four-terminal resistances on the gate voltage for the same sample in the interval of V_g from 40 to 200 mV. From this figure, one can see that (i) the dependence of the two-terminal resistance $R_{1212}(V_g)$ is smooth and contains no features, (ii) the four-terminal resistance $R_{1234}(V_g)$ is five times smaller than $R_{1212}(V_g)$ but far from zero, and (iii) the three- and four-terminal resistances exhibit mesoscopic oscillations within $V_g = 40$–60 mV. Thus, in zero magnetic field, the wire under study exhibits a weak quantization step of the two-terminal conductance, which corresponds to the propagation of the principle mode, and barely noticeable features, which correspond to the propagation of two or
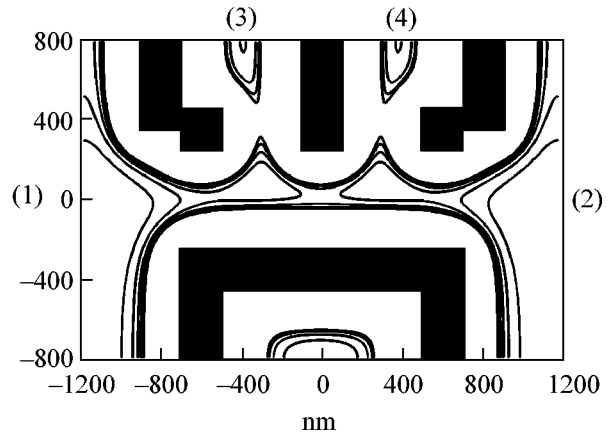

Fig. 1. Two-dimensional distribution of electron density in the wire (a half-tone image); the numbers of terminals are indicated in parentheses and the etch areas are shown by rectangles.
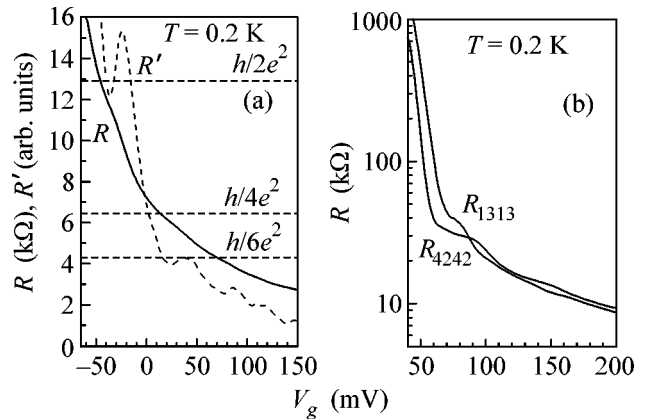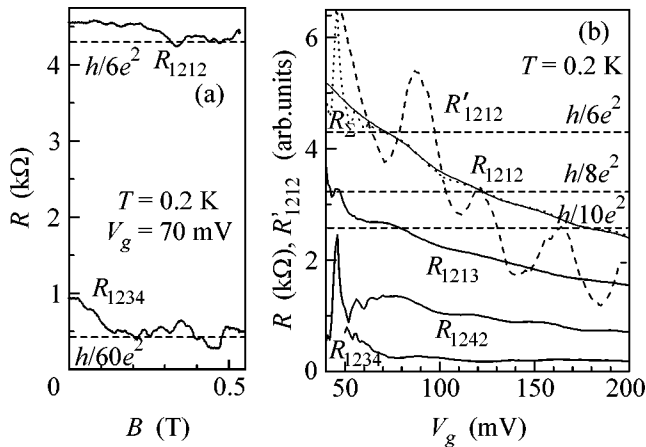

Fig. 2. Two-terminal resistances of (a) the wire and (b) the probes versus the gate voltage; $R' = -dR/dV_g$.

more modes. In addition, the wire has a noticeable value of four-terminal resistance, which is only 1.7 times smaller than that in the case of a diffuse wire ($lw \ll L$, where lw is the mean path length of electrons in the wire). Presumably, this situation is caused by the fact that the transmission of electrons through the wire is not ballistic but accompanied by their considerable scattering. The sources of this scattering may be individual impurities that occur inside the wire because of the insufficiently high mobility of electrons in the initial heterojunction, as well as quantum cavities formed at the points of contact of the wire with potentiometric probes. From Fig. 1, one can clearly see that the wire is not homogeneous along its length but represents a series connection of three constrictions and two potential wells, i.e., triangular quantum dots formed at the points of contact of the wire with the probes. Theoretical [8] and experimental [10] studies of triangular
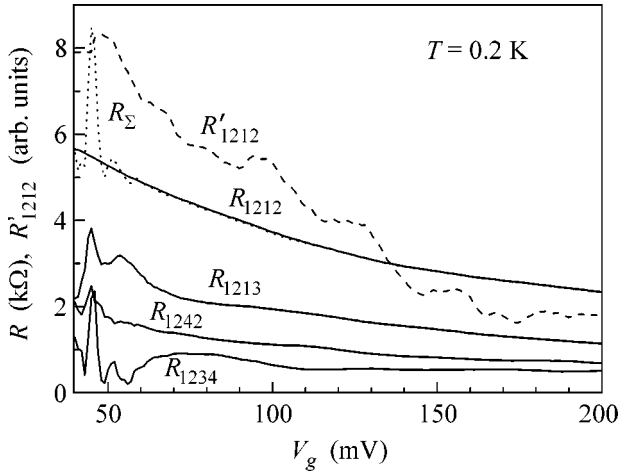
Fig. 3. Two- (R_{1212}), three- (R_{1213}, R_{1242}), and four-terminal (R_{1234}) resistances of the wire versus the gate voltage in zero magnetic field; $R' = -dR_{1212}/dV_g$ and $R_\Sigma = R_{1213} + R_{1242} + R_{1234}$.

Fig. 4. (a) Two- and four-terminal resistances of the wire versus the magnetic field and (b) the multiterminal resistances of the wire versus the gate voltage at $B = 0.45$ T; the notation is the same as in Fig. 3.

quantum dots in other structures suggest that these quantum cavities are the source of nonadiabaticity (strong intermode mixing), scattering, and inelastic processes, which suppress the quantization of the two-terminal resistance [11]. Therefore, potentiometric terminals positioned within the inner part of the wire strongly affect the ballistic transport regime characteristic of two-terminal wires. Most likely, the coherent resonance scattering by the triangular dots [8] is responsible for the mesoscopic oscillations observed for multiterminal resistances in the interval of $V_g = 40$–60 mV (Fig. 3). Evidence of coherence is the nonlocal character of the resistance, i.e., the large difference

between $R_\Sigma = R_{1213} + R_{1242} + R_{1234}$ and R_{1212}, which means that the total voltage drop in the wire is not equal to the sum of voltage drops in three series-connected elements of the wire (two triangular dots and the barrier between them). When $V_g > 70$ mV, the mesoscopic fluctuations disappear and the equality $R_\Sigma = R_{1212}$ is satisfied to a high accuracy.

Figure 4a shows the dependences of the two-terminal and four-terminal resistances of the wire on magnetic field at $V_g = 70$ mV. One can see that the resistance R_{1212} weakly depends on magnetic field except for the small-amplitude mesoscopic fluctuations. This suggests that, in the wire, the scattering from its lateral walls, which should lead to a high positive magnetoresistance, is absent. Unlike the small-amplitude mesoscopic fluctuations observed in the two-terminal resistance ($\delta R/R < 0.1$), the relative amplitude of the fluctuations observed in R_{1234} is much greater: $\delta R/R \sim 1$. This fluctuation behavior results in that, in a magnetic field of 0.45 T, the value of R_{1234} becomes four times smaller than its value in zero magnetic field. Figure 4b shows the dependences $R_{1212}(V_g)$, $R_{1234}(V_g)$, $R_{1213}(V_g)$, and $R_{1242}(V_g)$ measured precisely in the magnetic field of 0.45 T. One can see that the value of the four-terminal resistance R_{1234} remains small for all values of the gate voltage. In contrast to Fig. 3, the dependence R_{1212} exhibits small features in the form of inclined steps. For clarity, we also present the derivative $R' = -dR_{1212}/dV_g$. From this figure, one can see that the steps correspond to the transmission of three to five modes through the wire, although it should be noted that the step corresponding to the fourth mode is split into two steps.

Now, let us discuss the results described above. The main result is the observation of the magnetic field–controlled correlation in the behavior of R_{1212} and R_{1234}, which shows that, the smaller the value of the four-terminal resistance, the more pronounced the features resembling the conductance quantization. This result complements the experiment [5] in which the two-terminal conductance of a multiterminal wire was not measured. Our observation testifies that both the value of the four-terminal resistance and the presence of features in the two-terminal conductance are determined by the scattering of electrons in the wire–probe contact region. Another important result consists in that the values of the three-terminal resistances of the wire proved to be different. This points to a considerable difference between the perturbations introduced by the left and right probes into the electron transport through the wire. Presumably, it is this difference that gives rise to noticeable mesoscopic fluctuations of the three- and four-terminal resistances. The behavior of these fluctuations has a specific feature: they exist (see Figs. 3 and 4b) only when the probes and the wire are weakly coupled (the probe resistance is $R_p \gg h/2e^2$). As soon as a strong coupling ($R_p < h/2e^2$) arises between the probe and the wire, the fluctuations practically disappear. This

means that the opening of the probes leads to a strong relaxation of the phase of the wave function and, hence, to the suppression of mesoscopic fluctuations. A possible source of the relaxation is the outflow of electrons into the probe and then into the 2D sea. Since the current through the voltmeter is close to zero, the electrons returning to the wire have a phase independent of the phase of electrons in the wire [11].

Thus, the study described in this paper shows that a multiterminal wire represents a more complex object than expected. One of the main problems in studying such a wire is related to the quantum cavities formed in the wire–probe contact regions. These cavities cause an electron scattering (including inelastic one) accompanied by changes in charge and potential. As a result, both the electron scattering matrix and the potential of the probes vary in a complex way. The effect is evidenced by the absence of clearly pronounced quantization of conductance and by the large variations of multiterminal resistances. In addition, the behavior of mesoscopic fluctuations shows that, in a real wire, the phase relaxation time of the wave function changes in a jumplike manner. An analysis of these processes is an important problem which requires further investigation.

REFERENCES

1. H.-L. Engquist and P. W. Anderson, Phys. Rev. B **24**, 1151 (1981).
2. M. Buttiker, IBM J. Res. Dev. **32**, 317 (1988).
3. I. B. Levinson, Zh. Éksp. Teor. Fiz. **95**, 2175 (1989) [Sov. Phys. JETP **68**, 1257 (1989)].
4. M. Buttiker, Semicond. Semimet. **35**, 191 (1992).
5. R. de Picciotto, H. L. Stormer, L. N. Pfeiffer, *et al.*, Nature **411**, 51 (2001).
6. V. A. Sablikov, S. V. Polyakov, and M. Buttiker, Phys. Rev. B **61**, 13 763 (2000).
7. V. A. Sablikov and B. S. Shchamkhalova, Physica E (Amsterdam) **17**, 189 (2003).
8. O. A. Tkachenko, V. A. Tkachenko, D. G. Baksheev, *et al.*, Pis'ma Zh. Éksp. Teor. Fiz. **71**, 366 (2000) [JETP Lett. **71**, 255 (2000)].
9. O. A. Tkachenko, V. A. Tkachenko, D. G. Baksheyev, *et al.*, J. Appl. Phys. **89**, 4993 (2001).
10. Z. D. Kvon, O. Estibals, A. Y. Plotnikov, *et al.*, Physica E (Amsterdam) **12**, 815 (2002).
11. M. Buttiker, Phys. Rev. B **33**, 3020 (1986).

Translated by E. Golyamina

Melting of Metallic Hydrogen at High Pressures

V. V. Kechin

Institute of High-Pressure Physics, Russian Academy of Sciences, Troitsk, Moscow region, 142190 Russia
e-mail: kechin@hppi.troitsk.ru

The Lindemann equation was used to calculate the melting of metallic hydrogen. It is shown that, after transition from the molecular dielectric phase to the atomic metallic phase, hydrogen becomes a quantum liquid because of the atomic zero-point vibrations. The phase diagram of hydrogen is unique in that the molecular phase is the only solid phase of hydrogen. © 2004 MAIK "Nauka/Interperiodica".

PACS numbers: 64.70.Dv; 62.50.+p; 67.20.+k

The question of whether atomic metallic hydrogen will be solid or liquid is one of the main problems of high-pressure physics, planetary physics, and astrophysics. The relevant theoretical calculations are contradictory [1]. Some of them assume that metallic hydrogen will have anisotropic (or quasi-liquid) structure with a low packing density [2–5], and the others consider metallic hydrogen as having close-packed structure [6, 7]. It is assumed in some works that metallic hydrogen should undergo phase transitions under pressure [8, 9]. Finally, it is assumed that metallic hydrogen should be a quantum liquid [10, 11].

The dependence of the melting temperature T_m of metallic hydrogen on its volume V was calculated by different methods; the Bernal geometric theory [12], the defect theory [13], the theory of one-component plasma [14, 15], and the Lindemann theory [16, 17] were used (Fig. 1). To convert the $T_m(V)$ dependence into the $T_m(P)$ dependence, the equation of state obtained for metallic hydrogen by Kagan *et al.* [18] is used in Fig. 1 (the corrections for thermal pressure were not taken into account). The calculations devoted to melting of metallic hydrogen cover a period from 1966 to 1980; more recent calculations are lacking in the literature. Figure 1 also presents the melting curve of molecular hydrogen [19]. This curve was obtained by extrapolating the results of experimental measurements below 0.15 Mbar (1 Mbar = 100 GPa) using the melting equation recently published in [20]. This equation was used to predict the presence of a maximum on the melting curve of molecular hydrogen [19].

The melting curves of metallic hydrogen (Fig. 1) are inconsistent with the shock-wave experiments and *ab initio* simulations. From the shock experiments it follows that hydrogen is a liquid up to 1.8 Mbar in the temperature range 1600–3100 K and that it undergoes, under pressure, a continuous transition from semiconducting molecular liquid to molecular metal [21]. The *ab initio* simulation of hydrogen by the molecular

dynamics method has shown that hydrogen is a liquid at a temperature of 1000 K over the pressure range of 0.3–3.0 Mbar [22]. Analogous studies have shown that, at 1.5 Mbar and 1100 K, liquid hydrogen undergoes transition from the molecular to the atomic metallic state, and it becomes a metallic liquid at pressures of 3.8 and 24 Mbar in the temperature range 800–3000 K [23]; i.e., the melting temperature T_m of metallic hydrogen should be lower than 800 K at pressures of $P \geq$ 3.8 Mbar.

Melting calculation. In this work, the melting of metallic hydrogen at high pressure is calculated using the Lindemann equation [24]. Earlier, this method was used by Inoue and Ariyasu [17] (curve *3* in Fig. 1) and
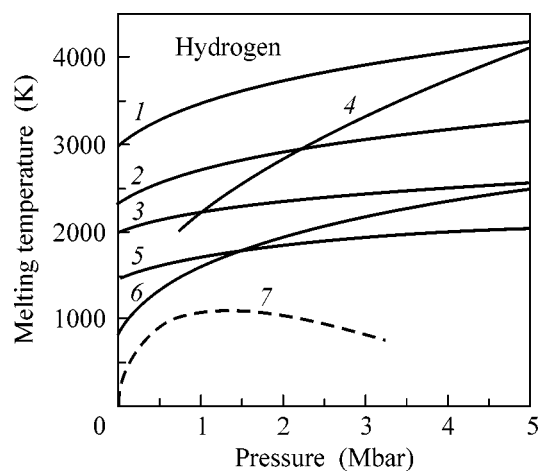
Fig. 1. Hydrogen melting curves under pressure. The solid lines correspond to atomic metallic hydrogen [12–17] and the dashed line corresponds to molecular hydrogen [19]: (*1*) theory of one-component plasma [14]; (*2*) Bernal geometric theory [12]; (*3*) Lindemann's melting theory [17]; (*4*) defect theory [13]; (*5*) theory of one-component plasma [15]; (*6*) Lindemann's melting theory [16]; and (*7*) extrapolation of the experimental data on melting of molecular hydrogen [19].

Stevenson and Ashcroft [16] (curve *6* in Fig. 1) for calculating the melting of metallic hydrogen. In those works, the Debye temperature was taken from the Trubitsyn expression [25] that was based on a simple method suggested by Abrikosov in [26]. Trubitsyn pointed out that the transverse waves caused by the Coulomb forces make the main contribution to the Debye temperature. Contrary to Inoue and Ariyasu [17], Stevenson and Ashcroft [16] distinguished between the transverse and longitudinal modes. The latter are mainly caused by the volume compressibility of electron gas. The Debye temperatures calculated by this method for metallic hydrogen were overestimated, and, hence, the obtained pressure dependence of the melting temperature proved to be incorrect.

The main distinction of this work is that the expression for the Debye temperature is derived using the phonon spectrum. In all variants of calculation of the structure of metallic hydrogen, it is assumed that the FCC lattice is most stable for metallic hydrogen at extremely high pressures. Caron [13] and Kagan *et al.* [18] calculated the phonon spectrum for the FCC lattice of metallic hydrogen. In the self-consistent harmonic approximation, Caron obtained the following expression for the Debye temperature [13]:

$$k\Theta_D = \frac{0.0453}{r_s^{3/2}} - \frac{0.023}{r_s^{1/2}} + 0.006r_s^{1/2}\text{Ry}. \quad (1)$$

Kagan *et al.* [18] derived the interpolation relation for the energy of zero-point vibrations, from which it follows that the expression for the Debye temperature of the FCC lattice has the form

$$k\Theta_D = \frac{0.055}{r_s^{3/2}} - \frac{0.041}{r_s^{1/2}} + 0.024 - 0.010r_s^{1/2}\text{Ry}. \quad (2)$$

According to the Lindemann's melting criterion, the ratio γ of the average vibrational amplitude to the closest interatomic distance R_{min} in a solid is constant along the melting curve. One often uses the Lindemann constant C_L instead of the Lindemann ratio γ. In the low-temperature limit of interest ($T_m \ll \Theta_D \approx 2000$ K), the Lindemann's melting equation has the form

$$T_m = \frac{\sqrt{6}\Theta_D}{\pi}\left(\frac{M\Theta_D V^{2/3}}{C_L^2} - \frac{1}{4}\right)^{1/2}, \quad (3)$$

where M is the atomic weight and V is the molecular volume. The factor 1/4 in Eq. (3) appears due to the atomic zero-point vibrations. If the expression on the right-hand side of Eq. (3) turns to zero, the melting temperature becomes $T_m = 0$. For example, the melting curves of Inoue and Ariyasu [17] and Stevenson and Ashcroft [16] (curves *3* and *6* in Fig. 1, respectively) predict that melting at $T_m = 0$ (so-called "cold" melting) induced by the zero-point vibrations occurs in hydrogen at a very high density of 21.9 g/cm^3 ($\approx$1.2 $\times$ 10^3 Mbar) and 4.6 $\times$ 10^3 g/cm^3 ($\approx$1.2 $\times$ 10^7 Mbar),

respectively (it will be shown below that this is not the case).

The Lindemann ratio γ is related to the Lindemann constant C_L by the expression $\gamma C_L = \beta\eta^{-1/3}$, where $\beta = 6^{1/6}\pi^{-2/3}hN^{5/6}k^{-1/2}$, h is the Planck's constant and N is Avogadro's number; i.e.,

$$\gamma C_L = 13.41\eta^{-1/3}, \quad (4)$$

where η is the packing density

$$\eta = \frac{4}{3}\pi(R_{min}/2)^3/V_{at}, \quad (5)$$

and V_{at} is the atomic volume. The packing density is $\eta = 0.74$, 0.74, 0.68, 0.52, and 0.32 for the FCC, HCP (see Appendix), BCC, simple cubic, and diamond structure, respectively.

The melting temperature strongly depends on the value of C_L, because it enters as C_L^2 in the Lindemann equation. It follows from the Lindemann equation that the smaller the Lindemann constant (the higher the packing density), the higher the melting temperature. Experiments suggest that the Lindemann empirical parameter C_L is the smallest for the cubic close-packed structures, and it is these structures that have melting temperatures higher as compared to the anisotropic low-packed structures [27, 28].

The average value of C_L is 218 for the HCP lattice, 148 for the FCC lattice, and 124 for the BCC lattice. Atomic hydrogen is alkali metal. For alkali metals, the average value is $C_L = 119$ ($C_L = 124$ for Li and $C_L = 114$ for Na). The hydrogen quantum Monte Carlo calculations suggest that the Lindemann ratio γ is 0.15 ($C_L = 102$) and 0.13 ($C_L = 114$) for the BCC and FCC lattices, respectively [7]. The analogous more recent studies [9] showed that $\gamma = 0.12$ ($C_L = 127$) for the BCC lattice, in good agreement with the experiment.

In this work, the Lindemann equation (3), expressions (1) and (2) for the Debye temperature, and various values of C_L were used to calculate the melting of metallic hydrogen. The computational results proved to be surprising. The right-hand side of Eq. (3) is imaginary for all values of C_L up to pressures of 3×10^5 Mbar. This signifies that metallic hydrogen has no melting curve and that hydrogen is a quantum liquid (due to the zero-point vibrations) at all pressures and temperatures.

Earlier, MacDonald and Burgess [10] showed that metallic hydrogen is a liquid at all pressures. Since the electron screening is essential only in the solid state and is of no importance in the liquid state, the latter is energetically lower than the solid state for all densities. Recently, Ashcroft also arrived at the conclusion that the metallic phase should be a liquid [29]. Liquid metallic phase represents the new class of quantum liquids [30] and the new matter state, namely, the state of a superconducting liquid [31].
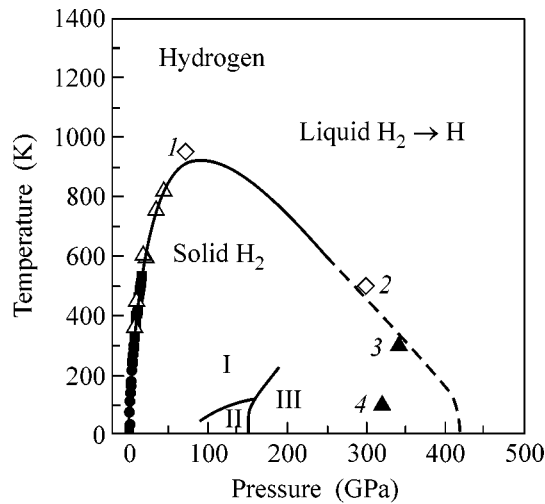
Fig. 2. Hydrogen phase diagram. Dark circles, dark squares, and light triangles are the experimental data obtained, respectively, in [32], [19], and [33] for the melting of molecular hydrogen. Solid line corresponds to the extrapolation of experimental data to 250 GPa using the melting equation from [20]. Dashed line is the assumed melting curve of molecular hydrogen at pressures $P > 250$ GPa. Point *1* corresponds to the discontinuity in the temperature dependence of vibronic frequency [33], presumably because of the first-order dielectric–metal phase transition in liquid hydrogen near the maximum on the melting curve, as predicted by the molecular dynamic *ab initio* simulation [34]; point *2* corresponds to the liquid phase according to this method [35]; points *3* and *4* correspond to the highest pressures achieved in diamond cells in [36] and [37], respectively; and II and III are the low-temperature phases of molecular hydrogen [38].

In summary, it has been shown that, due to the atomic quantum zero-point vibrations, hydrogen should be a quantum liquid after the transition from the molecular dielectric to the atomic metallic phase. Metallic hydrogen remains a liquid at all pressures and temperatures. The hydrogen phase diagram is unusual, because the molecular phase is the only solid phase of hydrogen (Fig. 2). When constructing Fig. 2, the experimental data obtained by Diatchenko *et al.* on melting under pressure ($0 \le P \le 7.7$ GPa) [32] and by Datchi *et al.* ($6.4 \le P \le 15.2$ GPa) [19], as well as the recent data on melting in diamond cells ($6.5 \le P \le 44$ GPa) [33] were used. These data were used to extrapolate the hydrogen melting curve to 250 GPa using the melting equation $T_m = 14.025(1 + P/0.02655)^{0.58665}\exp(-0.00637)$ obtained in [20]. At 300 K, the transition pressure to the metallic phase is equal to 350 GPa (Fig. 2). The highest pressure presently achieved in diamond cells at 300 K is 342 GPa [36], which is very close to this transition pressure.

The melting curve of the molecular phase is unique. It is simultaneously the interface between the solid and liquid phases, dielectric and metallic phases, and the molecular and atomic phases.

APPENDIX

The HCP structure has two branches in the dependence of packing density on the axes ratio $\delta = c/a$:

$$\eta = 2\sqrt{3\pi}/9\delta \quad (\delta \ge \delta_{id} = \sqrt{8/3}),$$

$$\eta = (2\pi/27\delta)\left(1 + \frac{3}{4}\delta^2\right)^{3/2} \quad (2/3 \le \delta \le \delta_{id}).$$

Cho [28] considered the role of lattice structure in the Lindemann's melting theory. For the HCP structure, he considered only one branch $\delta \ge \delta_{id}$. For this reason, his tables and drawings for the HCP metals with $\delta < \delta_{id}$ (Ru, Os, Re, Mg) are erroneous (otherwise, the packing densities of these metals would be higher than the packing density of an ideal HCP structure).

REFERENCES

1. E. G. Maksimov and Yu. I. Shilov, Usp. Fiz. Nauk **169**, 1223 (1999) [Phys. Usp. **42**, 1121 (1999)].

2. E. G. Brovman, Yu. Kagan, and A. Holas, Zh. Éksp. Teor. Fiz. **62**, 1492 (1972) [Sov. Phys. JETP **35**, 783 (1972)].

3. K. Ebina and H. Miyagi, Phys. Lett. A **142**, 237 (1989).

4. T. W. Barbee and M. L. Cohen, Phys. Rev. B **44**, 11563 (1991).

5. K. Johnson and N. W. Ashcroft, J. Phys.: Condens. Matter **10**, 11135 (1998).

6. D. M. Straus and N. W. Ashcroft, Phys. Rev. Lett. **38**, 415 (1977).

7. D. M. Ceperley and B. J. Alder, Phys. Rev. B **36**, 2092 (1987).

8. B. I. Min, H. J. F. Jansen, and A. J. Freeman, Phys. Rev. B **30**, 5076 (1984).

9. V. Natoli, R. M. Martin, and D. M. Ceperley, Phys. Rev. Lett. **70**, 1952 (1993).

10. A. H. MacDonald and C. P. Burgess, Phys. Rev. B **26**, 2849 (1982).

11. N. W. Ashcroft, J. Phys.: Condens. Matter **12**, A129 (2000).

12. L. G. Caron, J. Chem. Phys. **55**, 5227 (1971).

13. L. G. Caron, Phys. Rev. B **9**, 5025 (1974).

14. H. M. van Horn, Astrophys. J. **151**, 227 (1968).

15. S. G. Brush, H. L. Sahlin, and E. Teller, J. Chem. Phys. **45**, 2102 (1966).

16. D. J. Stevenson and N. W. Ashcroft, Phys. Rev. A **9**, 782 (1974).

17. K. Inoue and T. Ariyasu, J. Phys. Soc. Jpn. **48**, 2179 (1980).

18. Yu. Kagan, V. V. Pushkarev, and A. Holas, Zh. Éksp. Teor. Fiz. **73**, 967 (1977) [Sov. Phys. JETP **46**, 511 (1977)].

19. F. Datchi, P. Loubeyre, and R. LeToullec, Phys. Rev. B **61**, 6535 (2000).

20. V. V. Kechin, J. Phys.: Condens. Matter **7**, 531 (1995); Phys. Rev. B **65**, 052102 (2002).

21. S. T. Weir, J. Phys.: Condens. Matter **10**, 11147 (1998).

22. A. Alavi, M. Parinello, and D. Frenkel, Science **269**, 1252 (1995).

23. O. Pfaffenzeller and D. Hohl, J. Phys.: Condens. Matter **9**, 11023 (1997).

24. F. A. Lindemann, Phys. Z. **11**, 609 (1910).

25. V. P. Trubitsyn, Fiz. Tverd. Tela (Leningrad) **8**, 862 (1966) [Sov. Phys. Solid State **8**, 688 (1966)].

26. A. A. Abrikosov, Zh. Éksp. Teor. Fiz. **39**, 1797 (1960) [Sov. Phys. JETP **12**, 1254 (1960)].

27. K. Ishizaki, I. L. Spain, and P. Bolsaitis, J. Chem. Phys. **63**, 1401 (1975).

28. S.-A. Cho, J. Phys. F: Met. Phys. **12**, 1069 (1982).

29. N. W. Ashcroft, in *Proceedings of the 19th AIRAPT–41st EHPRG International Conference on High Pressure Science and Technology (Bridgman Award)* (Bordeaux, France, 2003).

30. J. Oliva and N. W. Ashcroft, Phys. Rev. B **25**, 223 (1982).

31. J. E. Jaffe and N. W. Ashcroft, Phys. Rev. B **23**, 6176 (1981).

32. V. Diatschenko, C. W. Chu, D. H. Liebenberg, *et al.*, Phys. Rev. B **32**, 381 (1985).

33. E. Gregoryanz, A. F. Goncharov, K. Matsuishi, *et al.*, Phys. Rev. Lett. **90**, 175701 (2003).

34. S. Scandolo, Proc. Natl. Acad. Sci. USA **100**, 3051 (2003).

35. D. Hohl, V. Nataly, D. M. Ceperley, and R. M. Martin, Phys. Rev. Lett. **71**, 541 (1993).

36. C. Narayana, H. Luo, J. Orloff, and A. L. Ruoff, Nature **393**, 46 (1998).

37. P. Loubeyre, F. Occelli, and R. LeToullec, Nature **416**, 613 (2002).

38. I. I. Mazin, R. J. Hemley, A. F. Goncharov, *et al.*, Phys. Rev. Lett. **78**, 1066 (1997).

Translated by V. Sakun

Phonon–Plasmon Modes in a Strong Magnetic Field

L. A. Falkovsky

Landau Institute for Theoretical Physics, Russian Academy of Sciences, Moscow, 117940 Russia
Groupe d'Etudes des Semiconducteurs, cc074 UM2-CNRS 34095 Montpellier cedex5, France
Received November 27, 2003

Frequencies of phonon–plasmon coupled modes in a strong magnetic field were calculated. The calculations were performed in the long-wave approximation with regard to the electron damping and intrinsic lifetime of optical phonons. The dependence of the Raman scattering cross section on the carrier concentration and the magnetic field intensity was calculated. © 2004 MAIK "Nauka/Interperiodica".

PACS numbers: 63.20.Kr; 71.38.-k; 73.20.Mf

Coupled phonon–plasmon modes arise as a result of the interaction of optical phonons with charge carriers in semiconductors. These modes are observed, for example, in Raman scattering. Interest in these modes is associated not only with applications in optics but also with the possibility of elucidating certain principal questions in condensed-state physics, in particular, the possibility of determining the magnitude of electron–phonon interaction with their help. In this connection, noteworthy is the study [1] of phonon–plasmon modes in the presence of a magnetic field, which represents an additional free parameter along with the carrier concentration.

Consider estimates of the corresponding parameters of an electron–phonon system. The frequency of an emitted or absorbed optical phonon ω is usually equal to several hundred degrees; for example, it is 35 mV in GaAs. The magnetic field in which the cyclotron frequency of carriers is of the same order of magnitude must reach 20 T for an effective carrier mass of $0.063m_0$ in the same GaAs. If scattering is excited by the laser frequency $\omega_i = 1.5$ eV, the wave vector k of incident radiation equals $\omega_i/c \sim 10^5$ cm^{-1}. Then, the condition $\omega/c \ll k \ll \omega/v_F$ is fulfilled, where the Fermi velocity is $v_F \sim 0.5 \times 10^8$ cm/s in the case when the statistics of carriers is degenerate. The left-hand side of the above inequality means that the electric field associated with the phonon vibration is static, that is, longitudinal with respect to the wave vector $\mathbf{k}$. The right-hand side of the inequality allows the conductivity to be calculated using an expansion in terms of the parameter kv/ω, retaining at least the first-order correction, which proves to be important, because it has a resonant character.

Two circumstances should be noted. First, both the frequency of the coupled modes and the width of the corresponding resonance are of interest, for example, in Raman light scattering. Therefore, the contribution of carriers to the dielectric function must be calculated with regard to their damping. The spatial dispersion of the dielectric function in a magnetic field under these conditions has not been calculated so far. Second, in addition to the electrodynamic interaction of carriers with phonon vibrations, which is taken into account by the dielectric function, the deformation interaction exists which bears the name Fröhlich in theoretical works. It arises because of the nonadiabaticity of the electron–phonon system and leads to a certain (as small as the nonadiabaticity parameter) renormalization of phonon frequencies. In the absence of a magnetic field, this renormalization has been considered recently in [2–4], and it will not be taken into account here.

Consider the geometry when the magnetic-field effect is most important: the magnetic field $\mathbf{H}$ is directed along the z axis, whereas the wave vector $\mathbf{k}$ and the corresponding electric field $\mathbf{E}$ are directed in the perpendicular direction x. The dielectric function will be calculated using the kinetic equation in the τ approximation

$$-i(\omega - kv_x)f + \omega_c\frac{df}{d\varphi} = v_x = (f - \langle f \rangle)/\tau, \quad (1)$$

where the factor $eE\delta(\varepsilon - \varepsilon_F)$, which contains the charge, the electric field, and the Dirac function, is separated out of the distribution function f; ε is the energy variable; $\omega_c = eH/mc$ is the cyclotron frequency; and φ is the angle of rotation in the momentum space around the magnetic field, on which the velocity $\mathbf{v}$ depends. For a quadratic electron spectrum, it may be considered, for example, that $v_x = v_\perp(p_z)\sin\varphi$. Broken brackets designate averaging over the Fermi surface

$$\langle \ldots \rangle = \int(\ldots)mdp_z d\varphi \Big/ \int mdp_z d\varphi,$$

where the element of phase volume equals $md\varepsilon dp_z d\varphi$. Taking into account the term with averaging in the kinetic equation is necessary for the fulfillment of the conservation law for the electric current.

The transverse (with respect to the magnetic field) conductivity in the direction x equals

$$\sigma = e^2 \int v_x f m \frac{2 d\varphi d p_z}{(2\pi)^3}. \quad (2)$$

The solution to Eq. (1) will be expanded to the second order in terms of the parameter kv/ω $f = f_0 + f_1 + f_2$. Because $\langle v_x \rangle$ vanishes upon integration over φ, it is seen from Eq. (1) that $\langle f_0 \rangle = 0$. Therefore, the system of equations for $f_0, f_1,$ and f_2 takes the form

$$-i\omega^* f_0 + \omega_c \frac{df_0}{d\varphi} = v_x,$$

$$-i\omega^* f_j + \omega_c \frac{df_j}{d\varphi} = \frac{\langle f_j \rangle}{\tau} - ik v_x f_{j-1},$$

where $j = 1, 2$ and $\omega^* = \omega + i/\tau$. The zeroth- and first-order approximations are readily found

$$f_0 = \int_{-\infty}^{\varphi} v_x \exp[-i\omega^*(\varphi - \varphi')/\omega_c]$$

$$= \frac{-v_\perp}{2}[(\omega_c - \omega^*)^{-1} e^{i\varphi} + (\omega_c + \omega^*)^{-1} e^{-i\varphi}], \quad (3)$$

$$f_1 = \int_{-\infty}^{\varphi} (\langle f_1 \rangle/\tau) - ik v_x f_0) \exp[-i\omega^*(\varphi - \varphi')/\omega_c], \quad (4)$$

which are periodic in the angle φ. First, $\langle f_1 \rangle$ and, then, f_1 can be found by averaging both sides of the last equation. We get

$$f_1 = \frac{-ik v_\perp^2}{4(\omega_c^2 - \omega^{*2})} \left[\frac{4i}{3\omega\tau} + 2\frac{v_\perp^2}{v_0^2} \right.$$

$$\left. + \frac{(\omega_c + \omega^*) v_\perp^2}{(2\omega_c - \omega^*) v_F^2} e^{2i\varphi} + \frac{(\omega_c - \omega^*) v_\perp^2}{(2\omega_c + \omega^*) v_F^2} e^{-2i\varphi} \right]. \quad (5)$$

For the second-order approximation, an expression similar to f_1 (Eq. (4)) is obtained. The difference is connected with the fact that f_2 is an odd function of velocity, and, therefore, the mean value $\langle f_2 \rangle$ vanishes. It can be found that

$$f_2 = \frac{k^2 v_\perp v_F^2}{8(\omega_c^2 - \omega^{*2})}$$

$$\times \left[\left(\frac{4i}{3\omega\tau} + 2\frac{v_\perp^2}{v_0^2} \right) \left(\frac{e^{i\varphi}}{\omega_c - \omega^*} + \frac{e^{-i\varphi}}{\omega_c + \omega^*} \right) \right.$$

$$\left. + \frac{(\omega_c + \omega^*) v_\perp^2}{(2\omega_c - \omega^*) v_F^2} \left(\frac{e^{3i\varphi}}{3\omega_c - \omega^*} - \frac{e^{i\varphi}}{\omega_c - \omega^*} \right) \right. \quad (6)$$

$$\left. - \frac{(\omega_c - \omega^*) v_\perp^2}{(2\omega_c + \omega^*) v_F^2} \left(\frac{e^{-i\varphi}}{\omega_c + \omega^*} - \frac{e^{-3i\varphi}}{3\omega_c + \omega^*} \right) \right].$$

Because the first-order approximation f_1 (Eq. (5)) is even with respect to velocity, it makes no contribution to the conductivity. Using the zeroth- (Eq. (3)) and second-order (Eq. (6)) approximations, the contribution of carriers to the conductivity (Eq. (2)) and the dielectric function $4\pi i\sigma/\omega$ can be calculated. With regard to the lattice contribution, the dielectric function can be written as

$$\varepsilon(\omega, k) = \varepsilon_\infty \left\{ 1 - \frac{\omega_{pi}^2}{\omega^2 - i\omega\Gamma - \omega_{TO}^2} - \frac{\omega_{pe}^2 \omega^*}{\omega(\omega^{*2} - \omega_c^2)} \right.$$

$$\left. - \frac{3\omega_{pe}^2 \omega^* k^2 v_F^2}{5\omega(\omega^{*2} - \omega_c^2)^2} \left(1 + \frac{5i}{9\omega\tau} + \frac{3\omega_c^2}{\omega^{*2} - 4\omega_c^2} \right) \right\}, \quad (7)$$

where the plasma frequency of ions is determined by the relationship between the frequencies of the longitudinal and transverse modes $\omega_{LO}^2 = \omega_{TO}^2 + \omega_{pi}^2$. The equation obtained remains valid both in the absence of a magnetic field ($\omega_c = 0$) and in the collisionless limit ($\tau = \infty$). If both these conditions are fulfilled, Eq. (7) converts to the known expression with the true coefficient 3/5. This coefficient, as well as the others in Eq. (7), was calculated here for the quadratic electron spectrum; however, the dependence itself on the frequency ω, magnetic field, and damping is also retained in the general case.

The dielectric function of a nondegenerate electron plasma was obtained in [5]

$$\varepsilon(\omega, k) = 1 - \frac{\omega_{pe}^2 \omega^*}{\omega} \left[\frac{1 - \lambda}{\omega^{*2} - \omega_c^2} + \frac{\lambda}{\omega^{*2} - 4\omega_c^2} \right], \quad (8)$$

where $\lambda = (k v_{th}/\omega_c)^2$, and v_{th} is the thermal velocity of electrons. At $\tau = \infty$ and $\lambda = (k v_F/\omega_c)^2/5$, it coincides with the electronic term in Eq. (7).

The zeros of the dielectric function (7) determine the spectrum of longitudinal vibrations of the electron–phonon system in a magnetic field. With the neglect of electron τ^{-1} and phonon Γ damping, dielectric function (7) is real and the frequencies of the corresponding vibrations are also real. In order to determine these frequencies, one has to solve a cubic equation. Instead of doing that, one can first omit the small term with k^2 and obtain two eigenfrequencies $\omega_\pm$ by solving a quadratic equation. The third frequency lies in the vicinity of the pole $\omega = 2\omega_c$ of the omitted term. This is shown in a dash-and-dot line in Figs. 1 and 2.

Figures 3 and 4, in which the intensity of Raman scattering is depicted as a function of the frequency transfer for several values of the magnetic field and two carrier concentrations, are more informative. This func-
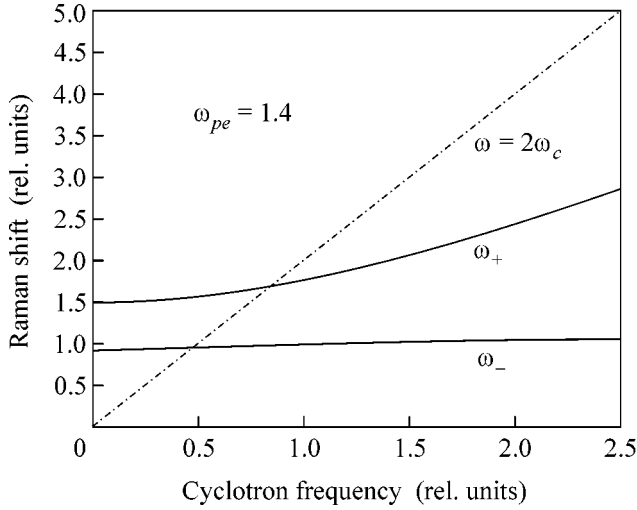
Fig. 1. Dependence of the frequencies (in the ω_{TO} units) of the phonon–plasmon coupled modes on the magnetic field (the cyclotron frequency is in the ω_{TO} units) for the carrier concentration $\omega_{pe} = 1.4$; the plasma frequency of carriers ω_{pe} is in the ω_{TO} units.

tion is the imaginary part of the generalized susceptibility

$$\chi(\omega, k) = \chi_e(\omega, k)$$

$$+ 4\pi g_E^2 \frac{\varepsilon_e(\omega, k) C^2 \omega_{TO}^4 / \varepsilon_\infty \omega_{pi}^2 - \Delta - 2C\omega_{TO}^2}{\varepsilon_e(\omega, k)\Delta + \varepsilon_\infty \omega_{pi}^2} \quad (9)$$
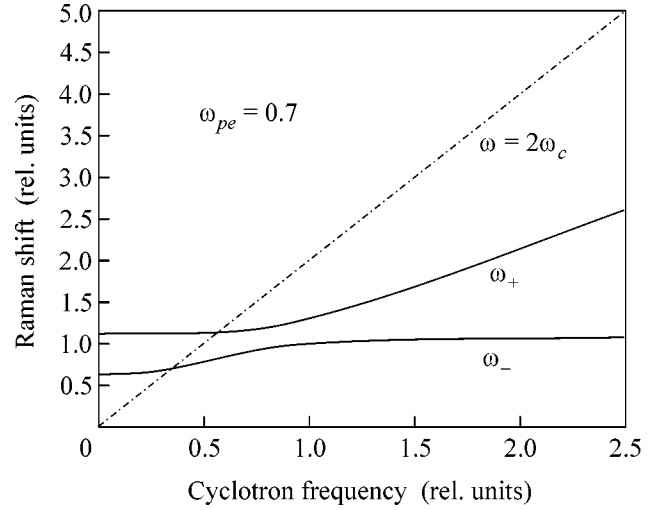
obtained in [6] for the case of a zero magnetic field; $\varepsilon_e(\omega, k)$ is the dielectric function without the lattice contribution, and $\Delta = \omega_{TO}^2 - \omega^2 - i\omega\Gamma$. All the difference here is only in the expression for the dielectric function, which is given now by Eq. (7). In Eq. (9), g_E is the electrooptic constant in Raman scattering and C is the Faust–Henry coefficient, which is commonly taken equal to $C = -0.5$ in the case of comparison with experiment in the absence of a magnetic field. It is natural that the poles of the second term in Eq. (9) coincide with the zeros of the dielectric function (7).

The first term in Eq. (9), which corresponds to the contribution to scattering due to the excitation of electron–hole pairs, is not taken into account in the figures. It was calculated in [7] and, at $k = 0$, was found to be

$$\chi_e(\omega, 0) = -\nu \sum_n \left\langle \frac{\omega |\gamma^{(n)}|^2}{\omega - n\omega_c + i/\tau} \right\rangle, \quad (10)$$

where $\gamma^{(n)}$ is the Fourier component (with respect to the angle φ) of the electron-optic constant in Raman scattering and ν is the electron density of states.

The electron–hole contribution given by Eq. (10), as well as the dielectric function (7), has singularities at cyclotron and multiple frequencies. An essential difference is in the fact that the second term in Eq. (9)
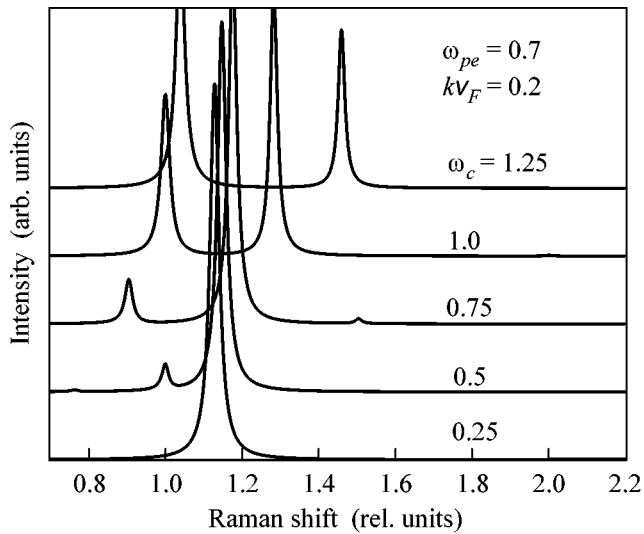
depends only on the frequency transfer ω, while the electron–hole contribution (10) depends via $\gamma^{(n)}$ on the frequencies of incident and scattered light separately (resonant scattering). Moreover, the cyclotron resonances in the second term strongly interfere with the phonon singularities at ω_{TO} or ω_{LO}. Actually, it is seen in Fig. 3 how the weak resonance at $\omega = 2\omega_c$ and the phonon peak at $\omega = \omega_{TO}$ are "pushed apart" in the case when they turn out to be close, see the curve for $\omega_c = 0.5$. The same figure (see, also, Fig. 1) clearly demonstrates the result of screening in the case of a relatively

Fig. 2. The same as in Fig. 1 but for $\omega_{pe} = 0.7$.
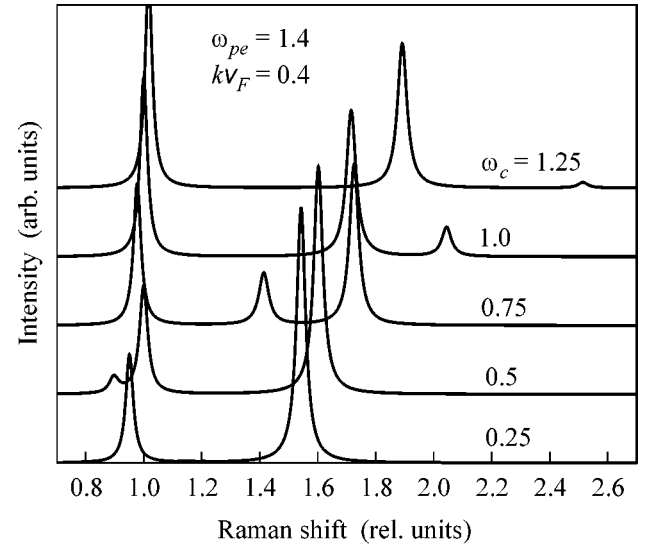
Fig. 3. Calculated Raman spectra for the carrier concentration, momentum transfer, and cyclotron frequency indicated in the figure. All the frequencies and kv_F are in the ω_{TO} units; the phonon width $\Gamma = 3 \times 10^{-2} \omega_{TO}$, the carrier relaxation rate $\tau^{-1} = 2 \times 10^{-2} \omega_{TO}$, and the plasma frequency of ions $\omega_{pi} = 0.4\omega_{TO}$.

The case of a relatively small carrier concentration is illustrated by Figs. 2 and 4. It is seen in Fig. 4 that, in a weak field ($\omega_c = 0.25$), the frequency of the longitudinal mode is close (as it must be) to $\omega_{LO} = 1.1\omega_{TO}$. Besides the weak resonance at $\omega = 2\omega_c$, a phonon–plasmon crossover is seen in the curves for $\omega_c = 0.75$ and 1.0: as the magnetic field increases, the weaker plasmon peak, after passing through the phonon one, becomes more intense.

REFERENCES

1. A. Wysmolek, M. Potemski, and T. Slupinski, Physica B (Amsterdam) **298**, 216 (2001).
2. A. S. Alexandrov and J. R. Schrieffer, Phys. Rev. B **56**, 13731 (1997).
3. M. Reiser, Phys. Rev. B **61**, 40 (2000).
4. L. A. Falkovsky, Phys. Rev. B **66**, 020302 (2002).
5. P. M. Platzman, P. A. Wolf, and N. Tzoar, Phys. Rev. **174**, 489 (1968).
6. L. A. Falkovsky, Zh. Éksp. Teor. Fiz. **124**, 886 (2003) [JETP **97**, 794 (2003)].
7. E. G. Mishchenko, Phys. Rev. B **53**, 2083 (1996).

Translated by A. Bagatur'yants

$\omega_{pe} = 0.7$
$kv_F = 0.2$

$\omega_c = 1.25$

1.0

0.75

0.5

0.25

Fig. 4. The same as in Fig. 3 but for $\tau^{-1} = 10^{-2}\,\omega_{TO}$.

high concentration of carriers: the frequency ω_-, which equals the frequency of the longitudinal mode in the absence of carriers (at the particular choice of parameters, $\omega_{LO} = 1.1\omega_{TO}$), turns out to be close to the frequency of the transverse mode ω_{TO}.

Collective Excitations in Double Quantum Wells with Strong Tunnel Coupling

S. V. Tovstonog[1, 2, *], L. V. Kulik[1, 2], V. E. Kirpichev[1], I. V. Kukushkin[1, 2],
W. Dietsche[2], and K. von Klitzing[2]

[1] *Institute of Solid-State Physics, Russian Academy of Sciences, Chernogolovka, Moscow region, 142432 Russia*
[2] *Max-Planck-Institut für Festkörperforschung, 70569 Stuttgart, Germany*
*e-mail: tovstons@issp.ac.ru

Received December 2, 2003

Spectra of collective and magnetic excitations in symmetric double quantum wells with strong tunnel coupling were studied by inelastic scattering. Gaps in the spectrum of collective and single-particle excitations associated with tunnel interwell splitting were measured. New excitation modes, namely, tunnel Bernstein modes, were detected in a magnetic field. Based on the dispersion and magnetic-field dependences of the energies of inelastic light scattering lines, a classification of excitations and magnetic excitations was given. © *2004 MAIK "Nauka/Interperiodica".*

PACS numbers: 73.21.Fg, 75.75.+a; 78.67.De

By physical properties, symmetrically doped double quantum wells (DQWs) can be divided into two groups: DQWs with Coulomb coupling and DQWs with tunnel coupling between the wells. DQWs with Coulomb coupling are primarily objects of basic research, because Coulomb correlations between electrons of different wells can lead to such physical phenomena as superconductivity [1] and Wigner crystallization [2]. In turn, double quantum wells with tunnel coupling are of considerable interest to technical applications. At the moment, it is DQWs with spatially modulated tunnel coupling that are probable candidates for creating basic elements of quantum computing—qubits and quantum logic gates—integrated into standard electronic circuits. An electron wave packet of such a circuit is injected into one of the quantum wells in the weak-coupling state and propagates into the region with strong tunnel coupling, where the electron density is redistributed between the wells, after which the packet passes again into the region of weak coupling and is detected. By varying the number and distribution of surface gates to the DQW, one can in principle organize any quantum computing [3]. However, the main problem of the experimental implementation of such quantum circuits is the dephasing of the electron wave packet in the course of quantum computing. Improving the growth technology of double quantum wells has led to the fact that the channels of scattering by impurities and heterogeneities of the structure make no significant contribution to dephasing. Nevertheless, there exists a principally irremovable dephasing channel, namely, electron–electron scattering. The probability of electron–electron scattering is determined by the excitation spectrum in the DQW, which can be effectively changed by an external quantizing magnetic field. In this work, the spectrum of collective excitations in symmetric double quantum wells with strong tunnel coupling and its modification in a transverse magnetic field were studied by inelastic light scattering.

Inelastic light scattering (ILS) spectra were measured using a tunable Ti–sapphire laser with a photon energy of 1.545–1.570 eV and the characteristic power density $W = 0.1$–1 W/cm^2. The measurements were performed in a cryostat with a superconducting solenoid at a temperature of 4.2 K in the back-scattering geometry. A triple monochromator in combination with a semiconductor detector with charge coupling served as the spectral instrument, which provided a spectral resolution of 0.02 meV. The quasi-momentum of excitations (in a magnetic field, pseudomomentum [4]) was determined by the difference in the momenta of the pumping and scattered photons, which were specified by the mutual configuration of the directions of the exciting radiation and the scattered ILS signal with respect to the normal to the sample surface. By varying the experimental configuration, the quasi-momentum (pseudomomentum) of excitations can be varied in the range from 0 to 1.5×10^5 cm^{-1}. Some measurements were carried out in an optical cryostat.

The studies were carried out with two high-quality heterostructures grown by molecular-beam epitaxy (MBE). Each of the heterostructures consisted of two symmetrically doped $Al_{0.3}Ga_{0.7}As/GaAs/Al_{0.3}Ga_{0.7}As$ quantum wells 120 Å in width separated by a narrow potential barrier 25 Å in width (Fig. 1). In spite of the

fact the total electron concentrations and mobilities in the two structures were approximately equal (3.3×10^{11} cm^{-2} and $\sim 6 \times 10^5$ cm^2 V^{-1} s^{-1}), their ILS spectra were different. This was primarily due to the specific features of the growth of heterostructures with narrow (~ 100 Å) quantum wells. Fluctuations of one monolayer in the well and barrier thicknesses allowable in the growth led to a noticeable change in the band structure and, as a consequence, to a change in the energy spectrum of the input and output resonances for inelastic light scattering. Therefore, the experimental spectra obtained from the two structures differed in the energies and intensities of the ILS lines. The lines less intense in the spectra of one structure can be more intense in the spectra of the other. The total intensity of the ILS signal from the narrow quantum wells was on the threshold of the sensitivity of the experimental system (a small effective optical path for narrow quantum wells), and even a small gain in the intensity of particular lines substantially simplified their study. The majority of the results presented in this paper were obtained with one structure; in the case when the results for the second heterostructure were used, this is specially indicated.

The energy parameters of the DQW—the tunnel gap and the Fermi energy of electrons—were determined by the spectroscopic method developed in [5]. Resonances associated with single-particle excitations from the Fermi level of electrons in the lower tunnel subband to the upper one are observed in the ILS spectra of double quantum wells with tunnel coupling (SPE$_1$ and SPE$_2$ lines, Fig. 2a). At a zero quasi-momentum, the energy levels of all such excitations are degenerate and equal to the tunnel gap (Δ_{SAS}). With increasing quasi-momentum, the energies of excitations from the electron states with the Fermi quasi-momentum parallel (antiparallel) to the quasi-momentum of excitations increase (decrease); this is demonstrated by the schematic diagram in Fig. 1a (transitions 0–1 and 0–2) and in Fig. 2. The slope of the dependences of the resonance energies of single-particle excitations on the transferred momentum gives the Fermi velocity of electrons in the lower tunnel subband (v_F). Taking into account that tunnel-coupled quantum wells possess a common Fermi level, one can find electron concentrations in each of the tunnel subbands (n_1 and n_2)

$$n_1 = \frac{(m^* v_F)^2}{2\pi\hbar^2}, \quad n_2 = n_1 - \frac{m^*\Delta_{SAS}}{\pi\hbar^2}, \qquad (1)$$

where m^* is the effective electron mass in GaAs. The electron concentrations were found to be 2×10^{11} cm^{-2} and 1.3×10^{11} cm^{-2} in the lower and upper tunnel subbands, respectively.

Besides the lines of tunnel single-particle excitations, two additional spectral features (TCDE and ISPE lines) are observed in the ILS spectrum. In order to
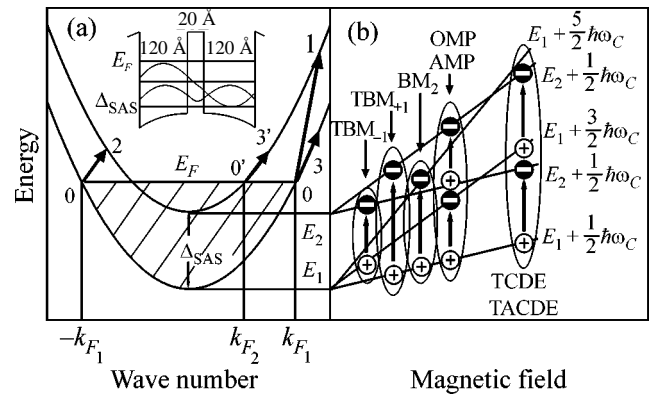
Fig. 1. (a) Illustration of the spectrum of electrons in the two tunnel subbands of a double quantum wells. The arrows indicate single-particle intraband and tunnel excitations with the quasi-momentum k. The inset shows the potential profile of the quantum well and wave functions in the tunnel subbands. (b) Schematic diagram of possible collective excitations in a double quantum well with tunnel coupling in a magnetic field. The designations are explained in the text.
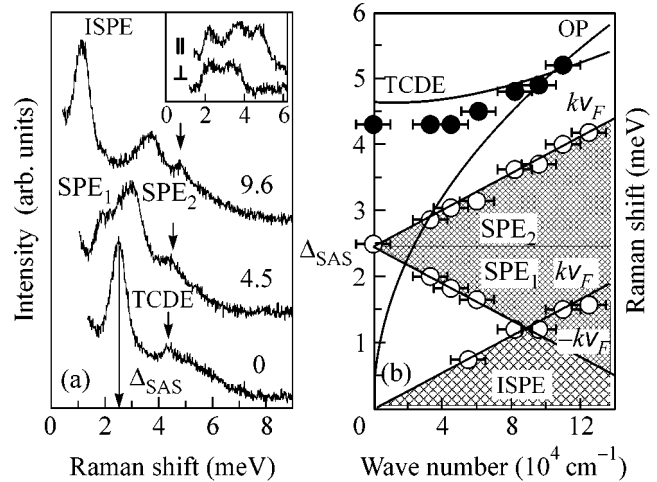
Fig. 2. (a) Inelastic light scattering spectra of the first heterostructure under study at various transferred momenta. The inset shows spectra measured in two configurations of polarizers for the second structure at $k = 5.5 \times 10^4$ cm^{-1}. (b) Dependence of the energies of ILS lines on the transferred momentum. Light dots correspond to unpolarized lines; black dots indicate the ILS line observed only in the parallel polarization configuration. Solid lines correspond to the energies of collective excitations calculated in the RPA approximation. The optical plasmon (OP) is slightly active in inelastic light scattering spectra, see, for example, [17]. Hatched regions indicate the energies of single-particle excitations.

determine the nature of these lines, the ILS spectra were recorded in two different polarization configurations of the pumping and scattered radiation. The polar-

ization planes were parallel in one configuration and perpendicular in the other. The ILS signals from electron excitations of different types (excitations of the charge and spin densities) were detected in the parallel and perpendicular configurations, respectively [6]. The ISPE line was observed in both polarization configurations; therefore, we associated it with single-particle excitations inside one tunnel subband represented by transitions 0–3 and 0–3' in the schematic diagram in Fig. 1a (the energies of single-particle excitations with and without spin flip are equal to each other). The dependence of the energy of the ISPE line on the transferred momentum is described sufficiently well by the dispersion of the boundary energy of the single-particle continuum kv_F, where k is the momentum passed to the electron system in the process of inelastic light scattering (transferred momentum).

Unlike the ISPE line, the TCDE line is observed only in the parallel configuration (Fig. 2), and its dispersion is of the gap type. This allows the TCDE line to be associated with a collective excitation of the charge density, namely, with a tunnel plasmon [7]. The energy of the tunnel plasmon at $k = 0$ can be obtained analytically within the random phase approximation (RPA) [8]

$$\omega^2 = \Delta_{SAS}^2 + \frac{2\sqrt{2\pi}e^2 L}{\epsilon}(n_1 - n_2)\Delta_{SAS}, \qquad (2)$$

where L is the parameter characterizing the nonlocality of the wave function of electrons in the growth direction of the heterostructure. The second term in Eq. (2) is called depolarization shift and is determined by the effects of the dynamic screening of an excited electron by the electron system. Substituting in Eq. (2) the quantum-well width for L, we obtain 4.3 meV. This virtually coincides with the TCDE line energy at $k = 0$. The complete calculation of the dispersion of collective excitations within the RPA is shown in Fig. 2b. The electron wave functions in the growth direction and the tunneling subband energies were found as the self-consistent solutions to the Schrödingen and Poisson equations. The widths of the barrier and quantum wells were varied within the limits of the technological errors of the MBE growth in such a way that the equality of the calculated and experimental tunnel gaps would be guaranteed.

The characteristic feature of both the experimental data and the theoretical calculation is that the gapless mode with linear dispersion, that is, the acoustic plasmon, which represents an antiphase oscillation of the charge density localized in the two quantum wells [9], is absent in the excitation spectrum. Because the well number is a bad quantum number in double wells with tunnel coupling, it is more appropriate to speak about the acoustic phonon as an antiphase oscillation of the electron density in the two tunnel subbands. Such plasma excitations were discussed theoretically for single quantum wells with two occupied dimensional-

quantization subbands [10, 11]. The principle difference of symmetric DQWs with tunnel coupling from single quantum wells is in the fact that the electron density is distributed uniformly in the two tunnel subbands (the squares of the wave functions virtually coincide, Fig. 1). Note that the energy of the acoustic plasmon is determined by the difference in the Coulomb interaction of electrons located in one and in different tunnel subbands. For symmetric DQWs, this difference is small; therefore, the acoustic plasmon mode softens and falls into the continuum of single-particle excitations.

In a magnetic field oriented along the heterostructure growth direction, the energy spectrum of each tunnel subband is divided into a series of discrete Landau levels. In this case, the spectrum of neutral excitations changes qualitatively. The continua of the intraband and the tunnel single-particle excitations are split into a number of spectral components, among which groups of lines with energies multiple of cyclotron frequencies ($\hbar\omega_C$, where $\omega_C = eB/m^*$) can be distinguished. Two such groups are observed in the spectrum. The energies in these groups at $B \longrightarrow 0$ either (1) tend to zero (BM_2) or (2) equal the tunnel gap (TBM_{+2}, TBM_{+1}, TBM_{-1}, and TBM_{-2}). The first group consists of Bernstein modes, that is, collective excitations composed of excited electrons on empty Landau levels and holes in occupied Landau levels in one tunnel subband. These excitations differ from each other by the difference in the Landau level numbers of excited electrons and holes (Δn), and $\Delta n \geq 2$ [12, 13]. The second group represents a new type of excitations associated with electron transitions accompanied by a simultaneous change in the indices of the tunnel subband and the Landau level. In the subsequent discussion, these excitations will be referred to as tunnel excitations in order to distinguish them from the other types of Bernstein modes [14]. The energies of the tunnel Bernstein modes in the region of magnetic fields under study can be described to a good accuracy by the dependence of the form
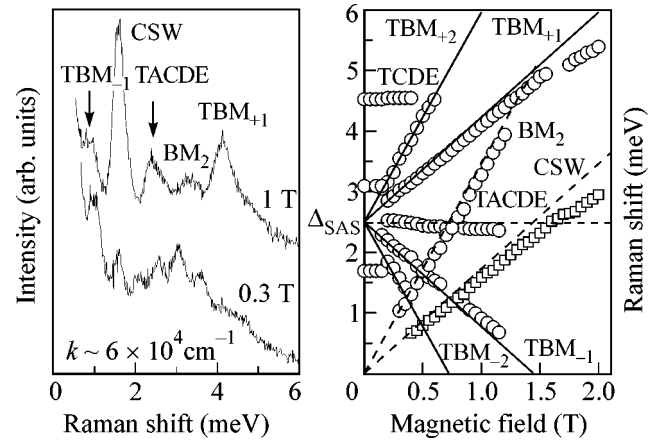
$$E_{B_{\pm n}} = |\Delta_{SAS} \pm \Delta n \hbar \omega_C|, \qquad (3)$$

where $\Delta n \geq 1$. Unlike the usual Bernstein modes, the energies of tunnel Bernstein modes can either increase or decrease in a magnetic field. This corresponds to electron transitions with an increase or a decrease in the Landau level number (Fig. 3 and the schematic diagram in Fig. 1). In a finite magnetic field, a situation when the energy of one of the tunnel Bernstein modes equals zero can be accomplished. In this field, the energies of the two upper occupied Landau levels of the two tunnel subbands are degenerate, which can lead to the decay of the quantum Hall effect states in the DQW.

Another class of collective magnetic excitations is associated with electron transitions that are accompanied by the retention of the Landau level number and a change in the index of the tunnel subband. The energies

of such transitions are independent of the magnetic field strength; therefore, we assign the TCDE and TACDE lines (Fig. 3) to this class. The TCDE line corresponds to in-phase transitions of electrons from occupied Landau levels of the lower tunnel subband to empty or partially occupied Landau levels of the upper subband. The energy of the TCDE mode is determined by the tunnel gap and the depolarization shift, whereas it is expressed by Eq. (2) at a zero pseudomomentum. The TACDE line corresponds to antiphase electron excitations from the lower tunnel subband to the upper one. The energy of such excitations does not include the depolarization shift, and their energy tends to the tunnel gap at $B \longrightarrow 0$. Lines similar to TCDE and TACDE were observed previously in the spectrum of intersubband excitations of single quantum wells in which electrons occupied one dimensional-quantization subband [6, 15]. In a sense, these excitations are similar to the acoustic and the optical phonons in crystals. Here, the magnetic flux quantum corresponds to the unit cell, and the occupation factor (ν) corresponds to the number of atoms in the unit cell. In a single quantum well, the natural restriction on the domain of existence of excitations of the optical type was the condition $\nu > 2$, that is, the occupation of more than one Landau level of electrons. In double quantum wells, both the tunnel subbands are occupied by electrons; therefore, the condition $\Delta\nu > 2$ is the restriction on the domain of existence of excitations of the optical type in this case, where $\Delta\nu$ is the difference in the occupation factors of the lower and upper tunnel subbands. It is evident that this condition cannot be fulfilled at $\hbar\omega_C > \Delta_{SAS}$; this is in agreement with the experimental results (Fig. 3).

In Fig. 3, it is seen that the ILS spectra of the quantum wells under study contain a line with an energy of $\hbar\omega_C$ (CSW). This line is predominant in the region of low magnetic fields. Such a line was observed in the ILS spectra of single and double quantum wells without tunnel coupling and was associated with excitations of the spin rather than charge density, namely, a cyclotron spin wave [16]. However, the intensity of the cyclotron-spin-wave line was considerably lower than that in the DQWs under study. It may be suggested that the ILS line of the cyclotron spin wave coincides in our case with an intense line of an unknown charge-density excitation. This excitation can correspond to the acoustic plasmon. There is an analogy between spin waves in two-dimensional systems and the acoustic plasmon in symmetric double quantum wells with tunnel coupling. In the absence of a magnetic field, both modes are gapless and their energies fall into the continuum of single-particle excitations. The discretization of the electron spectrum by a magnetic field leads to the stabilization of spin waves. It may be suggested that an analogous effect also arises for the acoustic plasmon. Because the energy of the acoustic plasmon (AP) in the absence of a magnetic field is small, the energy of the hybrid magnetoacoustic plasmon (MAP) in a magnetic field only slightly differs from the cyclotron energy [17]

$$\hbar\omega_{MAP} = \sqrt{(\hbar\omega_{AP})^2 + (\hbar\omega_C)^2} \approx \hbar\omega_C. \quad (4)$$

Fig. 3. (a) Inelastic light scattering spectra at $k = 6 \times 10^4$ cm^{-1} for two values of the magnetic field, $B = 0.3$ T and $B = 1$ T. (b) Magnetic-field dependence of the energies of ILS lines. Solid lines correspond to the dependence of $|\hbar\Delta_{SAS} \pm n\hbar\omega_C|$, dotted lines correspond to $n\hbar\omega_C$, and dash-and-dot lines correspond to $\hbar\Delta_{SAS}$.

REFERENCES

1. P. M. Plazman and T. Lenosky, Phys. Rev. B **52**, 10327 (1995).
2. H. C. A. Oji, A. H. MacDonald, and S. M. Girvin, Phys. Rev. Lett. **58**, 824 (1987).
3. A. Bertoni, P. Bordone, R. Brunetti, *et al.*, Phys. Rev. Lett. **84**, 5912 (2000).
4. C. Kallin and B. I. Halperin, Phys. Rev. B **30**, 5655 (1984).
5. S. V. Tovstonog, L. V. Kulik, V. E. Kirpichev, *et al.*, JETP Lett. **78**, 654 (2003).
6. A. Pinczuk, S. Schmitt-Rink, G. Danan, *et al.*, Phys. Rev. Lett. **63**, 1633 (1989); G. Abstreiter, R. Merlin, and A. Pinczuk, IEEE J. Quantum Electron. **22**, 1771 (1986).
7. R. Decca, A. Pinczuk, S. Das Sarma, *et al.*, Phys. Rev. Lett. **72**, 1506 (1994).
8. R. Z. Vitlina and A. V. Chaplik, Sov. Phys. JETP **54**, 536 (1981).
9. Acoustic plasmon is always present in the excitation spectra of symmetrical double quantum wells with a Coulomb relation, see, for example, D. S. Kainth, D. Richards, A. S. Bhatti, *et al.*, Phys. Rev. B **59**, 2095 (1999); S. V. Tovstonog, I. V. Kukushkin, L. V. Kulik, and V. E. Kirpichev, JETP Lett. **76**, 511 (2002).

10. J. K. Jain and S. Das Sarma, Phys. Rev. B **36**, 5949 (1987).

11. C.-M. Hu, C. Schüller, and D. Heitmann, Phys. Rev. B **64**, 073303 (2001).

12. E. Batke, D. Heitmann, J. P. Kotthaus, and K. Ploog, Phys. Rev. Lett. **54**, 2367 (1985).

13. L. Wendler and R. Pechstedt, J. Phys.: Condens. Matter **2**, 8881 (1990).

14. V. E. Kirpichev, L. V. Kulik, I. V. Kukushkin, *et al.*, Phys. Rev. B **59**, R12751 (1999).

15. L. V. Kulik, I. V. Kukushkin, V. E. Kirpichev, *et al.*, Phys. Rev. Lett. **86**, 1837 (2001).

16. L. V. Kulik, I. V. Kukushkin, V. E. Kirpichev, *et al.*, Phys. Rev. B **63**, 201402(R) (2001); L. V. Kulik, I. V. Kukushkin, V. E. Kirpichev, *et al.*, Pis'ma Zh. Éksp. Teor. Fiz. **74**, 300 (2001) [JETP Lett. **74**, 270 (2001)].

17. S. V. Tovstonog, L. V. Kulik, I. V. Kukushkin, *et al.*, Phys. Rev. B **66**, 241308 (2002).

Translated by A. Bagatur'yants

Quantum Magnetostriction Oscillations in a Two-Dimensional Antiferromagnet with Spin–Phonon Interaction in a Magnetic Field

S. S. Aplesnin

Kirenskiĭ Institute of Physics, Siberian Division, Russian Academy of Sciences,
Akademgorodok, Krasnoyarsk, 660036 Russia
e-mail: apl@iph.krasn.ru
Received December 8, 2003

The ground state of a two-dimensional antiferromagnet with $S = 1/2$ interacting with acoustic phonons in a magnetic field was studied by the quantum Monte Carlo method in the nonadiabatic approximation. Oscillations of the amplitude of the root-mean-square displacement of ions and the average phonon occupation number in a magnetic field were found. Local maxima were revealed in the distribution functions of site magnetic moments and ion displacements. The saturation magnetization was calculated as a function of the spin–phonon coupling constant. © 2004 MAIK "Nauka/Interperiodica".

PACS numbers: 75.10.Jm; 75.30.Cr; 75.80.+q

Phase separation in manganites and the formation of strips in undoped cuprate superconductors are bright effects in condensed state physics. Such effects associated with strip structures are also observed in the spin system with four-spin interaction on a square lattice [1]. The model with four-spin interaction is a particular case of a more general model of spin interaction with acoustic phonons.

Additional incommensurable maxima in the magnetic and nuclear structural factors were calculated for a ferromagnet with spin–phonon interaction on a square lattice [2]. Several maxima were also found in the density of states of bound spin–phonon quasiparticles. Under the action of an external magnetic field, the bound state of spins and phonons decays, resulting in an increase in the average number of phonons. This communication is devoted to the determination of the behavior of the amplitude of the root-mean-square displacement of ions in a magnetic field and the saturation magnetization, which has the constant value $m_s = 1$ for systems with spin–phonon interaction within the adiabatic approximation [3, 4].

Consider the ground state of a quasi-two-dimensional magnet with the interplane exchange interaction that is several orders of magnitude smaller than the intraplane exchange interaction. Therefore, the consideration will be restricted to the spin interaction between the nearest neighbors and with the acoustic modes of in-plane lattice vibrations. The Hamiltonian for a bound spin–phonon system in the harmonic approximation takes the form

$$H = \sum_{i,j} [J + \alpha(u_{i,j} - u_{i+1,j})]$$

$$\times [S_{i,j}^z S_{i+1,j}^z + (S_{i,j}^+ S_{i+1,j}^- + S_{i,j}^- S_{i+1,j}^+)/2] + H_i S_i^z$$

$$+ [J + \alpha(u_{i,j} - u_{i,j+1})] \quad (1)$$

$$\times [S_{i,j}^z S_{i,j+1}^z + (S_{i,j}^+ S_{i,j+1}^- + S_{i,j}^- S_{i,j+1}^+)/2] + M\dot{u}_{i,j}^2/2$$

$$+ K(u_{i,j} - u_{i+1,j})^2/2 + K(u_{i,j} - u_{i,j+1})^2/2,$$

where $S^{z,\pm}$ are the components of the spin operator $S = 1/2$ on a lattice site, $u_{i,j}$ is the ion displacement along the lattice translation vectors, M is the ion mass, and K is the elastic lattice constant; $J > 0$. Using the canonical transformation

$$\hat{u}_{\mathbf{r}} = \frac{1}{\sqrt{N}} \sum_{\mathbf{q}} \sqrt{\frac{\hbar}{2M\Omega(\mathbf{q})}} (b_{\mathbf{q}} + b_{-\mathbf{q}}^+) \exp(i\mathbf{q}\mathbf{r}), \quad (2)$$

the variables $u_{i,j}$ will be converted to the phonon creation and annihilation operators b^+ and b with the momenta $q_\beta = 2\pi n/L$, $n = 1, 2, \ldots, L$; $\beta = x, y$; and the lattice constant $a = 1$. The transformed Hamiltonian has the form

$$H = \sum_{i,j} (J_{i,j} \mathbf{S}_i \mathbf{S}_j + H_i S_i^z)$$
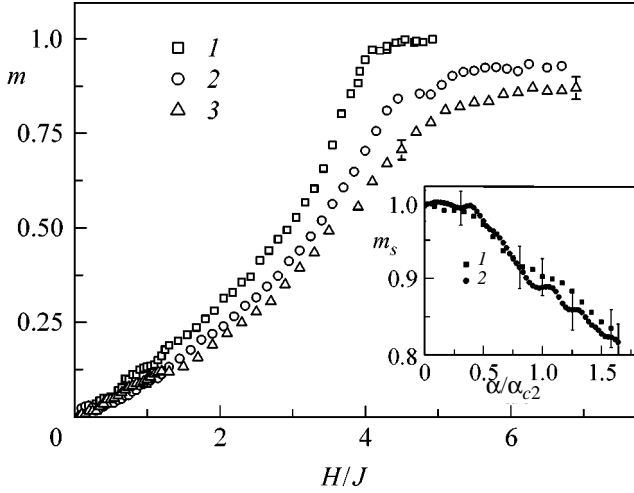
Fig. 1. Field dependence of the magnetization in an AFM and in a spin liquid for $\omega_0 = J$ and $\alpha/\alpha_{c2} = (1)$ 0, (2) 1, and (3) 1.5. The inset displays the dependence of the saturation magnetization on the normalized spin–phonon coupling constant for $\omega_0/J = (1)$ 1 and (2) 6.

$$+ \sum_{q_x, q_y, n, m} \alpha \sqrt{\frac{\hbar}{2M\Omega(\mathbf{q})}} \exp(i\mathbf{q}\mathbf{r})(b_\mathbf{q} + b^+_{-\mathbf{q}})$$

$$\times [(1 - \cos q_x - i\sin q_x)\mathbf{S}_{n,m}\mathbf{S}_{n+1,m} \qquad (3)$$

$$+ (1 - \cos q_y - i\sin q_y)\mathbf{S}_{n,m}\mathbf{S}_{n,m+1}] + \sum_\mathbf{q} \hbar\Omega(\mathbf{q})b^+_\mathbf{q}b_\mathbf{q},$$

$$\Omega(\mathbf{q}) = \omega_0\sqrt{2 - \cos(q_x) - \cos(q_y)}; \quad \omega_0 = \sqrt{\frac{2K}{M}}.$$

The calculations involve the spin–phonon coupling constant α normalized to the exchange interaction and the distance r normalized to the lattice constant. As the computational method, a quantum Monte Carlo method was selected. The method combined the worldline algorithm and the continuous time algorithm [5] on a plane with the size $N = 32 \times 32$ with periodic boundary conditions at the temperature $\beta = J/T = 10$. The computational method was described in detail in [2].

The root-mean-square displacement of an ion is determined as

$$\langle u^2 \rangle = \frac{\hbar}{2MN} \sum_q \frac{2n_q + 1}{\Omega(q)}.$$

In the ground state of a harmonic oscillator with $\alpha \longrightarrow 0$, the number of phonons equals zero. Therefore, it is important to calculate the variation of zero-point vibrations due to the action of the magnetic system on the
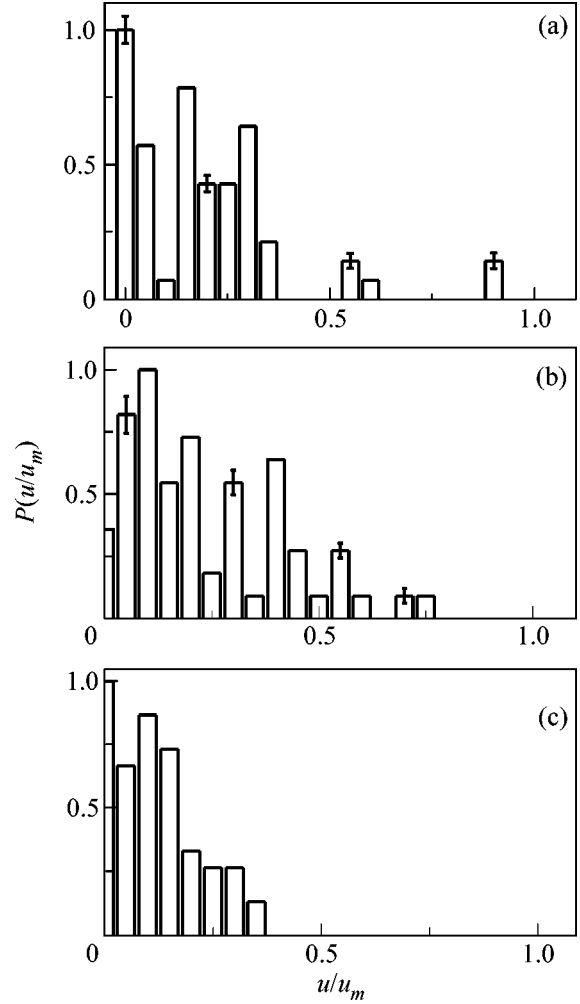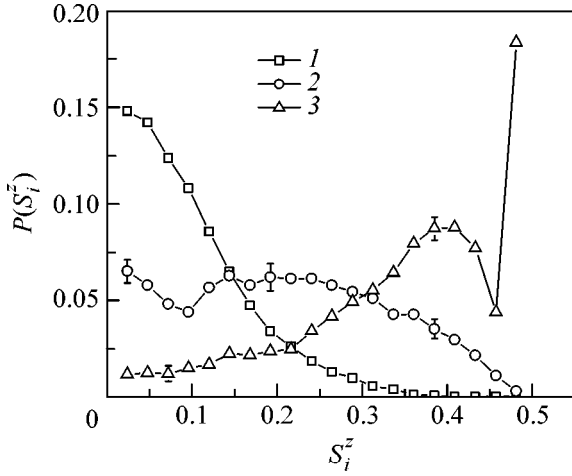

Fig. 2. Distribution functions of site ion displacements normalized to the maximum displacement u_m at $H = 0$ for $\omega_0 = J$, $\alpha/\alpha_{c2} = 1$, and $H/J = $ (a) 0.5, (b) 2, and (c) 5.

elastic subsystem; that is, $\langle U_n^2 \rangle = \langle u^2(\alpha) \rangle - \langle u^2(\alpha = 0) \rangle$. Below, the normalized value

$$\langle U^2 \rangle = \sum_r \langle U_n^2(r) \rangle / \frac{\hbar}{2NM\omega_0}$$

will be used.

In this work, two characteristic cases of the interaction of the spin and elastic subsystems are considered. These are the case when the threshold of the band of magnon excitations W_{tm} exceeds the threshold of the band of phonon excitations W_{tph}, which corresponds to the crossing of the dispersion curves of magnons and phonons, for example, at $\omega_0/J = 1$, and the opposite case when $W_{tph} > W_{tm}$ for $\omega_0/J = 6$. Typical dependences of the magnetization on the external magnetic field are presented in Fig. 1 for the magnetically ordered state and the magnetically disordered singlet state. The critical field of magnetic saturation for an antiferromagnet

Fig. 3. Distribution functions of site magnetic moments for $\omega_0 = J$, $\alpha/\alpha_{c2} = 1$, and $H/J = $ (*1*) 0.5, (*2*) 3, and (*3*) 5.

(AFM) is in good agreement with the known result $H_c = 2zSJ$. If the spin–phonon coupling parameter exceeds the critical value α_{c1}, at which the isotropy of spin–spin correlation functions becomes broken [2], the saturation field increases and the saturation magnetization m_s decreases. The corresponding values of m_s determined in the range of fields $H_c < H < 2H_c$ are displayed in the inset in Fig. 1. Here, the spin–phonon coupling parameters are normalized to the critical value α_{c2}, at which the long order disappears and a quantum spin liquid is formed. In the region of low fields, the magnetization grows linearly with increasing field even in the spin liquid state but with a smaller slope of $m(H)$. This dependence qualitatively differs from the dependence of the magnetization in the spin liquid with dimer ordering, for which $m(H) \longrightarrow 0$ at $H < \Delta$, where Δ is the energy gap in the spectrum of triplet excitations [6].

The elastic stresses induced by the spin subsystem have a hierarchical structure. The distribution function of ion displacements depicted in Fig. 2a exhibits several local maxima. In the region of local stresses, spins form singlet states. The existence of states is confirmed by the distribution function of the site magnetic moment $P(S^z \longrightarrow 0) \neq 0$ (Fig. 3) and by the calculation of the four-spin correlation function of parallel spin pairs

$$R(r) = \langle (\sigma_i + \sigma_{i+1}) S_i^z S_{i+1}^z$$
$$\times (\sigma_{i+r} + \sigma_{i+r+1}) S_{i+r}^z S_{i+r+1}^z \rangle, \qquad (4)$$
$$\sigma_i = \mathrm{sgn}(S_i^z).$$

The minima in the distance dependence of the four-spin correlation function presented in Fig. 4 correspond to the characteristic distance between the square-lattice sites with either zero values of the magnetic moment or an antiparallel arrangement of spins on the sites. Two such distances are observed in a magnetic field $H < H_c$,
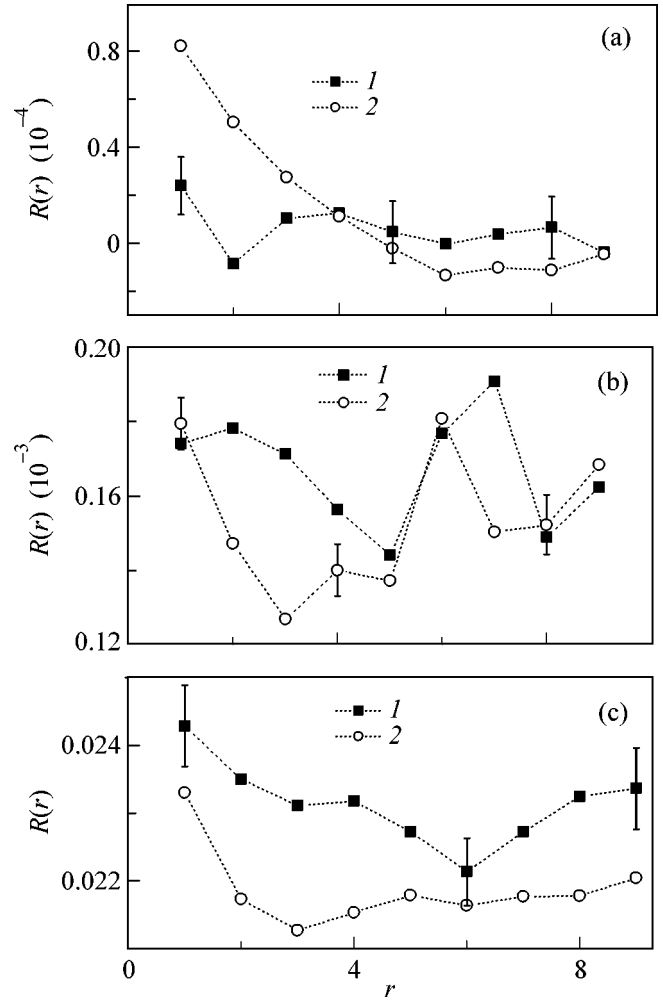
Fig. 4. Four-spin correlation functions for pairs of parallel spins calculated according to Eq. (4) for $\omega_0 = J$, $\alpha/\alpha_{c2} = 1$, and $H/J = $ (a) 0.5, (b) 2, and (c) 5 in the (*1*) [100] and (*2*) [010] directions.

and one minimum in $R(r)$ exists in the saturation field. The wave function of this state can be represented as a linear combination of the singlet and triplet states of dimers $\psi \sim u(|\uparrow\downarrow\rangle - |\downarrow\uparrow\rangle) - v|\uparrow\uparrow\rangle$, where the coefficients u and v depend on the field and the spin–phonon coupling parameter $u^2 \sim (1 + \delta/J)$, $v^2 \sim (1 - \delta/J)$, and $\delta = \alpha(u_i - u_{i+1})$.

The local singlet state decays in the magnetic field through the formation of two antiferromagnetic domain boundaries in which the loss in the Zeeman energy of the triplet with the effective exchange interaction $J - \delta$ is compensated by the gain in the exchange energy of the boundaries $J + \delta$. Estimations of the energy with regard to the exchange energy only for the longitudinal spin components lead to the critical magnetization $m_c = \sqrt{4 + 3\delta - 1.5K(\delta/\alpha)^2}/2\sqrt{2}$, above which the local stresses disappear.
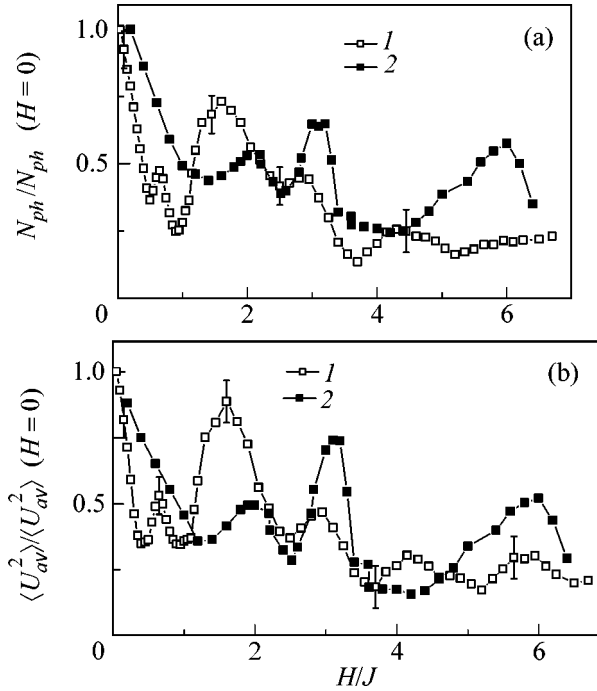
Fig. 5. (a) Average occupation numbers of phonons and (b) amplitudes of root-mean-square ion displacements $\langle U^2_{av}\rangle / \langle U^2_{av}(H=0)\rangle$ normalized to the maximum zero-field value for (*1*) $\omega_0/J = 1$ and $\alpha/\alpha_{c2} = 1$ and (*2*) $\omega_0/J = 6$ and $\alpha/\alpha_{c2} = 1.35$ calculated as a function of the magnetic field.

The field dependences of the average occupation number of phonons and the root-mean-square displacement of ions are displayed in Fig. 5. The oscillations in the dependences $N_{ph}(H)$ and $\langle U^2(H)\rangle$ are due to the decay of the bound spin–phonon state $\langle S^\alpha \ldots S^\beta b^\gamma \ldots b^\nu\rangle \longrightarrow \langle S^\alpha \ldots S^\beta\rangle\langle b^\gamma \ldots b^\nu\rangle$ in the magnetic field corresponding to the effective bond energy. The resulting phonons give rise to new local maxima in the distribution func-

tion of ion displacements (Fig. 2b). In the saturation field, the dispersion of the distribution function $P(u_i/u_{max})$ decreases. In this case, it can be approximated by a double-peaked Gaussian function; this can also be done for the distribution function of site magnetic moments $P(S^z)$ depicted in Fig. 3. Thus, in fields $H > H_c$, the nonuniformity of the interrelated spin-density and elastic-stress distributions is retained.

In conclusion, the main results will be emphasized. Interaction between the elastic and magnetic subsystems leads to a disordered single state with a hierarchical structure of ion displacements. The decay of bound spin–phonon particles in magnetic fields induces phonons, which are pinned at domain boundaries. As a result, the field dependence of the amplitude of the root-mean-square displacement has an oscillating shape. In the saturation field, the nonuniformity of the distributions of site magnetic moments and ion displacements is retained, and the saturation magnetization monotonically decreases with increasing spin–phonon coupling constant.

REFERENCES

1. A. W. Sandvik, S. Daul, R. R. P. Singh, and D. J. Scalapino, Phys. Rev. Lett. **89**, 247201 (2002).
2. S. S. Aplesnin, Zh. Éksp. Teor. Fiz. **124**, 1080 (2003) [JETP **97**, 969 (2003)].
3. F. Mila, Eur. Phys. J. B **6**, 201 (1998).
4. R. Chitra and T. Giamarchi, Phys. Rev. B **55**, 5816 (1997).
5. N. V. Prokof'ev and B. V. Svistunov, Phys. Rev. Lett. **81**, 2514 (1998); N. V. Prokof'ev, B. V. Svistunov, and I. S. Tupitsyn, Zh. Éksp. Teor. Fiz. **114**, 570 (1998) [JETP **87**, 310 (1998)].
6. M. Matsumoto, B. Normand, T. M. Rice, and M. Sigrist, Phys. Rev. Lett. **89**, 077203 (2002).

Translated by A. Bagatur'yants

Experimental Determination of the Conditions for the Transition of Jupiter's Atmosphere to the Conducting State

V. Ya. Ternovoĭ*, S. V. Kvitov, A. A. Pyalling, A. S. Filimonov, and V. E. Fortov

Institute of Problems of Chemical Physics, Russian Academy of Sciences, Chernogolovka, Moscow region, 142432 Russia
* e-mail: ternovoi@ficp.ac.ru
Received December 1, 2003

The intensity of optical radiation and resistance of a hydrogen–helium layer with He mass fraction $Y = m_{He}/(m_{He} + m_H) \cong 0.24$, which corresponds to the composition of the outer layers of Jupiter's atmosphere [2], were simultaneously measured under multiple shock compression up to 164 GPa in plane geometry. The initial pressure and temperature of the mixture were equal to 8 MPa and 77.4 K, respectively, and the velocity of steel strikers was equal to 6.2 km/s. These conditions allowed the generation of the final compressed curve close to the adiabatic states of Jupiter's atmosphere according to the models proposed in [2, 3]. The conditions for the appearance of the conducting phase in the compression process and the achieved level of electrical conductivity were determined. The experimental data were compared with the one-dimensional fluid-dynamic simulation of the compression process using the equation of state for the mixture in a model similar to the one proposed in [3, 8]. The experimental data were also compared with the behavior of pure components having the same initial density as in the mixture and compressed to the same final pressure. © 2004 MAIK "Nauka/Interperiodica".

PACS numbers: 96.30.Kf; 96.35.Kx; 96.35.Hv

The Galileo sounder data obtained for the structure and composition of the outer layers of Jupiter's atmosphere up to 1 MPa and 200 K [1] corroborated the applicability of the adiabatic approximation [2, 3] to the description of the pressure dependence of its temperature for $P > 0.1$ MPa. The measured helium fraction in the atmosphere proved to be close to its fraction inside the Sun, $Y = m_{He}/(m_{He} + m_H) \cong 0.234 \pm 0.005$. In the near future, the studied pressure range can hardly be extended by using spacecrafts. Therefore, the physical conditions for the transition of the atmosphere to the conducting state have not yet been determined.

The current models of Jupiter's atmosphere are based on the assumption that the hydrogen transition to the conducting state occurs at 150 [2] and 100 GPa [3].

The dynamic experiments on strong single and multiple compression of the initially liquid and gaseous hydrogen [4–6] show that its transition to the conducting state occurs at 40–140 GPa for a density of 0.4–0.7 g/cm³ and testify to the strong influence of temperature on this process. Consideration of this transition of Jupiter's atmosphere in [2, 4], where the presence of helium was ignored, overestimated the transition pressure, because helium is a source of additional heat in the mixture, as compared to pure hydrogen under adiabatic compression.

Experimental study of the condition for pressure-induced helium ionization under multiple shock compression [7] shows that helium undergoes transition to the conducting state at a pressure above 0.7 g/cm³ at temperatures of 15–40 kK realized in these experi-

ments. This circumstance enables one to assume that, with allowance for the additional helium-induced heating of the mixture, compared to pure hydrogen, the behavior of Jupiter's atmosphere at lower densities and temperatures is primarily determined by hydrogen. Calculations [5, 7] show that multiple shock compression is isentropic within the experimental accuracy when the third and the sequential waves pass through the compressed layer. In this case, at most two discrete matter states are realized in the compressed layer, and only a single state exists at times of reflection from the layer boundaries. By the action of two passing waves, the initial mixture can be carried to a state on Jupiter's isentrope, after which the behavior diagnostics becomes possible for higher discrete compression parameters.

In this paper, we report the experimental results on the conduction transition of a hydrogen–helium mixture with $Y = 0.245 \pm 0.015$ (for the mixture supplied by the AGA-BKZ firm), which is close to the value measured by Galileo, under multiple shock compression up to 130–160 GPa in the plane geometry. Figure 1 shows the P–T diagrams obtained by the thermodynamic simulation of the behavior of Jupiter's atmosphere, helium, and hydrogen according to [3, 4], together with the calculations of state trajectories for multiple shock compression in the experiments.

The fluid-dynamic simulation was carried out using the equation of state constructed for the mixture similarly to [8]. The interaction potential for hydrogen and helium atoms was taken from [8, 9]. The H_2–He inter-

action potential was experimentally determined in [10]. The parameters of the H_2–He interaction potential were taken as averages of the respective parameters of the H_2–H_2 and He–He interaction potentials according to [11]. The interaction potentials were taken in the following form modified with respect to the standard exp-6 potential:

$$V(r) = \begin{cases} \dfrac{\varepsilon}{\alpha - 6}\left[6e^{\alpha\left(1 - \frac{r}{r_a}\right)} - \theta\alpha\left(\dfrac{r_a}{r}\right)^6\right], & r > W, \\ Ae^{-Br}, & r \leq W. \end{cases}$$

In contrast to the standard exp-6 potential, this formula includes the parameter θ. It is necessary because the interaction potential for helium does not include long-range attraction. Table 1 presents the parameters of the interaction potentials used in this work.

The calculated interaction potentials and their comparison with the corresponding experimental data are shown in Fig. 2.

The dissociation of hydrogen atoms was taken into account according to the model proposed in [12] by the formula

$$E_{\mathrm{dis}}(V) = a_0 - a_1(V - V_0)^2 - a_2(V - V_0)^3, \quad V < V_0,$$

$$E_{\mathrm{dis}}(V) = a_0, \quad V > V_0.$$

According to the known cold curves for molecular and atomic hydrogen, the decrease in the ionization potential as a function of density can be described by the parameters $a_0 = 4.735$, $a_1 = 0.013$, $a_2 = 0.00732$, and $V_0 = 11.13055$ cm^3/mol. The degree of hydrogen dissociation in the mixture was calculated under the assumption that the dissociation potential depends not on the density but on the average number of atoms per unit volume.

Figure 1 shows that Jupiter's isentrope determined here agrees well with similar calculations by Hubbard *et al.* [13] and that the calculations according to [4] show no decrease in temperature in the dissociation process.

The experimental procedure for simultaneous measurement of the compression parameters and resistance of the compressed layer was similar to [7]. To initiate the compression process, 1.5-mm-thick 321-H-steel plates 30 mm in diameter were accelerated to 5.6 km/s by the detonation products of cylindrical condensed explosive charges in the process of face throwing. To accelerate a 1.5-mm-thick steel plate to a velocity of 6.2 km/s, a 4.5-mm-thick steel plate 40 mm in diameter was accelerated to 4.7 km/s by the detonation products and a 6-mm-thick PMMA layer was placed ahead of the thin steel plate. The initial temperature of the mixture was controlled by a platinum resistance thermometer and was equal, within an accuracy of 2 K, to 77.4 K, i.e., to the temperature of liquid nitrogen used for cooling. Based on the preliminary one-dimensional fluid-
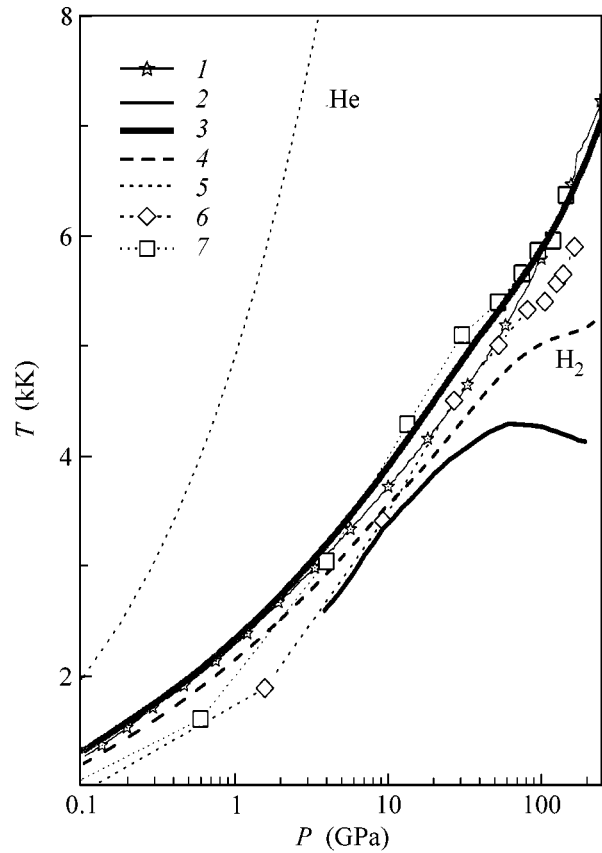
Fig. 1. The adiabat *P–T* diagrams of Jupiter's atmosphere beginning from a pressure of 0.1 MPa and a temperature of 165 K, as calculated according to (*1*) [3], (*2*) [4], and (*3*) this work; the corresponding diagrams for (*4*) hydrogen and (*5*) helium; and (*6*, *7*) the state trajectories of multiple shock compression.

dynamic simulation of the experiment, the initial pressure was taken to be 4 and 5.6 MPa for the low plate velocity and 8.1 MPa for the high velocity. Resistance was measured by the schemes with one and two measuring electrodes [7, 14]. In a 5-mm-thick optical-quality sapphire disk 20 mm in diameter (produced at the Monokristal synthetic-corundum factory in Stavropol), holes 0.45–0.8 mm in diameter were drilled at the vertices of an equilateral triangle with a side of 3.8 mm and were filled with indium. The measuring electrodes were situated on the disk axis. A diaphragmed quartz–quartz optical fiber with a diameter of 0.4 mm was situated on the outer side of the sapphire window between electrodes 2–3 mm from its axis. A silver-plated steel wire,
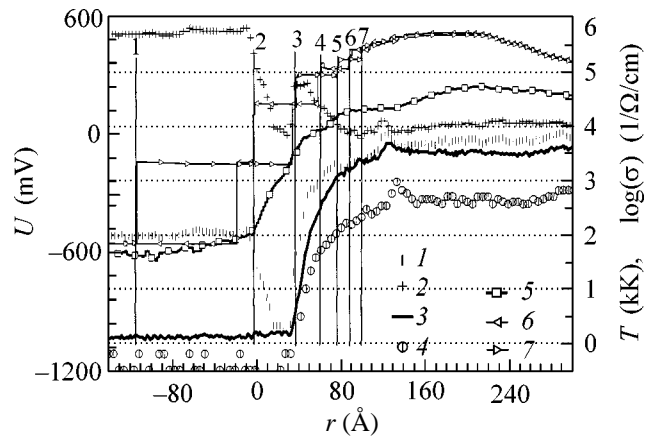
Table 1

		α	r_a (Å)	W (Å)	θ
H_2–He	24.53	11.05	3.19865	1.137827	0.5
He–He	16.53	11	2.9673	0	0
H_2–H_2	36.4	11.1	3.43	1.45855	1
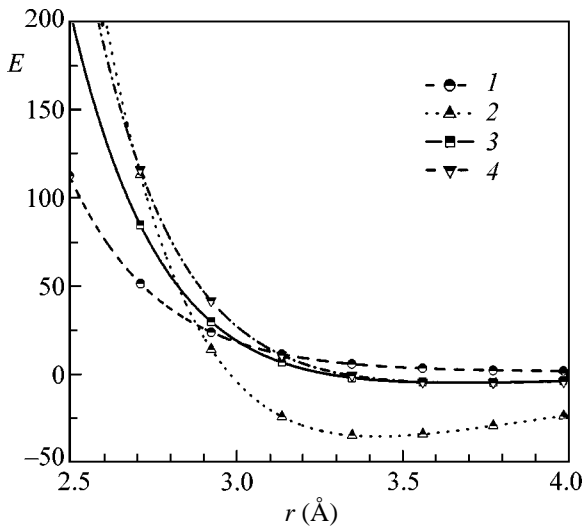
Fig. 2. Effective pair potentials of the (*1*) He–He, (*2*) H_2–H_2, (*3*) H_2–He, and (*4*) H_2–He interaction according to [10].

Fig. 3. Experimental records and simulations for the experiment with the mixture (m_{He}/m_{H_2} = 0.24): (*1*, *2*) voltage at the electrodes, (*3*) the resulting voltage at the sample, (*4*) recalculation of the mixture conductance (right axis), (*5*) measured temperature (right axis), and calculation of the mixture temperature in the (*6*) first and (*7*) last cells.

which had a diameter of 0.3 mm and jutted out of the internal sapphire surface by 1.2 mm, was pressed into the indium ground electrode with a diameter of 0.8 mm. Such a construction of the measuring cell reduces its inductance to 5–10 nH.

Figure 3 shows the experimental records of the resistance of the compressed layer, level of conductance, and brightness temperature measured by the three-electrode scheme for a striker velocity of 6.2 km/s and the straight lines indicate the times of shock wave reflection from the layer boundaries. The measured temperature is compared with the calculations of the temperatures of generated states by a one-dimensional fluid-dynamic code using the equation of state for the mixture. We took 200 cells for the compressed layer. The shown time dependence of temperature for the 10th and 190th points of the compressed layer shows a good agreement between the observed and calculated times of shock wave reflection from the layer boundaries. The calculated parameters of states behind the shock waves are presented in Table 2.

Using three electrodes to measure the resistance of the compressed layer, we were able to determine the final conductance (Σ) of the mixture at high pressures and find the boundary of atmosphere transition to the conducting state using only electrical measurements. Even after the third shock wave, the detected conductance was equal to 0.41 Ω^{-1} cm^{-1} (P = 26.5 GPa, ρ = 0.365 g/cm^3, T = 4380 K, Fig. 3). After the passage of the fourth shock wave, the conductance increases by two orders of magnitude to 55 Ω^{-1} cm^{-1} (P = 51.7 GPa, ρ = 0.494 g/cm^3, T = 4940 K). Taking account of the inductance effect increases this value threefold. Further compression to 0.8 g/cm^3 only doubles the conductance.

Thus, the above measurements show that the transition of Jupiter's atmosphere to the conducting state occurs at pressures of 25–50 GPa. This value agrees with the previously determined transition boundary for the initially gaseous hydrogen to the conducting state under multiple shock compression [5]. In future experiments, we plan to extend the ranges of the initial mix-

Table 2

No.	0	1	2	3	4	5	6	7	12
ρ, g/cm^3	0.0291	0.110	0.23	0.365	0.494	0.603	0.68	0.737	0.831
P, GPa	0.0081	1.57	9.03	26.5	51.7	80	104.4	124.6	164
T, K	77.4	1845	3320	4380	4940	5020	5205	5380	5690
U, mV	1025.2			1013	336.9	208.9	168.9	128.9	104.9
R, Ω				43	0.254	0.133	0.102	0.0756	0.059
L, mm	4.938			0.394	0.291	0.238	0.211	0.195	0.173
ρ, Ω cm				2.577	0.018	0.010	0.0084	0.0063	0.0052
Σ, Ω^{-1} cm^{-1}				0.388	55.05	96.87	118.9	158.5	194

ture densities and velocities of incident strikers to more accurately determine the Σ–p dependence in Jupiter's isentrope.

REFERENCES

1. U. Von Zahn, D. M. Hunten, and G. Lehmacher, J. Geophys. Res. **103**, 22815 (1998).

2. T. V. Gudkova and V. N. Zharkov, Planet. Space Sci. **47**, 1201 (1999).

3. D. Saumon, G. Chabrier, and H. M. Van Horn, Astrophys. J., Suppl. Ser. **99**, 713 (1995).

4. W. J. Nellis, Planet. Space Sci. **48**, 671 (2000); S. T. Weir, A. C. Mitchell, and W. J. Nellis, Phys. Rev. Lett. **76**, 1860 (1996).

5. V. E. Fortov, V. Ya. Ternovoĭ, S. V. Kvitov, *et al.*, Pis'ma Zh. Éksp. Teor. Fiz. **69**, 874 (1999) [JETP Lett. **69**, 926 (1999)]; V. Ya. Ternovoi, A. S. Filimonov, V. E. Fortov, *et al.*, Physica B (Amsterdam) **265**, 6 (1999).

6. G. W. Collins, P. M. Celliers, D. M. Gold, *et al.*, Contrib. Plasma Phys. **39**, 13 (1999).

7. V. E. Fortov, V. Ya. Ternovoĭ, M. V. Zhernokletov, *et al.*, Zh. Éksp. Teor. Fiz. **124**, 288 (2003) [JETP **97**, 259 (2003)].

8. H. Juranek and R. Redmer, J. Chem. Phys. **112**, 3780 (2000).

9. W. J. Nellis, N. C. Holmes, A. C. Mitchell, *et al.*, Phys. Rev. Lett. **53**, 1248 (1984).

10. R. Gengenbach, J. Strunck, and J. Toennies, J. Chem. Phys. **54**, 1830 (1971).

11. F. H. Ree, in *Shock Waves in Condensed Matter, 1987*, Ed. by S. C. Schmidt and N. C. Holmes (Elsevier, Amsterdam, 1988), p. 125.

12. M. Ross, J. Chem. Phys. **86**, 7110 (1987).

13. W. B. Hubbard, T. Guillot, M. S. Marley, *et al.*, Planet. Space Sci. **47**, 1175 (1999).

14. R. S. Hawke, A. C. Mitchell, and R. N. Keeler, Rev. Sci. Instrum. **40**, 632 (1969).

Translated by R. Tyapaev